

KEK Proceedings 2009-6  
November 2009  
R

# Proceedings of the Sixteenth EGS Users' Meeting in Japan

August 6 - 8, 2009.  
KEK, Tsukuba, Japan

Edited by

Y. Namito, H. Hirayama and S. Ban



High Energy Accelerator Research Organization

**High Energy Accelerator Research Organization (KEK), 2009**

KEK Reports are available from:

High Energy Accelerator Research Organization (KEK)  
1-1 Oho, Tsukuba-shi  
Ibaraki-ken, 305-0801  
JAPAN

Phone: +81-29-864-5137  
Fax: +81-29-864-4604  
E-mail: [irdpub@mail.kek.jp](mailto:irdpub@mail.kek.jp)  
Internet: <http://www.kek.jp>

## FOREWARD

The Sixteenth EGS Users' Meeting in Japan was held at High Energy Accelerator Research Organization (KEK) from August 6 to 8. The meeting has been hosted by the Radiation Science Center. More than 100 participants attended the meeting.

The meeting was divided into two parts. Short course on EGS was held at the first half of the workshop using EGS5 code. In the later half, 17 talks related EGS were presented. The talk covered the wide fields, like the medical application and the calculation of various detector responses *etc.* These talks were very useful to exchange the information between the researchers in the different fields.

Finally, we would like to express our great appreciation to all authors who have prepared manuscript quickly for the publication of this proceedings.

Hideo Hirayama  
Yoshihito Namito  
Syuichi Ban  
Radiation Science Center  
KEK, High Energy Accelerator Research Organization

## CONTENTS

<b>Investigation for an Application of Strong Magnetic Field to X-Ray Therapy for Inhomogeneous Region</b>	1
<i>H. Itoh, A. Wakita, R. Taniguchi, S. Okuda, A. Sawada, Y. Iwashita, A. Noda and M. Hiraoka</i>	
<b>Effects of Scattered Radiation due to a Gold Internal Fiducial Marker for Precise Setup in External Radiotheraph</b>	8
<i>K. Habara, T. Shimozato, Y. Aoyama, R. Kawanami, K. Yasui, M. Komori, and Y. Obata</i>	
<b>Comparison of Output Factor Obtained by Measurement and Radiation Treatment Planning System in a Lung Tissue</b>	13
<i>Y. Igarashi, Y. Aoyama, Y. Obata, K. Habara, T. Shimozato, and M. Komori</i>	
<b>Investigation for the Calculation of Absorbed Dose in High-Density Bone Material</b>	21
<i>T. Matsunaga, T. Shimozato, Y. Aoyama, M. Komori, and Y. Obata</i>	
<b>Development and Validation of Monte Carlo Dose Verification System for Intensity Modulated Radiotherapy</b>	30
<i>Y. Ishihara, Y. Narita, T. Yamamoto, T. Mizowaki, Y. Miyabe, A. Sawada, S. Yano, T. Teshima, and M. Hiraoka</i>	
<b>Investigation of Uniform Exposure to Surface Lesion Using Ir-192 Source</b>	40
<i>K. Yasui, Y. Aoyama, T. Shimozato, R. Kawanami, K. Habara, M. Komori, and Y. Obata</i>	
<b>Comparing with the Calculations of Plato Clinical Treatment Planning System and EGS5 Simulations for Brachytherapy</b>	48
<i>S. Tsuji and N. Narihiro</i>	
<b>Monte Carlo Characterization of the Photon Source from a Clinical Linear Accelerator</b>	53
<i>N. Mukumoto and T. Teshima</i>	
<b>Effect of the Beam Shaping Filter in the X-ray CT Simulation</b>	59
<i>Y. Morishita and S. Koyama</i>	
<b>Assessment of the Validity of Virtual Grid Using Monte Carlo Code EGS5</b>	65
<i>Y. Chujo and S. Koyama</i>	
<b>Simulations of Photon Specific Absorbed Fractions in a Mouse Voxel Phantom</b>	70
<i>A. Mohammadi and S. Kinase</i>	

<b>Evaluation of Counting Efficiencies of a Whole-Body Counter Considering the ICRP Biokinetic Models</b>	78
<i>M. Takahashi, S. Kinase, and R. Kramer</i>	
<b>Evaluation of LSO Scintillator Characteristics for Development of Lost Alpha Particle-Induced Gamma Ray Detector System in ITER</b>	84
<i>S. Kashiwa, M. Nishiura, T. Tanaka, T. Nagasaka, K. Fujioka, A. Okamoto, S. Kitajima, and M. Sasao</i>	
<b>Evaluation of Delta-Rays Production in a Wall-Less Tissue Equivalent Proportional Counter Irradiated by Energetic Heavy Ion Beams</b>	90
<i>S. Tsuda, T. Sato, H. Iwase, Y. Namito, and S. Sasaki</i>	
<b>Incorporating the LPM Effect in the EGS5 Code</b>	96
<i>Y. Kirihara, Y. Namito, and H. Hirayama</i>	
<b>Charged Particle Transport Calculation with GPU 2</b>	110
<i>K. Okei and T. Nakatsuka</i>	

# INVESTIGATION FOR AN APPLICATION OF STRONG MAGNETIC FIELD TO X-RAY THERAPY FOR INHOMOGENEOUS REGION

H. Itoh<sup>1</sup>, A. Wakita<sup>2</sup>, R. Taniguchi<sup>3</sup>, S. Okuda<sup>3</sup>, A. Sawada<sup>1</sup>, Y. Iwashita<sup>4</sup>, A. Noda<sup>4</sup> and M. Hiraoka<sup>1</sup>

<sup>1</sup>Department of Therapeutic Radiology and Oncology, Kyoto University Graduate School of Medicine, Kyoto 606-8507, Japan

<sup>2</sup>Radiation Oncology Division, National Cancer Center Hospital

<sup>3</sup>Quantum-beam Science, Frontier Science innovation Center, Osaka Prefecture University, Sakai 599-8570, Japan

<sup>4</sup>Accelerator Laboratory, Advanced Research Center for Beam Science, Institute for Chemical Research, Kyoto University, Kyoto 611-0011, Japan

*e-mail: itoh@kuhp.kyoto-u.ac.jp*

## Abstract

Radiation therapy techniques advance from day to day. Image guided radiation therapy (IGRT) is particularly of current interest all over the world. An use of magnetic resonance imaging (MRI) is one of the IGRT techniques. In magnetic fields, charged particles are deflected by the Lorentz force. So, we discussed about an utility of magnetic fields to X-ray therapy by the monte carlo simulation EGS and mesurement data. As effects of magnetic fields get apparent in low density regions, we considered an application was better for lung cancer.

An application of magnetic fields to X-ray therapy made the more dose convergence than that of normal X-ray therapy, but unfavorable middle dose regions appeared at the mediastinum and chest wall due to the uniformity of magnetic field. Some kind of improvements are needed to overcome this defect.

## I. Introduction

MRI-Linac is been developped in order to verify set-up of patients before irradiation or see internal organ motion under irradiation<sup>1)-3)</sup>. Raaijmakers<sup>4)</sup> reported that, using IMRT, dose distribution in magnetic fields was comparable with that in non magnetic field. IMRT (Intensity Modulated Radiation Therapy) is one of the methods to deposit homogeneous high dose at the target by optimization of many beamlets. We thought deflection effects of magnetic field for secondary electrons by MRI-Linac would make ideal dose distribution which traditional irradiation methods couldn't realize. Eq.1 is the Bethe-Bloch's equation for electrons. This equation implies that the stopping power get small and ranges of electrons get long in low density regions. The longer ranges electrons have, the more apparent the effect of magnetic field gets. For this reason, we considered that it was better to apply magnetic field to lung cancer. Firstly, we investigated how dose distribution was changed by the presence of magnetic fields. Secondly, we measured dose distribution in magnetic fields by the electron linac and the permanent magnet, which is a third scale model of the AVF cyclotron, established at Osaka prefecture university.

$$S_{col} = \frac{2\pi e^4}{mv^2} NZ \left[ \ln \frac{mv^2 E}{2I^2(1-\beta^2)} - \left( 2\sqrt{(1-\beta^2)} - 1 + \beta^2 \right) \ln 2 + 1 - \beta^2 + \frac{1}{8} \left( 1 - \sqrt{(1-\beta^2)} \right)^2 \right] \quad (\text{Eq.1})$$

## II. Material and Methods

### II-1. Monte Carlo Simulation

An calculation model was built based on CT images of lung cancer. **Fig.1** shows calculation model. Four thresholds were established from the difference of CT values: air, lung, soft tissue and bone. A simulated tumor was manually added. The simulated tumor of 1.5cm in diameter was added in the center of right lung and isocenter was set at the center of the tumor. The energy spectrum of initial particles were quoted from the Daryoush's report<sup>5)</sup>. The 6MV of Varian's linac was assumed. **Table.1** shows the beam configuration. Coplanar arrangement was adopted. This was because some groups<sup>1)-3)</sup> studying MRI-linac assumed an open-bore MR scanner. Initial particles were  $10^8$  in number and each particle move between 1mm x 1mm x 2.5mm voxels. Absorbed dose deposited in those voxels was evaluated. Lower limit energies of electron and photon were 10 keV and 521 keV, respectively. Uniform magnetic fields directed from foot to head. The strength of the magnetic field was 0.5T, 1.5T or 0T all over the model. To compare each distribution, dose of all calculations was normalized at each isocenter dose.

### II-2. Measurement at Simple Geometry

We thought the deflection effect for secondary electrons by magnetic fields was verified by not only monte carlo simulation but also actual measurement. So, we made some experiments at Osaka prefecture university. As the energy of linac was variable, we used energy ranges between 6MeV to 8MeV. Through all measuments, currents of electron beam were stable between 1 $\mu$ A to 8 $\mu$ A. Accelerated electrons once went outside through the window made of titanium whose thickness was 5 $\mu$ m. Then, they entered to the tungsten plate and produced bremsstrahlung X-rays. Produced X-rays were collimated to 2mm x 2mm. The gap of magnetic poles was set to 6cm in order to insert the phantoms. To the difficulty, magnets were designed as a third scale model of AVF cyclotron. So, they had concavo-convex shapes on their surfaces. In order to smooth surfaces of the magnets and get uniform magnetic fields, some iron plates were inserted to the valley of magnets. As to the detector, we used EBT radiochromic films. This is because radiochromic films doesn't need image development and the measument results are immediately confirmed. Two shapes of Tough-Water phantoms were inserted to the gap of magnet. The hexahedron phantom simulated the chest wall and the sphere phantom simulated the tumor, respectively. Both phantoms were divided to two pieces. Radiochromic films were sandwiched in those pieces of both phantoms and set parallel to the beam direction. The distance from the tungsten plate to the center of the sphere phantom was 65cm. After irradiation, results measured by films were converted from blackening distributions to dose distributions. **Fig.2** shows the experimental set-up mentioned above.

## III. Results

### III-1. Monte Carlo Simulation

**Fig.3** (a)(b)(c) shows the dose distributions without magnetic fields, with 0.5T and 1.5T, respectively. **Fig.3** (b) and **Fig.3** (c) show similar tendencies as a whole. It was found that the secondary electrons produced in the tumor were deflected with magnetic fields, returned to the tumor and deposited their energies. As the radius of rotation was long in the case of 0.5T, secondary electrons were stopped in the lung before returning to the tumor and the low dose region spread around the tumor like a halo. But high dose was localized at the tumor in the case of 1.5T. **Fig.3**

(d) and **Fig.3** (e) were the differential images when the dose distribution in the case of 0T was subtracted from that of 0.5T and 1.5T, respectively. Those images indicate that the dose in the lung region was decreased, but the dose in the chest wall and mediastinum was increased. This is because the effect of magnetic fields to secondary electrons were not selective and dose enhancement was occurred in density differential regions similar to the boundary between the lung and tumor. Raaijmakers reported similar results<sup>(6-7)</sup>. **Fig.4** is the dose volume histogram curve about the gross tumor volume (GTV) and lung acquired from each calculation. Compared with the case of 0T, in the case of 0.5T and 1.5T, volume of high dose of the GTV is increased and the gradient of curves gets moderate. It is considered that secondary electrons in the tumor were slightly deflected and an ununiformity of the dose distribution was occurred.

### III-2. Measurement at Simple Geometry

**Fig.5** shows the magnetic flux density measured by hall probe before the irradiation. Horizontal axis is the distance from the center of the gap of magnetic poles and vertical axis is the strength of magnetic fields. At both parts of original hill and valley, approximately uniform magnetic fields of 0.47T were acquired. The results calculated in advance by EGS indicated that dose enhancement was occurred not only at the tumor but at the other density differential regions. So, for demagnetization, iron plates were established in front of the chest wall phantom. The results after that work are shown in **Fig.6**. The horizontal axis indicates the distance perpendicular to the beam direction, the axis of the depth direction indicates the distance along the beam direction and the vertical axis indicates the strength of the magnetic field. Iron plates demagnetized to about 0.2T on their surfaces, but didn't more than 2cm away from their surfaces. The difference of dose distributions with or without magnetic fields is indicated in **Fig.7**. In **Fig.7**, upper is the dose distribution without magnetic fields and lower is the result measured in the gap of magnetic poles. As secondary electrons were deflected by the Lorentz force in magnetic fields, beam profile in the phantom was slightly spread to the inferior direction on paper. In the air, that effect was remarkable and then the appearance that distribution spreaded drawing the arc was found. **Fig.7** also shows that high energy electrons returned to the sphere phantom and deposited their residual energies on the surface of the phantom. Same tendency was observed at the back wall of the chest wall phantom. **Fig.8** is the results before and after the iron plate was inserted. Upper dose distribution is the same of the lower in **Fig.7** and lower is the result after the insert of iron plates. Indicated in **Fig.6**, as the demagnetization was measured only at the surfaces of iron plates, any distinct variations were not seen.

## IV. Discussions

As mentioned in the previous section, the effect of magnetic fields was remarkable in the region that the density shifted from high to low. As uniform magnetic fields were assumed, electrons returned not only at the tumor but at the chest wall and mediastinum. As to the mediastinum, dose distribution will be improved by the rearrangement of beams. In order to prevent the appearance of middle dose region at healthy tissues, magnetic fields need to be ununiform. In our experiments, iron plates were inserted in front of the chest wall phantom but the demagnetization was observed only on the surfaces of iron plates. So, we need to optimize the arrangement of materials to attenuate magnetic fields.

## V. Conclusion

It was indicated that an application of magnetic fields to X-ray therapy was be useful by monte carlo simulation and measurement data. Dose deposited by the electrons deflected by magnetic fields got high at the tumor, but unfavorable middle dose regions may appear at the chest wall and mediastinum. Optimized distribution of magnetic fields will make dose enhancement only at the tumor.

## References

- 1) Zhifei Wen, Rebecca Fahrig, Scott T. Williams and Norbert J. Pelc, “Shimming with permanent magnets for the x-ray detector in a hybrid x-ray/MR system”, Med. Phys. **35**, 3895-3902(2008)
- 2) B. G. Fallone, B. Murray, S. Rathee, T. Stanescu, S. Steciw, S. Vidakovic, E.Blosser and D. Tymofichuk, “First MR images obtained during megavoltage photon irradiation from a prototype integrated linac-MR system”, Med. Phys. **36**, 2084-2088(2009)
- 3) B. W. Raaijmakers, J. J. W. Lagendijk, J. Overweg, J. G. M. Kok, A. J. E. Raaijmakers, E. M. Kerkhof, R. W. van der Put, I. Meijsing, S. P. M. Crijs, F. Benedosso, M. van Vulpen, C. H. de Graaff, J. Allen and K. J. Brown, Phys. Med. Biol. **54**, 229-237(2009)
- 4) J. E. Raaijmakers, B. Hardemark, B. W. Raaymakers, C. P. J. Raaijmakers and J. J. W. Lagendijk, “Dose optimization for the MRI-accelerator: IMRT in the presence of a magnetic field”, Phys. Med. Biol. **52**, 7045-7054(2007)
- 5) S .B.Daryoush et.al., “Monte Carlo calculation of nine megavoltage photon beam spectra using the BEAM code”, Med.Phys., **29**(2002)
- 6) A. J. E. Raaijmakers, B. W. Raaymakers and J. J. W. Lagendijk, “Integrating a MRI scanner with a 6MV radiotherapy accelerator: dose increase at tissue-air interfaces in a lateral magnetic field due to returning electrons”, Phys. Med. Biol. **50**, 1363-1376(2005)
- 7) J. E. Raaijmakers, B. W. Raaymakers, S. van der Meer and J. J. W. Lagendijk, “Integrating a MRI scanner with a 6MV radiotherapy accelerator: impact of the surface orientation on the entrance and exit dose due to the transverse magnetic field”, Phys. Med. Biol. **52**, 929-939(2007)

**Table.1** The coplanar beam arrangement

<b>Field #</b>	<b>1</b>	<b>2</b>	<b>3</b>	<b>4</b>	<b>5</b>	<b>6</b>
<b>Gantry</b>	<b>20</b>	<b>335</b>	<b>300</b>	<b>260</b>	<b>240</b>	<b>175</b>
<b>Couch</b>	<b>0</b>	<b>0</b>	<b>0</b>	<b>0</b>	<b>0</b>	<b>0</b>

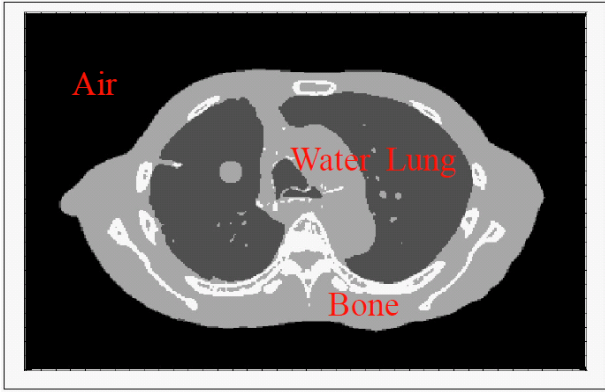


**Fig.1** The calculation model based CT images of lung cancer

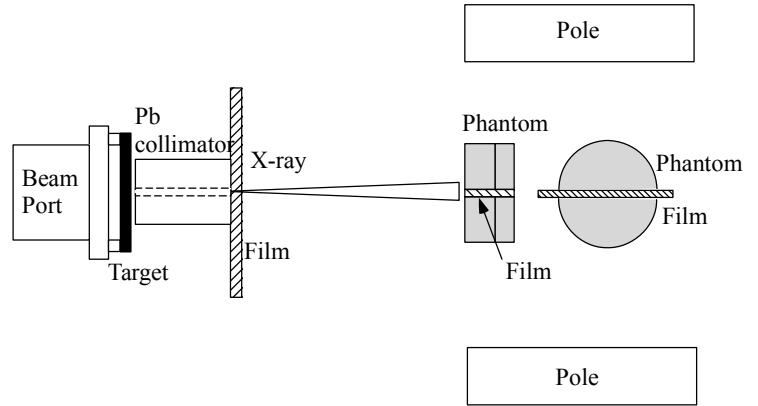


**Fig.2** Measurement setup at Osaka Perfectual University

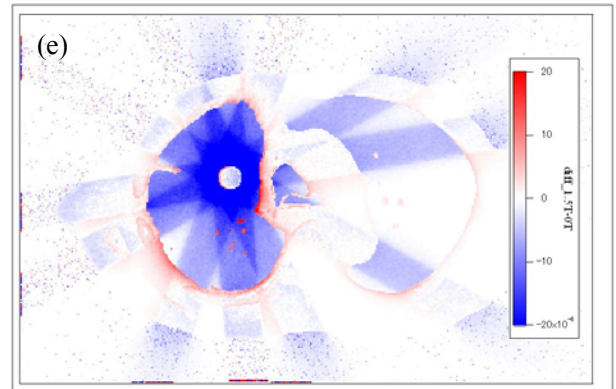
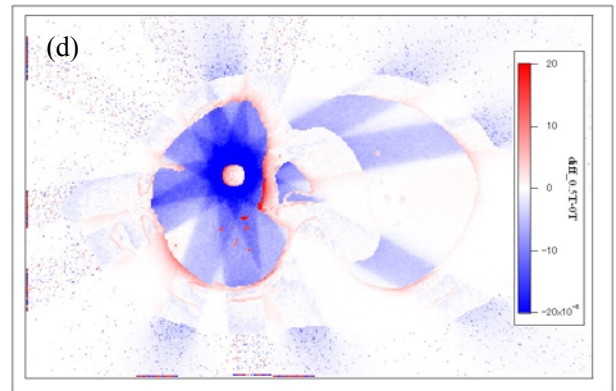
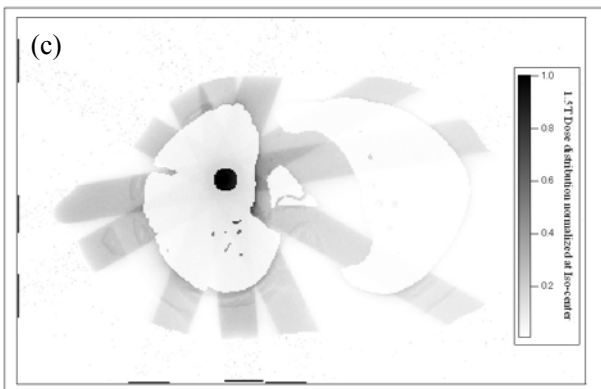
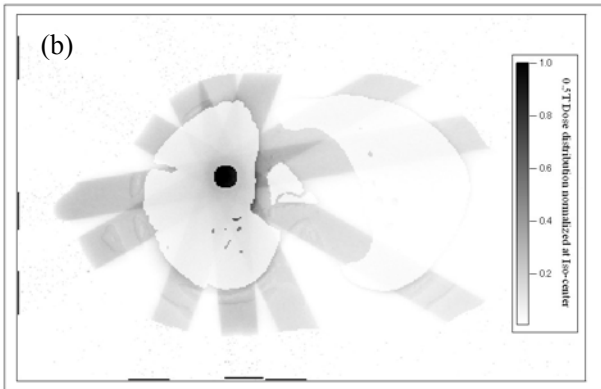
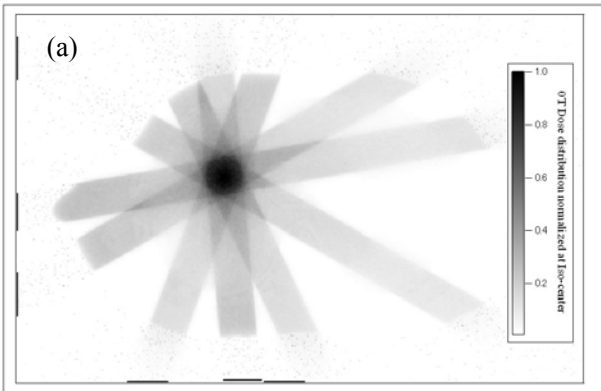


**Fig.3** Dose distributions  
 (a)0T, (b)0.5T, (c)1.5T,  
 (d)Subtraction of dose distribution at 0T from 0.5T and  
 (e) Subtraction of dose distribution at 0T from 1.5T

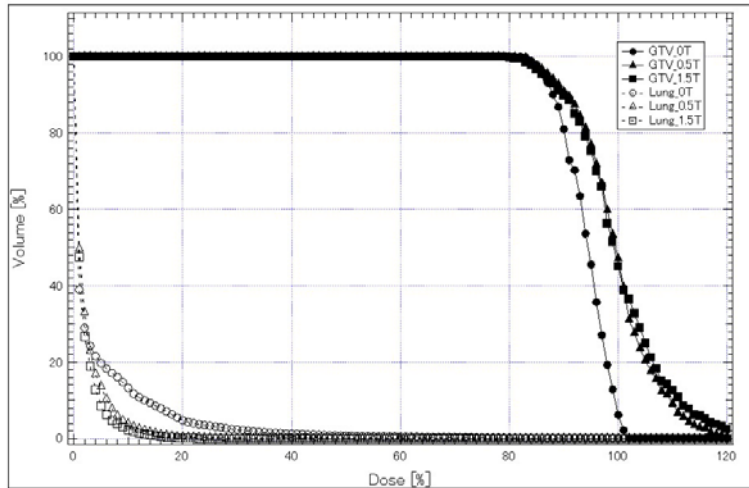


**Fig.4** Dose volume histograms of the monte carlo calculation

Circles represents 0T, triangles represents 0.5T and squares represents 1.5T, respectively.

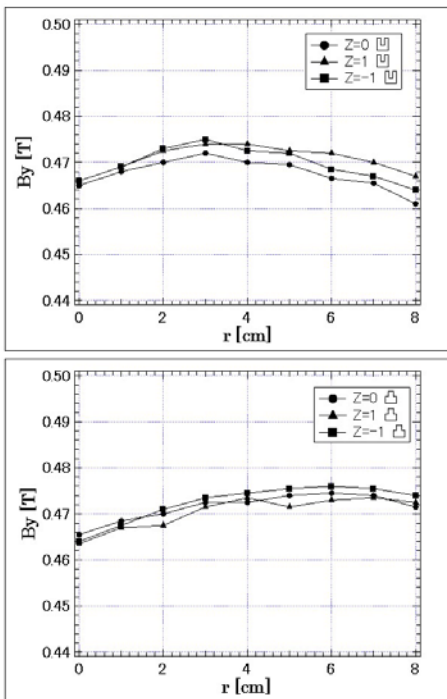


**Fig.5** Magnetic field distribution after the insert of iron plate. Upper is valley part of original geometry of magnet and lower is hill part

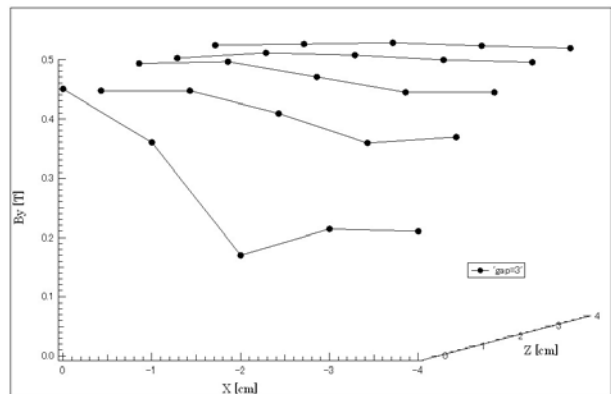


**Fig.6** Horizontal distribution after insert of iron plate in order to attenuate magnetic field

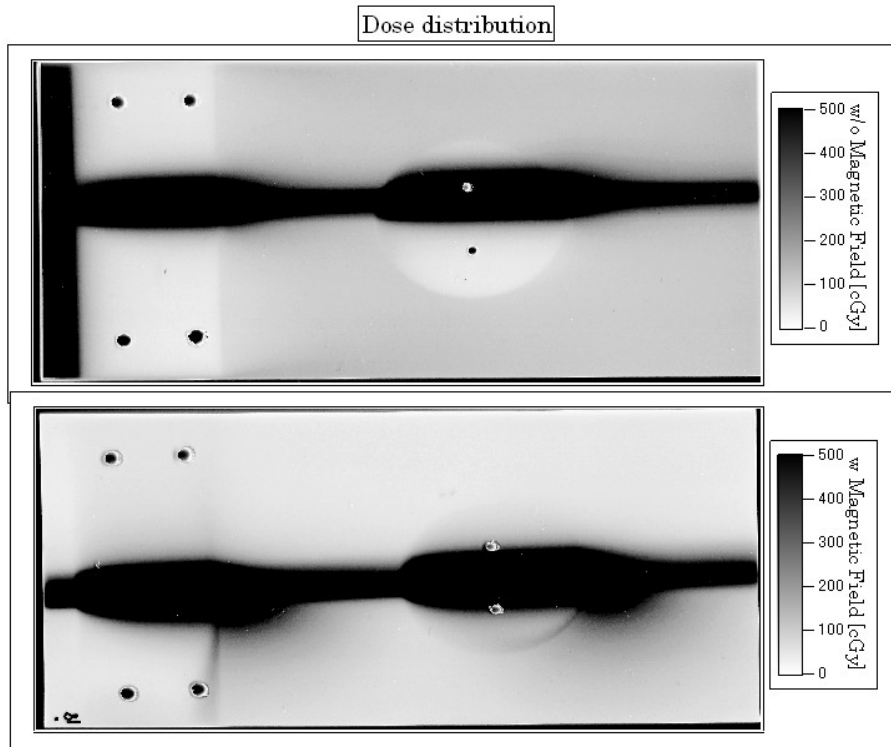


**Fig.7** Dose distribution in the gap of permanent magnets

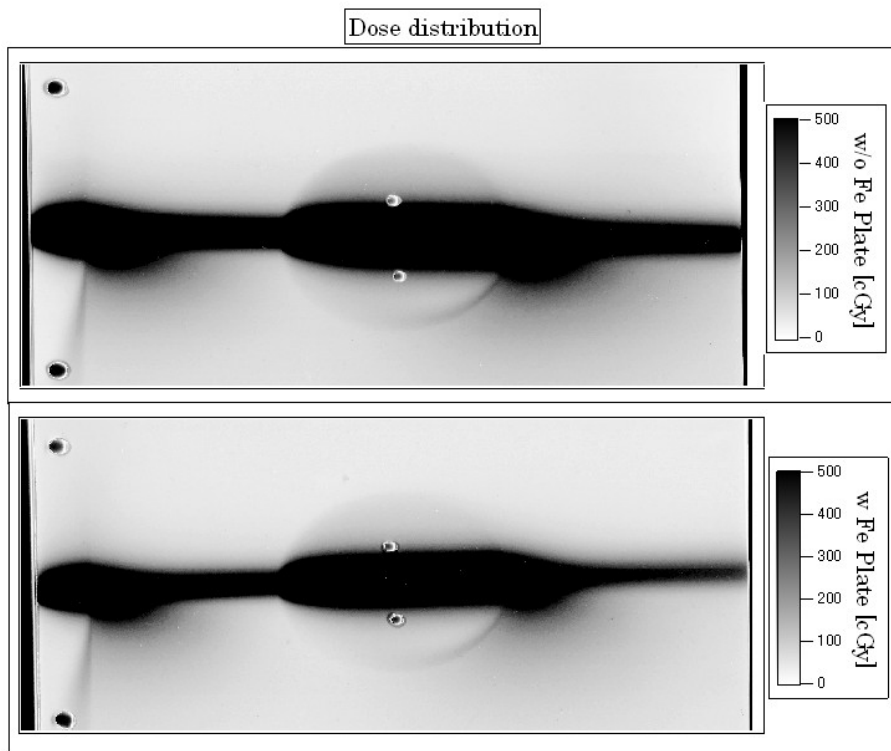


**Fig.8** Dose distribution in the gap of permanent magnets after the insert of iron plate for attenuation

# EFFECTS OF SCATTERED RADIATION DUE TO A GOLD INTERNAL FIDUCIAL MARKER FOR PRECISE SETUP IN EXTERNAL RADIOTHERAPY

K. Habara<sup>1</sup>, T. Shimozato<sup>2</sup>, Y. Aoyama<sup>3</sup>, R. Kawanami<sup>1</sup>, K. Yasui<sup>1</sup>, M. Komori<sup>2</sup> and Y. Obata<sup>2</sup>

<sup>1</sup>*Department of Radiological Technology, Graduate School of Medicine, Nagoya University  
1-1-20 Daikou-Minami, Higashi-ku, Nagoya-city, Aichi, 461-8673, Japan*

<sup>2</sup>*Department of Radiological Technology, Nagoya University School of Health Science*

<sup>3</sup>*Division of Radiology, Nagoya University Hospital*

*e-mail: habara.kosaku@d.mbox.nagoya-u.ac.jp*

## Abstract

Monitoring a gold marker position in or near the tumor in the radiotherapy can identify the tumor localization with a high degree of accuracy. However, it has been reported that the dose calculation using Radiation Treatment Planning Systems (RTPS) cannot calculate with the accuracy in the vicinity of high-Z and high-density interfaces. We investigated the effects of the scattered radiation due to a gold internal fiducial marker along the beam axis in a virtual lung phantom. However, practically, it is very important that the effects of scattered radiation near the marker are considered in the patient body. The purpose of this work is to study effects of the scattered radiation due to the gold internal fiducial marker in the virtual lung phantom by comparing the relative dose distributions of vertical direction to the beam axis using Monte Carlo (MC) simulation, film measurement and the RTPS calculation. The Electron Gamma Shower code version 5 (EGS5) was used for MC simulation. Radiochromic Film was used for the measurement. XiO was used for the RTPS calculation. The virtual lung phantom was irradiated by 10 MV photon beam with 5 x 5 cm<sup>2</sup> field size. The differences for isodose level greater or equal to 50 % between the MC simulation and the RTPS calculation were up to 23.5 % in front of the gold marker, and up to 7.8 % at behind of gold marker. The causes of the differences between the MC simulation and the RTPS calculation are thought that the RTPS cannot precisely calculate the doses of the backscatter radiation, the frontscatter radiation, and the lateral scatter radiation, the lack of the secondary electron equilibrium, and etc.

## 1. Introduction

Real-time tumor-tracking radiotherapy (RTRT) is one of radiotherapy techniques, and the precise localization of moving tumors has become more and more important with RTRT [1]. Insertion of some internal fiducial markers into or near the tumor is essential step in RTRT. Monitoring the gold marker positions in the radiotherapy can identify the tumor localization with a high degree of accuracy.

In the radiotherapy, Radiation Treatment Planning Systems (RTPS) are used for the dose calculation inside patients. The correct dose calculation is crucial component in the radiation treatment planning. However, RTPS has been unsuccessful in the correct dose calculation for the vicinity of high-Z and high-density substances [2, 3]. In our previous study, we investigated the effects of the scattered radiation due to a gold internal fiducial marker along the beam axis in a virtual lung phantom. However, practically, it is very important that the effects of scattered radiation near the marker are considered in the patient body.

Therefore, we studied effects of the scattered radiation due to the gold internal fiducial marker in the virtual lung phantom by comparing the relative dose distributions of vertical direction to the beam axis using Monte Carlo (MC) simulation, the film measurement and the RTPS calculation.

## 2. Materials and Methods

### 2.1 Measurements to obtain density-dose conversion curve and dose profiles

Water-equivalent phantoms (tough water phantom, Kyoto kagaku Co.,LTD) of the size of 30 x 30 x 30 cm<sup>3</sup> and Radiochromic Films (Gafchromic EBT Film, ISP.Inc) with the same lot number were used to obtain calibration curve for the conversion from the density to the dose. This film was selected because it can be used in the bright place, it can be placed closely to the gold marker and the phantom, it can be cut freely and etc [4, 5]. It has been reported that the uncertainty of the measurement using Gafchromic EBT Film was approximately 5.0 % [4, 5]. The films were placed in verticality to the central axis of 10 MV photon beams which were delivered from Varian Clinac 21 EX (Varian Medical Systems.Inc) with field size of 10 x 10 cm<sup>2</sup> to obtain calibration curve, and exposed by 13 steps of monitor-units (MU) from 0 MU to 400 MU at source axis distance of 100 cm (source surface distance (SSD) = 90 cm, depth = 10 cm). 100 MU = 1 Gy at depth of maximum dose.

Fig. 1 shows the virtual lung phantom which was composed of tough water phantoms, tough lung phantoms (Kyoto kagaku Co.,LTD), cork boards (Kobe cork Co.,LTD), and a 2.0-mm-diameter gold ball (Eishin Co.,LTD). To obtain dose profiles, the films were placed at 5, 8 and 8.2 cm depth from the phantom surface (5 cm depth was used of the standard of the relative dose, 8 cm depth corresponded to the front of the gold ball, and 8.2 cm depth corresponded to the behind of the gold ball). The field size was 5 x 5 cm<sup>2</sup> determined by jaw collimators because small fields are used practically. The virtual lung phantom was irradiated 250 MU at 100 cm of SSD. All films were digitalized by a flatbed scanner (EPSON Offirio ES 10000G) and analyzed by DD-system (Version 9.0.0, R-TECH.Inc).

### 2.2 MC simulations to obtain dose profiles

The Electron Gamma Shower code version 5 (EGS5) was used for MC simulation. The simulation geometry was reconstructed accurately from the measurement geometry (shown in Fig. 1) except the films to compare between the film measurement and MC simulation. In the simulation, water was used for the material instead of the film because the composition of water was near the film. Table 1 shows the composition of the geometry and the density of the materials [6, 7]. The geometry for MC simulation was shown in Fig. 2. Data acquisition regions were allocated in the water phantom and each voxel size was 0.1 x 0.2 x 0.0234 cm<sup>3</sup>. Energy spectrum was quoted from published data for 10 MV photon beams of Varian [8]. The cut-off energies for transport calculation of electron (ECUT) and photon (PCUT) in all calculations of this study were set to 521 keV and 10 keV, respectively. Statistical uncertainties of the MC simulations were less than 1.0 % for the isodose level greater than or equal to 50 %.

### 2.3 RTPS calculations to obtain dose profiles

XiO (Version 4.33.02, CMS.Inc) was used for RTPS calculations. The multi grid superposition algorithm was selected for all RTPS calculations because it was superior to any other XiO calculation algorithms including pencil beam, clarkson and convolutions [9, 10]. The inhomogeneity correction was processed in pixel by pixel, and the size of the calculation grid was 0.1 x 0.1 x 0.1 cm<sup>3</sup>. The dose calculations using the algorithm were fitted in that of the same linear accelerator used in the measurement.

The geometry for the RTPS calculation was the same arrangement as the measurement. The virtual lung phantom was scanned and reconstructed by using the X-ray computed Tomography (CT) named Asteion (Toshiba medical Co.,LTD). In RTPS calculations, CT number-electron density conversion table is required, and the table ranges in XiO were from 0.3 (particles/ m<sup>3</sup>) to 1.8 since the table ranges typically used from air to bone. However, the relative electron density of the material of gold is higher than 1.8, then the relative electron density of the gold automatically assigned 1.8.

### 3. Results

Fig. 3 shows the comparison of off center ratio (OCR) curve at 8 cm depth corresponded to the front of the gold ball normalized to the dose at 5 cm depth among the MC simulation, the film measurement and the XiO calculation. The dose increment in the vicinity of the central axis was not seen in XiO calculation though it was seen in the MC simulation and the film measurement. The difference between the calculation results of EGS5 and measured data is defined as follows:

$$difference = \frac{D_{measurement} - D_{EGS5}}{D_{EGS5}} \times 100 \quad [\%]$$

where  $D_{measurement}$  and  $D_{EGS5}$  are the relative dose in measurement and EGS5, respectively. The difference between the calculation results of EGS5 and XiO is defined as follows:

$$difference = \frac{D_{XiO} - D_{EGS5}}{D_{EGS5}} \times 100 \quad [\%]$$

where  $D_{XiO}$  are the relative dose in XiO. The method of evaluating the OCR curve was quoted from the criteria as reported by ESTRO [11]. It assumed on a beam center axis to be  $\delta_1$ , and on the area of making to smoothness in the irradiation field to be  $\delta_3$ . The differences of the MC simulation and the measurement were 6.6 % on  $\delta_1$ , and 0.2 % on  $\delta_3$ . The differences of the MC simulation and the XiO calculation were -23.5 % on  $\delta_1$ , and -2.1 % on  $\delta_3$ .

Fig.4 shows OCR curves at 8.2 cm depth. The dose decrement in the vicinity of the central axis was not seen in XiO calculation though it was seen in MC simulation and the film measurement. The differences of the MC simulation and the measurement were -11.2 % on  $\delta_1$ , and -0.3 % on  $\delta_3$ . The differences of the MC simulation and the XiO calculation were 7.2 % on  $\delta_1$ , and -2.3 % on  $\delta_3$ .

### 4. Discussion

The differences as shown in Figs. 3 and 4 were caused by the effects of the partial volume. In this study, the pixel size of the measurement points in EBT was 0.17 mm while the mean value in the voxel in the data acquisition area in EGS5 was calculated. Therefore, the steep dose change in the vicinity of the gold ball was calculated to be gentler by the effect of partial volume in EGS5. The cause for the differences between the MC simulation and the RTPS is thought that the RTPS cannot calculate precisely the dose of the backscatter radiation, the frontscatter radiation, the lateral scatter radiation, the lack of secondary electron equilibrium, and etc [2, 3].

Practically, the size of a gold marker is different between facilities. Therefore, it is necessary to consider the effect of the size of the marker. It has been reported that large reduction in dose enhancement along the central axis is observed for the diameter changing from 2 cm to 0.5 cm though it is not observed from infinitely large to 2 cm [3]. And it is expected that large reduction in dose enhancement along the central axis is observed for the diameter changing from 0.5 cm to 0.2 cm. Therefore, the size of a gold marker may be as small as possible.

As for RTPS, the dose perturbation near the metal cannot be accurately expressed. Though EBT can measure, it is limited to a special situation like the phantom experiment. As for MC simulation, it seems that the evaluation in the situation near clinical is possible because it is computable in various situations.

The results of MC simulation fill 160% or less homogeneity index (HI) in clinical enough [12]. It is necessary to avoid the dose increment to organ at risk though it is thought that the irradiation execution is possible.

### 5. Conclusions

In this study, the effects of scattered radiation due to a gold internal fiducial marker in virtual lung phantom were

investigated. The dose increment and decrement by the scattering radiation were able to be confirmed by the MC simulation and the film measurement within  $\pm 0.5$  cm in the vicinity of the marker to the lateral direction. And from these results, there is a possibility of an overestimated dose or underestimated dose in the vicinity of the marker in the RTPS calculation.

## References

- 1) H. Shirato, T. Harada, T. Harabayashi, et al., "Feasibility of insertion/implantation of 2.0-mm-diameter gold internal fiducial markers for precise setup and real-time tumor tracking in radiotherapy," *Int. J. Radiat. Oncol. Biol. Phys.*, **56**, 240-247 (2003).
- 2) Otto A. Sauer, "Calculation of dose distributions in the vicinity of high-Z interfaces for photon beams," *Med. Phys.* **22**, 1685-1690 (1995).
- 3) X. Allen Li, James C. H. Chu, et al., "Dose enhancement by a thin foil of high-Z material: A Monte Carlo study," *Med. Phys.* **26**, 1245-1251 (1999).
- 4) M. Miyazawa, "The dosimetry procedure with Gafchromic Film," *Jpn. J. Radiol. Technol.*, **62**, 1428-1436 (2006).
- 5) L. Menegotti and A. Delana, "Radiochromic film dosimetry with flatbed scanners: A fast and accurate method for dose calibration and uniformity correction with single film exposure," *Med. Phys.* **35**, 3078-3085 (2008).
- 6) "Portugal-Japan Cork Industrial Association" [online], available at <http://www014.upp.so-net.ne.jp/pjcia/>
- 7) "Slab phantoms of tough series for treatment", Kyoto kagaku co.,LTD
- 8) D. Sheikh-Bagheri and D. W. O. Rogers, "Monte Carlo calculation of nine megavoltage photon beam spectra using the BEAM code," *Med. Phys.* **29**, 391-402 (2002).
- 9) P. Carrasco, N. Jorret, et al., "Comparison of dose calculation algorithms in slab phantoms with cortical bone equivalent heterogeneities," *Med. Phys.* **34**, 3323-3333 (2007).
- 10) B. Vanderstraeten, N. Reynaert, et al., "Accuracy of patient dose calculation for lung IMRT: A comparison of Monte Carlo, convolution/superposition, and pencil beam computations," *Med. Phys.* **33**, 3149-3158 (2006).
- 11) B. Mijnheer, A. Olszewska, et al., "Quality assurance of treatment planning systems-practical examples for non-IMRT photon beams," ESTRO Booklet No.7.
- 12) M. Hiraoka, Y. Nagata, et al., "JCOG0403," JCOG

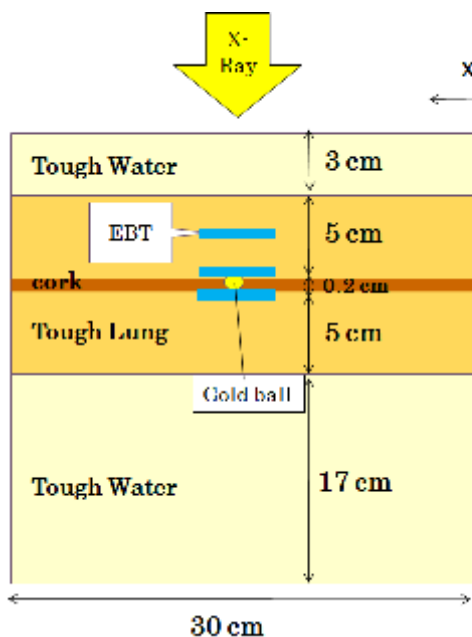


Figure 1. The geometry of film measurement.

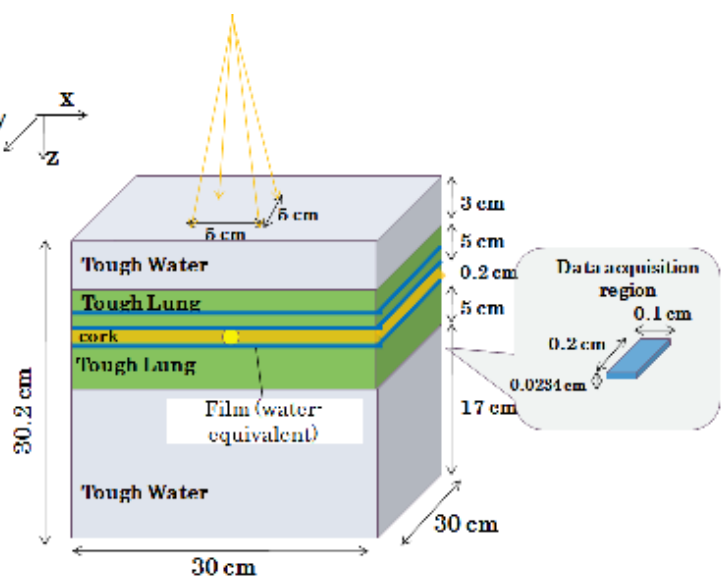
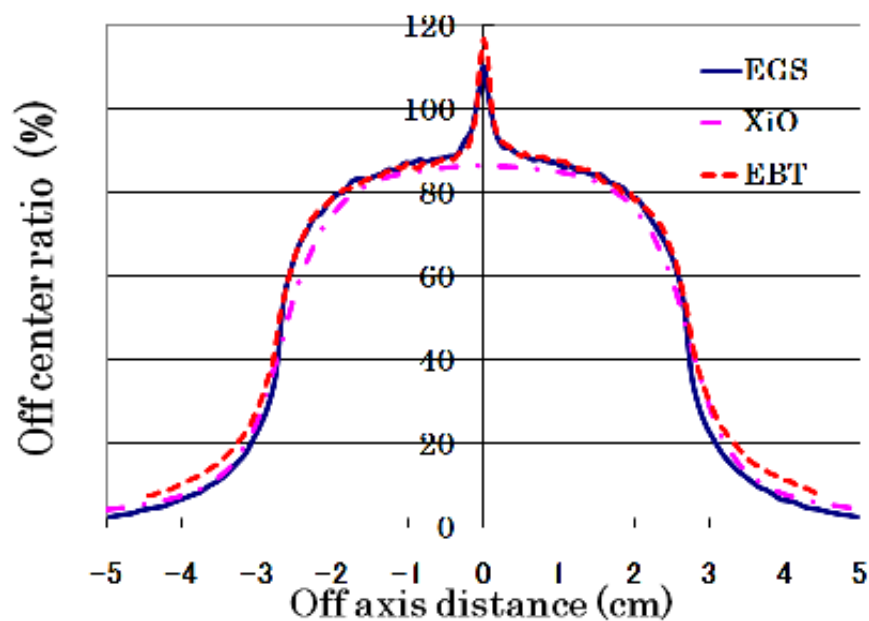


Figure 2. The geometry of MC simulation.

**Table 1** The compositions of the materials of the virtual lung phantom

Materials	Element composition (%)	Density [ $\text{g}/\text{cm}^3$ ]
Water	H(33.33), O(66.67)	1.000
Tough water	H(8.20), C(66.26), N(2.20), O(20.71), Cl(0.37), Ca(2.27)	1.018
Tough lung	H(7.00), C(50.20), O(35.10), P(0.10), Cl(1.00), Al(1.50), Si(5.00)	0.320
Cork	H(6.78), C(53.87), O(39.35)	0.300
Gold ball	Au(100.0)	19.300



**Figure 3.** Comparison among the results of the MC simulation (:EGS), film measurement (:EBT) and RTPS calculation (:XiO) at the incident side of gold.

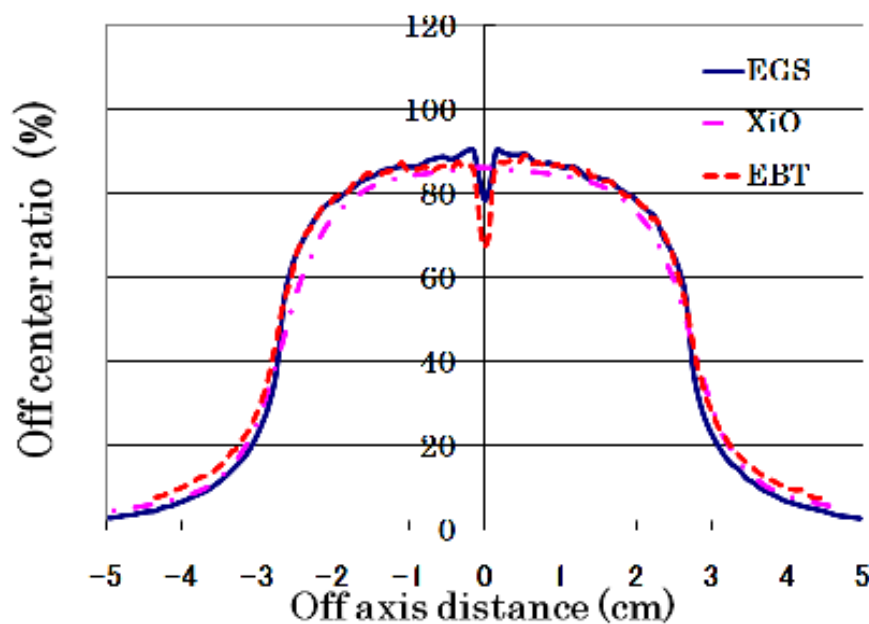


**Figure 4.** Comparison among the results of the MC simulation (:EGS), film measurement (:EBT) and RTPS calculation (:XiO) on the exit side of gold.

## Comparison of output factor obtained by measurement and radiation treatment planning system in a lung tissue

Y.Igarashi<sup>1</sup>, Y.Aoyama<sup>3</sup>, Y.Obata<sup>2</sup>, K.Habara<sup>1</sup>, T.Shimozato<sup>2</sup>, M.Komori<sup>2</sup>

<sup>1</sup>Department of Radiological Technology Graduate School of Medicine, Nagoya University  
1-1-20, Daikou-Minami Higashi-ku, Nagoya, Japan

<sup>2</sup>Department of Radiological Technology, School of Health Science, Nagoya University

<sup>3</sup>Department of Radiology, Nagoya University Hospital

email: [igarashi.yukinori@g.mbox.nagoya-u.ac.jp](mailto:igarashi.yukinori@g.mbox.nagoya-u.ac.jp)

### Abstract

In these day, dose distributions inside patients are calculated using Radiation Treatment Planning System (RTPS). For the radiotherapy, dose calculation algorithms need high accuracy and reliability.

In this work, dose calculation algorithms were evaluated by calculating output factor (OPF) using lung-equivalent phantom. The OPF was measured using an ionization chamber and calculated by Monte Carlo (MC) simulation or RTPS. By these evaluations, we investigated the accuracy of calculation method. Rates of change (RC) obtained using the MC simulation and the RTPS were larger values for a small field size than for a large field size (shown in Table1 and Table2), where  $RC(\%) = ((OPF_{RTPS \text{ or EGS}} - OPF_{\text{measure}}) / OPF_{\text{measure}}) \times 100$ . As a whole, AAA (analytical anisotropic algorithm) calculation and the MC simulation show relative high accuracy, but PBC (pencil beam convolution) calculation shows low accuracy.

## 1. Introduction

In recent years, radiotherapy technology has been developed. With the advance of technology and the complication of irradiation, dose calculation algorithm by using Radiation Treatment Planning System (RTPS) was requested to be highly accurate. In this work, by calculating output factor (OPF) using by lung-equivalent phantom (tough lung phantom, Kyoto kagaku co.,LTD) as a low density material, dose calculation algorithms were evaluated. OPFs were obtained using measured values by an ionization chamber, Monte Carlo (MC) simulations and RTPS calculations. By comparing these values, the accuracy of the dose calculation algorithms was investigated.

## 2. Materials and Methods

### 2.1 Ionization chamber measurement to obtain OPFs

We used tough lung phantoms, tough water phantoms (Kyoto kagaku Co.,LTD) and the data was measured by an ionization chamber (PTW Type 30013) and an electrometer (PTW UNIDOS). 6 and 10 MV photon beams from a medical linear accelerator Clinac 2100 CD (Varian medical systems) were used to obtain sufficient quantity of the ionization. Field sizes were  $7\times 7$ ,  $10\times 10$ , and  $15\times 15$  cm<sup>2</sup> and measurement depths were 5, 10, and 20 cm. In the measurement, source axis distance (SAD) was 100 cm and the geometry is shown in Fig. 1. The measurement using the ionization chamber was repeated three times at each depth or each field. The measurement values were revised against temperature and pressure correction factors, and the OPF was calculated for each condition. The OPF is defined by  $D_r(A)/D(A=10\times 10$  cm<sup>2</sup>), where  $D_r(A)$  is the absorbed dose at the reference point r for field size A, the depth of r is 10 cm.

### 2.2 RTPS calculations to obtain OPFs

At first, lung phantoms were scanned by a computed-tomography (CT) equipment. The scan situation is shown in Fig. 2. Scan data acquired by CT were sent to a commercial RTPS Eclipse (Varian medical systems). The calculation algorithms were AAA algorithm and PBC algorithm. These algorithms have different characteristics. The AAA algorithm can take the change of side scatter with a low density tissue into account because Kernel is extended in the low density tissue and shrunked in the high density tissue. On the other hand, the PBC algorithm cannot take the change of side scatter with the low density tissue into account because Kernel can only be extended or shrunked by density scaling along the axis, also it cannot revise Kernel to the vertical direction of the pencil beam. We acquired monitor-units (MU) and dose/MU at the reference depth and then calculated OPFs.

### 2.3 Monte Carlo simulations to obtain OPFs

Electron Gamma Shower version 5 (EGS5) of the MC simulation code was used to obtain OPFs. In the MC simulations, the simulation geometry was accurately reconstructed from the measurement geometry as shown in Fig. 1. The composition of the tough lung phantom is H: 7.0, C: 50.2, O: 35.1, P: 0.1, Al: 1.5, Cl: 1.0, Si: 5.0 (percentage by weight, %) and the density is 0.32 g/cm<sup>3</sup>. Also, in regard to the composition of the tough water phantom, we used to water in place of the tough water phantom because percentage depth dose (PDD) of the tough water phantom and water were not so different. Data acquisition region was allocated on the center of field and the voxel size was 0.5 x 0.5 x 0.5 cm<sup>3</sup>. Statistical uncertainties of the MC simulations were less than 1.0 %.

Energy spectra of photon beams were excerpted from published data for 6 MV and 10 MV photon beams of Varian in all simulations [1].

### **3. Results and discussion**

#### **3.1 Comparison between ionization chamber measurement and RTPS calculations**

OPFs at the depth of 5, 10, and 20 cm for 6 MV are shown in Figs. 3, 4, and 5, respectively. At 5 cm depth, the OPF calculated by the AAA method algorithm agreed within  $\pm 1.0\%$  with measurement for  $7 \times 7 \text{ cm}^2$ ,  $15 \times 15 \text{ cm}^2$  by the ionization chamber. At 10 cm depth, results at 10 cm depth were similar to those at 5 cm depth. However, at 20 cm depth, the OPF of  $7 \times 7 \text{ cm}^2$  field agreed within  $\pm 1.0\%$  with the measurement, while those of  $15 \times 15 \text{ cm}^2$  field did not. Also, OPFs for 10 MV are shown in Figs. 6, 7, and 8. Results calculated by the AAA algorithm were similar to those for 6 MV. On the other hand, OPFs calculated by the PBC algorithm did not agreed with measurement by the ionization chamber both for 6 and 10 MV. The maximum of rates of change (RC) of the PBC method was  $-2.24\%$  for 6 MV, and was  $+2.87\%$  for 10 MV, As shown by these results, the accuracy of the calculation by the AAA method was higher than by the PBC method.

#### **3.2 Comparison between ionization chamber measurement and MC simulation**

Results calculated by the MC simulation agreed within  $\pm 1.0\%$  with the ionization chamber measurement at 5 and 10 cm depth for 6 MV. However, for 20 cm depth, the rate of change was more than  $+1.5\%$  as shown in Table 1 and Figs. 3- 5. Also, results calculated by the MC simulation agreed within  $\pm 1.0\%$  with measurement by the ionization chamber at 10 and 20 cm depth for 10 MV, but at 5 cm depth, the RC was more than  $+1.5\%$  as shown in Table 2 and Figs. 6- 8. However, as a whole, the accuracy of calculation by the MC method was thought to be considerable high.

### **4. Conclusions**

The accuracy of the calculation algorithm for low density materials was investigated in this work. OPFs obtained using the ionization chamber agreed with the AAA algorithm in the RTPS and with the MC simulation. In comparison of these results, as a whole, OPFs were larger than those of the measurement when the field size was small, while OPFs were smaller than those of the measurement when the field size was large. Thus, the same energy spectra of the beam may overestimate the low energy compositions in the small field and underestimate the low energy composition in the large field. For the dose calculation of low materials such as lung, the accuracy of calculation by the AAA algorithm in the RTPS and the MC simulations were

relatively high, while that by the PBC algorithm was low.

## References

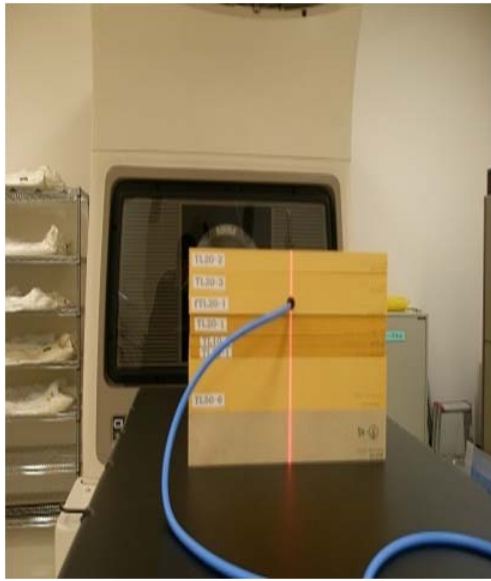
- 1) D.Sheikh-Bagheri and D.W.O.Rogers,"Monte Carlo calculation of nine megavoltage photon beam spectra using the BEAM code, "Med. Phys.,**29**, 391-402,(2002)
- 2) C. L. Chow, K.K. Leung and Jake Van Dyk,"Variations of lung density and geometry on inhomogeneity correction algorithms: A Monte Carlo dosimetric evaluation, "Med. Phys.,**36**, 3619-3630,(2009)

Table 1 The rate of change (RC) of the RTPS calculation and the MC simulations for 6 MV

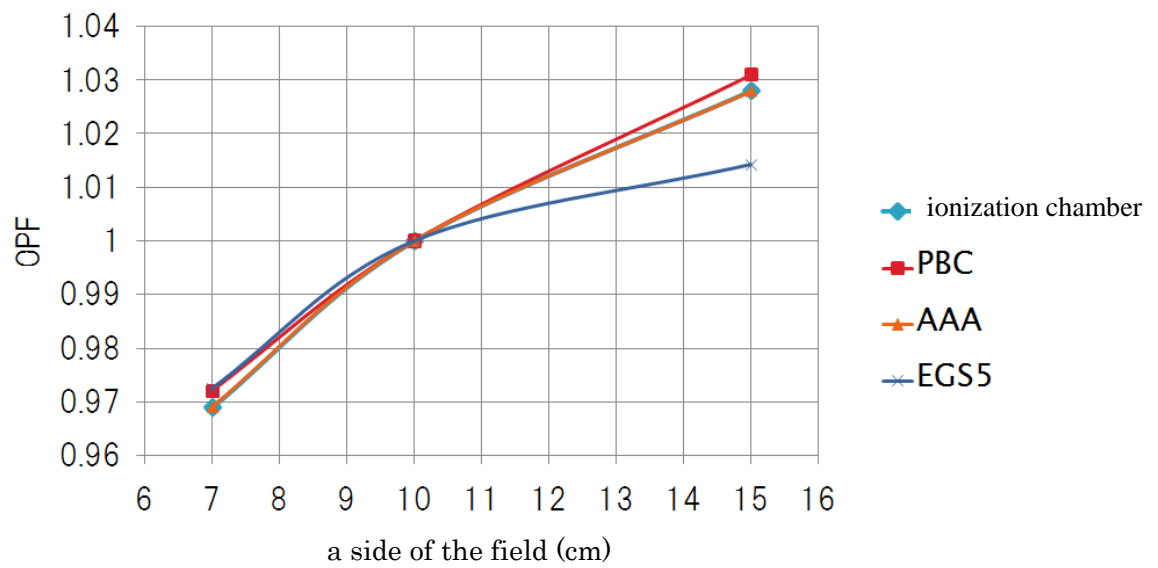
depth (cm)	field (cm <sup>2</sup> )	PBC method	AAA method	EGS5
5	7×7	+0.31%	±0%	+0.41%
	15×15	+0.29%	±0%	-0.58%
10	7×7	+0.31%	+0.41%	+0.41%
	15×15	-0.78%	+0.09%	-0.39%
20	7×7	+1.47%	+0.93%	+0.20%
	15×15	-2.24%	-1.90%	-1.64%

Table 2 The rate of change (RC) of the RTPS calculation and the MC simulations for 10 MV.

depth (cm)	field (cm <sup>2</sup> )	PBC method	AAA Method	EGS5
5	7×7	+0.94%	+0.21%	+1.57%
	15×15	-0.67%	-0.38%	-0.87%
10	7×7	+2.00%	+0.63%	+0.63%
	15×15	-0.29%	-0.09%	-0.10%
20	7×7	+2.87%	+0.74%	+0.42%
	15×15	-0.86%	-0.86%	-0.58%



**Fig. 1** The geometry of the ionization chamber measurement    **Fig. 2** The situation of CT scan



**Fig. 3.** Output factors (OPFs) of the EGS simulation, the RTPS calculation and the ionization chamber measurement at depth of 5 cm for 6 MV

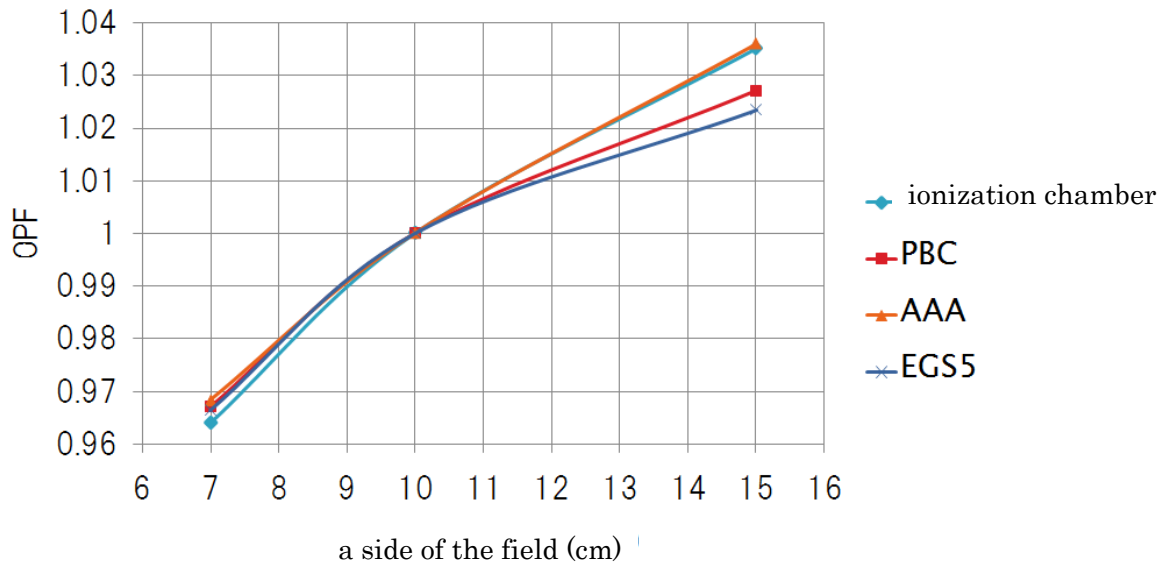


**Fig. 4.** Output factors (OPFs) of the EGS simulation, the RTPS calculation and the ionization chamber measurement at depth of 10 cm for 6 MV

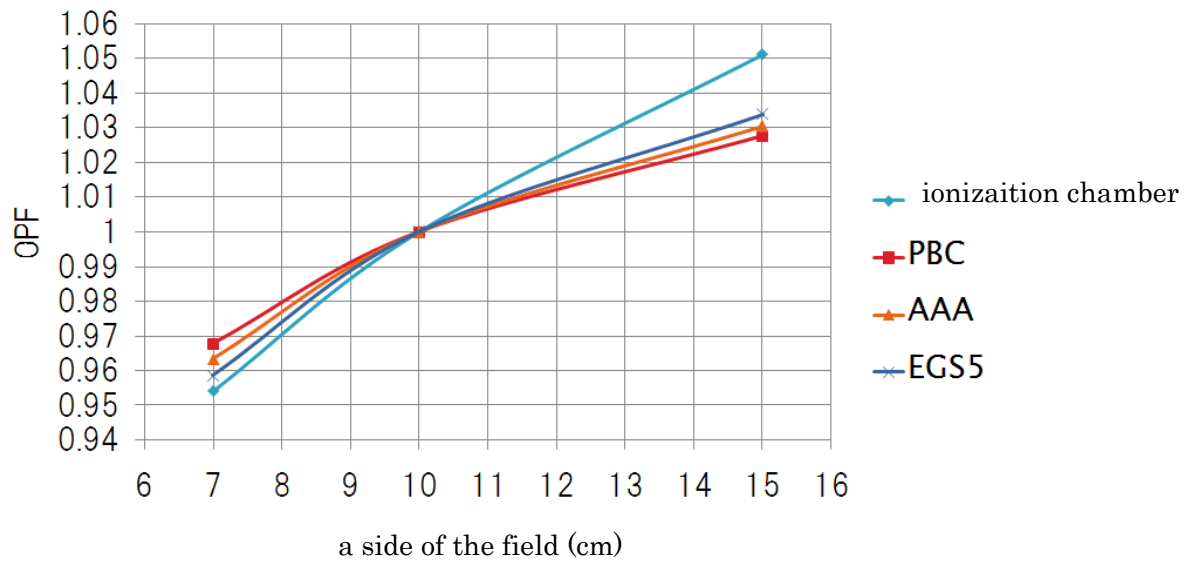


**Fig. 5.** Output factors (OPFs) of the EGS simulation, the RTPS calculation and the ionization chamber measurement at depth of 20 cm for 6 MV

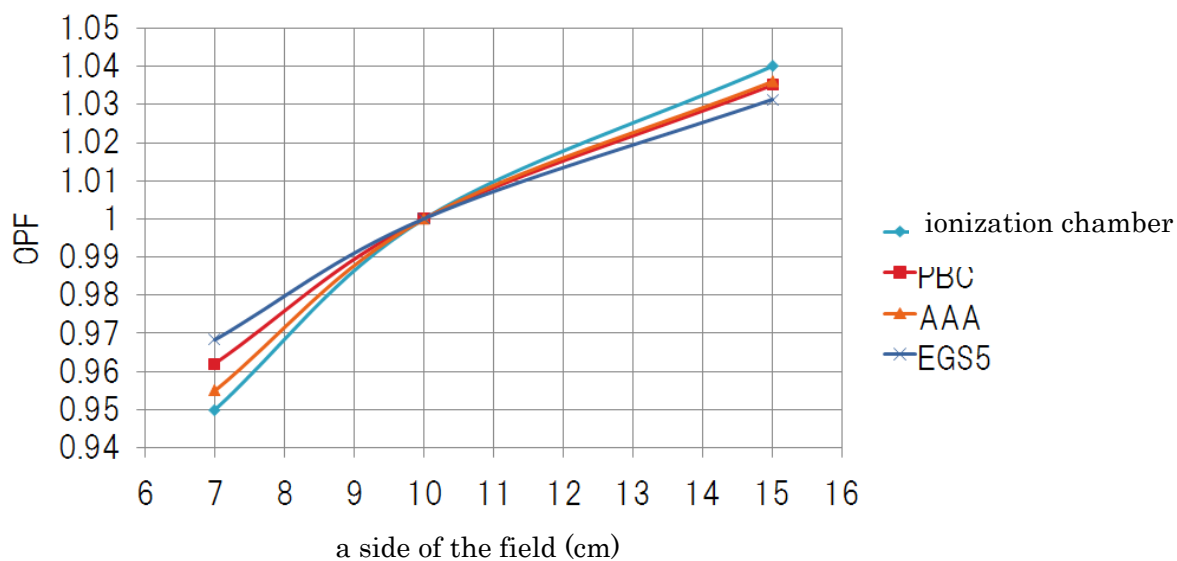


**Fig. 6.** Output factors (OPFs) of the EGS simulation, the RTPS calculation and the ionization chamber measurement at depth of 5 cm for 10 MV

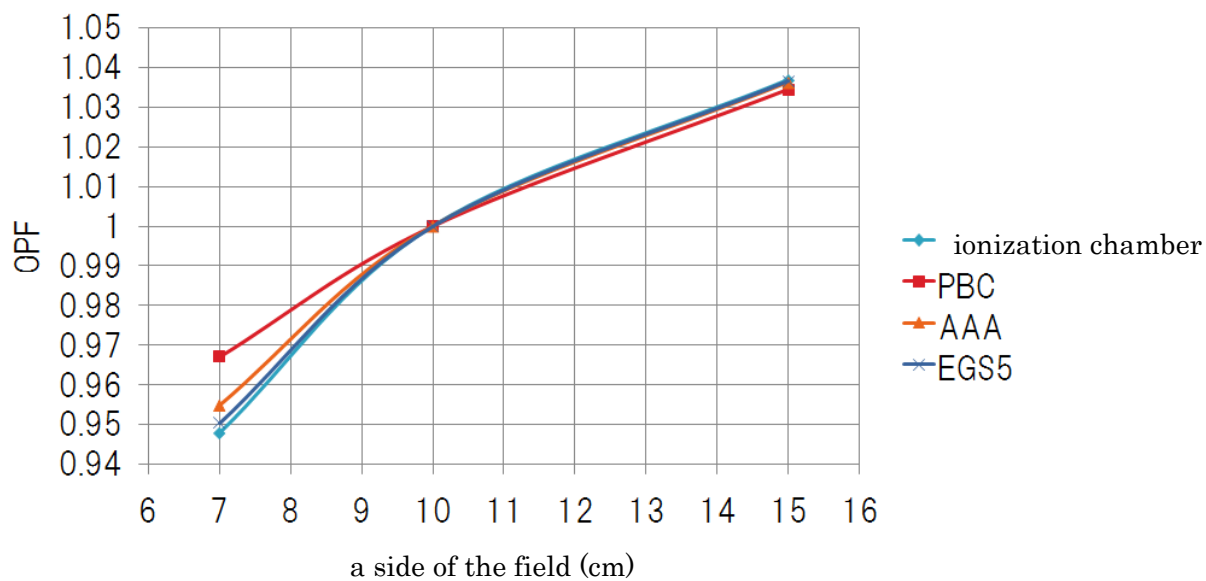


**Fig.7.** Output factors (OPFs) of the EGS simulation, the RTPS calculation and the ionization chamber measurement at depth 10 cm for 10 MV

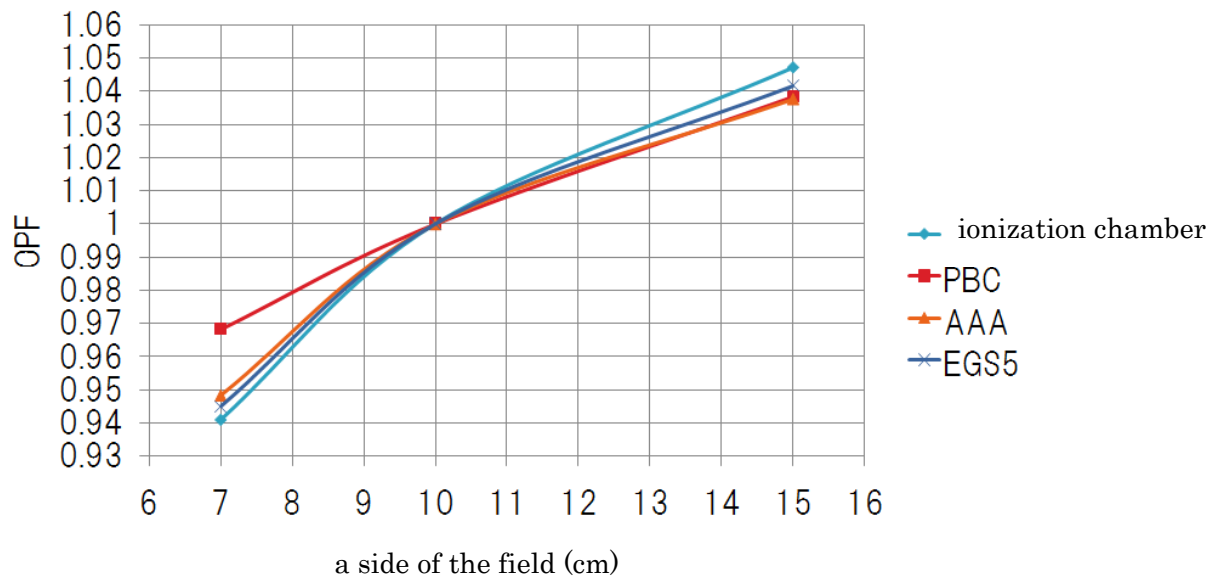


**Fig.8.** Output factors (OPFs) of the EGS simulation, the RTPS calculation and the ionization chamber measurement at depth of 20 cm for 10 MV

# Investigation for the calculation of absorbed dose in high-density bone material

T. Matsunaga<sup>1</sup>, T. Shimozato<sup>2</sup>, Y. Aoyama<sup>1,3</sup>, M. Komori<sup>2</sup>, and Y. Obata<sup>2</sup>

<sup>1</sup>*Department of Radiological Technology, Graduate School of Medicine, Nagoya University  
1-1-20 Daikou-Minami, Higashi-ku, Nagoya, Japan*

<sup>2</sup>*Department of Radiological Technology, School of Health Science, Nagoya University*

<sup>3</sup>*Department of Radiology, Nagoya University Hospital*

*E-mail: matsunaga.takuma@h.mbox.nagoya-u.ac.jp*

## Abstract

Dosimetry protocols provide a set of correction factors for converting an ionization into a dose, but only for water-equivalent at a reference depth. The correction factors inside the bone-equivalent material should differ from those factors in water. We calculated the correction factor inside the bone-equivalent materials using Monte Carlo (MC) simulation. We converted the measured percentage depth ionization to the percentage depth dose (PDD) using this correction factor. The discrepancies between the converted PDD and the MC PDD ranged from - 0.2 to 1.4 % inside the bone-equivalent materials. In addition, we investigated the accuracy of the calculation in the radiation treatment planning systems. The doses calculated by MC are sufficiently accurate just before or at the side of the inhomogeneity due to the contribution of scatter doses from the high-density material. Convolution/Superposition algorithm does not provide the accurate calculation of the effect by scattered radiation.

## 1. Introduction

The effect of heterogeneity on dose distributions and dose calculations is an issue that has concerned the medical physics field for almost three decades. Dosimetry protocols [1] provide a set of correction factors for converting an ionization into a dose, but only for water at a reference depth. Therefore, an ionization chamber can be used only in the water-equivalent regions of the phantom as these correction factors inside the bone-equivalent material should differ from those in water [2].

In the radiation treatment planning systems (RTPS), the accuracy of patient dose predictions has been continuously improved. The Convolution/Superposition (CS) algorithms have been recently implemented. However, larger errors in the calculated doses occur in the vicinity of tissue heterogeneities [3].

The aim of this work is to evaluate absorbed doses in heterogeneous slab phantoms with the bone-equivalent heterogeneity by means of comparing with the MC simulations.

## 2. Materials and Methods

Measurements, RTPS calculations, and MC simulations were performed for a field size of 10 x 10 cm<sup>2</sup> with a constant source-to-surface distance (SSD) of 100 cm for 6 and 10 MV (measurements), for 10 MV (RTPS calculations) x-ray beams from a Clinac 2100C/D (Varian Medical Systems) linear accelerator, and for 6 and 10 MV x-ray beams of Varian (MC simulations) [4], respectively.

All measurements and calculations are made for slab phantoms of water-equivalent materials (Tough Water : TW, Kyoto Kagaku Co., LTD), bone-equivalent materials (Tough Bone : TB, Kyoto Kagaku Co., LTD), and lung-equivalent

materials (Tough Lung : TL, Kyoto Kagaku Co., LTD). The size of the slabs is 30 x 30 cm<sup>2</sup> with the thickness ranging from 0.5 to 5 cm. The composition in weight, mass density, and relative electron density of each materials are detailed in Table I. Five configurations were studied (Fig. 1 (a)-(e)).

An absorbed dose in materials other than water is difficult to determine with standard ionization chambers because chamber correction factors are not known for these materials [5]. The AAPM Report No. 85 [6] indicates an inhomogeneity correction factor (ICF) for converting the ionization into the dose inside bone-equivalent materials as follow.

$$ICF_{bone} = \frac{(\bar{L}/\rho)_{gas}^{bone} \cdot P_{bone}}{(\bar{L}/\rho)_{gas}^{water} \cdot P_{water}} \quad (1)$$

where  $(\bar{L}/\rho)_{gas}^{mat}$  is average restricted mass collision stopping power ratio (SPR) of material to air and  $P_{mat}$  is perturbation correction factor of material.

## 2.1 PDI measurements

The percentage depth ionization (PDI) curves were obtained by means of a cylindrical ionization chamber with 0.6 cm<sup>3</sup> volume (PTW 30013, PTW-Freiburg), which was connected to the electrometer UNIDOS (PTW-Freiburg). Measurements were carried out at depths of 12 points on the central axis of the beam ranging from 1.0 to 12.0 cm for Fig. 1 (a).

## 2.2 RTPS calculations

A commercial RTPS XiO (Version 4.33.02, CMS, Inc) was adopted. The CS algorithm was selected for all calculations and calculation voxel size was 0.2 x 0.2 x 0.2 cm<sup>3</sup>. The dose distributions were calculated for Fig. 1 (b)-(e). In addition, the PDD curves were obtained by geometry shown in Fig. 1 (b)-(c), and the dose profiles at depths of 7.5 cm (Fig. 1 (d)) and 12.5 cm (Fig.1 (e)) where are the depth of center of TB were obtained.

## 2.3 MC simulations

EGS 5 [7] and EGSnrc [8] MC code system were used to MC simulation. The simulation geometries were reconstructed accurately from the measurements and RTPS calculations geometries (Fig. 1 (a)-(e)). The cut-off energies for the transport calculation of electron (ECUT) and photon (PCUT) in all simulations were set to 521 and 10 keV, respectively. For obtaining relative doses, deposited energies at each region of interest divided mass density of each material are computed and normalized with the energy at the peak point. Energy spectra of photon beams were excerpted from published data for 6 and 10 MV photon beams of Varian in all simulations [4]. The MC PDD curves and the measured PDD curves using water phantom for 6 MV and 10 MV agreed within 1.5 % discrepancies except the buildup regions.

Data acquisition regions of the PDD curve for Fig. 1 (a) were allocated on the central axis of the beam and each voxel size was 0.5 x 0.5 x 0.05 cm<sup>3</sup>. Statistical uncertainties were less than 1.0 % at all depths.

Data acquisition regions of the PDD curve for Fig. 1 (b)-(e) were allocated the plane including the central axis of the beam and each voxel size was 0.2 x 0.2 x 0.2 cm<sup>3</sup>. Statistical uncertainties were less than 2.0 % at the side of 7.5 cm from the central axis of the beam. In addition, the PDD curves were obtained for Fig. 1 (b)-(c), and the dose profiles at depth of 7.5 cm (Fig. 1 (d)) and 12.5 cm (Fig. 1 (e)) were obtained.

The SPR for Fig. 1 (a) was calculated using the EGSnrc/SPRRZnrc [9] code. The perturbation correction factors of TW and TB were calculated using the EGS 5. Fig. 2 shows the schematic representation of the calculation geometries arranged to compute the perturbation correction factor. The perturbation correction factor was computed as the ratio of doses  $[D_{air}]_{none} / [D_{air}]_{chamber}$ .  $[D_{air}]_{none}$  is the dose to the sensitive volume in the air cavity for the chamber wall composed entirely of TW or TB.  $[D_{air}]_{chamber}$  is the dose to the real chamber geometry. Fig. 2 demonstrates simple chamber geometries, but in EGS 5 calculations, detailed chamber geometries were used according to the manufacturers' specifications [10].

### 3. Results and Discussion

#### 3.1 Converting measured PDI into PDD and comparison with MC PDD

Figs. 3 (a)-(b) show SPR for Fig. 1 (a) for 6 and 10 MV, respectively. The perturbation correction factor of TW and TB were 0.997, 1.037 for 6 MV, and 0.999, 1.022 for 10 MV, respectively. Using above factors and Eq. (1), ICF were calculated: 0.968 for 6 MV, and 0.956 for 10 MV. Figs. 4 (a)-(b) show measured PDI, converted PDD using ICF (cPDD), and MC PDD curves for 6 and 10 MV, respectively. PDI and MC PDD curves agreed within 3.0 to 4.8 % discrepancies for 6 MV, and 4.4 to 4.8 % for 10 MV inside the TB, where discrepancies =  $((\text{PDI} - \text{MC PDD}) / \text{MC PDD}) \times 100 (\%)$ . cPDD and MC PDD agreed within -0.2 to 1.4 % discrepancies for 6 MV, and -0.2 to 0.2 % for 10 MV inside the TB, where discrepancies =  $((\text{cPDD} - \text{MC PDD}) / \text{MC PDD}) \times 100 (\%)$ .

To convert the ionization to the dose inside the materials except for water, we have to think about the SPR. Especially, inside high-density materials, we have to be careful about the shift of the perturbation correction factor. Accurate conversion will contribute to evaluate absorbed dose and radiation damage of the irradiated bone.

#### 3.2 Comparison RTPS with MC

Figs. 5 (a)-(d) show the dose distributions for Fig. 1 (b)-(e) calculated by XiO and EGS 5. Figs. 6 (a)-(b) show the PDD curves for Figs. 1 (b)-(c), and Fig. 7 (a)-(b) show the dose profiles at depth of 7.5 cm (Fig. 1 (d)) and 12.5 cm (Fig. 1 (e)) calculated by XiO and EGS 5. Near the TB, the discrepancies between XiO and EGS 5 were 4.6 % (Fig. 6 (a)), 3.5 % (Fig. 6 (b)) in front of TB, 3.6 % (Fig. 6 (a)), 2.8 % (Fig. 6 (b)) at behind of TB, 4.7 % (Fig. 7 (a)), 2.0 % (Fig. 7 (b)) at the side of TB. As the depth was shallower, the discrepancies were larger.

In the region before or forward or at the side of the high-density material the doses produced by the CS algorithm introduce some errors. That is, those doses are underestimated or overestimated (Figs. 5-7). The doses calculated by MC increase just before or at the side of the inhomogeneity due to the contribution of the radiation scattered from high-density material and decrease forward of the high-density material due to the contribution of the collapse of electron equilibrium. The CS algorithm does not provide the accurate calculation of the scatter effect. The enhancement by scattered radiation is a well known phenomenon for the beam penetrating from lower to higher relative electron density materials [5, 11]. For the beam penetrating from higher to lower relative electron density materials, the dose is decreased due to collapse of electron equilibrium.

### 4. Conclusions

We could convert the ionization to the dose considering SPR of bone to air and the perturbation correction factor of the ionization chamber inside the high-density bone material.

In the region before or forward or at the side of the high-density bone material, the CS algorithm underestimated the MC doses in the before or at the side region as the CS algorithm fails to predict the well-known dose enhancement just near the high-density bone material due to increased scatter and the CS algorithm overestimated the MC doses in the forward region as the CS algorithm fails to predict the collapse of electron equilibrium for the beam penetrating from higher to lower relative electron density materials.

### References

- 1) "JSMP: Standard Dosimetry of Absorbed Dose for External Radiotherapy," Tsusho-Sangyo Kenkyu-sha, 96-141, (2006).
- 2) P. Carrasco, N. Jornet, M. A. Duch, V. Panettieri, L. Weber, T. Eudaldo, M. Ginjaume, and M. Ribas, "Comparison of dose calculation algorithms in slab phantoms with cortical bone equivalent heterogeneities," *Med. Phys.* **34**, 3323-3333, (2007).
- 3) T. Krieger and O. A. Sauer, "Monte Carlo versus pencil-beam/collapsed cone dose calculation in a heterogeneous

- multi-layer phantom,” *Phys. Med. Biol.* **50**, 859–868, (2005).
- 4) D. Sheikh-Bagheria and D. W. O. Rogers, “Monte Carlo calculation of nine megavoltage photon beam spectra using the BEAM code,” *Med. Phys.* **29**, 391–402, (2002).
  - 5) F. DeBlois, W. A. Rahman, J. P. Seuntjens, and E. B. Podgorsak, “Measurement of absorbed dose with a bone-equivalent extrapolation chamber,” *Med. Phys.* **29**, 433–440, (2002).
  - 6) N. Papanikolaou, J. J. Battista, A. L. Boyer, C. Kappas, E. Klein, T. R. Mackie, M. Sharpe, and J. Van Dyk, “AAPM Report No. 85: Tissue inhomogeneity corrections for megavoltage photon beams,” Report of Task Group No. 65 Medical Physics Publishing, Madison, (2004).
  - 7) H. Hirayama, Y. Namito, A. F. Bielajew, S. J. Wilderman, and W. R. Nelson, *The EGS5 Code System*, SLAC-R-730 Stanford Linear Accelerator Center, Stanford, CA, (2005).
  - 8) I. Kawrakow and D. W. O. Rogers, “The EGSnrc code system: Monte Carlo Simulation of Electron and Photon Transport,” National Research Council of Canada Report PIRS-701, (2002).
  - 9) D. W. O. Rogers, I. Kawrakow, J. P. Seuntjens, B. R. Walters, and E. Mainegra-Hing, “NRC User Codes for EGSnrc,” National Research Council of Canada Report PIRS-702 Rev B, (2005).
  - 10) F. Araki, “Monte Carlo calculations of correction factors for plane-parallel ionization chambers in clinical electron dosimetry,” *Med. Phys.* **35**, 4033–4040, (2008).
  - 11) M. Farahani, F. C. Eichmiller, W. L. McLaughlin, “Measurement of absorbed doses near metal and dental material interfaces irradiated by x-ray and gamma-ray therapy beams,” *Phys. Med. Biol.* **35**, 369–385, (1990).

Table I. Element composition, mass density, and relative electron density to water of the materials in this study

		Tough Water (TW)	Tough Bone BE-H (TB)	Tough Lung (TL)
Composition (%)	H	8.4	5.1	7.0
	C	67.4	42.5	50.2
	N	2.2	1.7	
	O	19.5	28.1	35.1
	P		7.0	0.1
	Al			1.5
	Cl	0.2	0.1	1.0
	Ca	2.3	15.5	
	Si			5.0
	Mass density (g cm <sup>-3</sup> )		1.017	1.5
Relative electron density to water		0.989	1.415	0.312

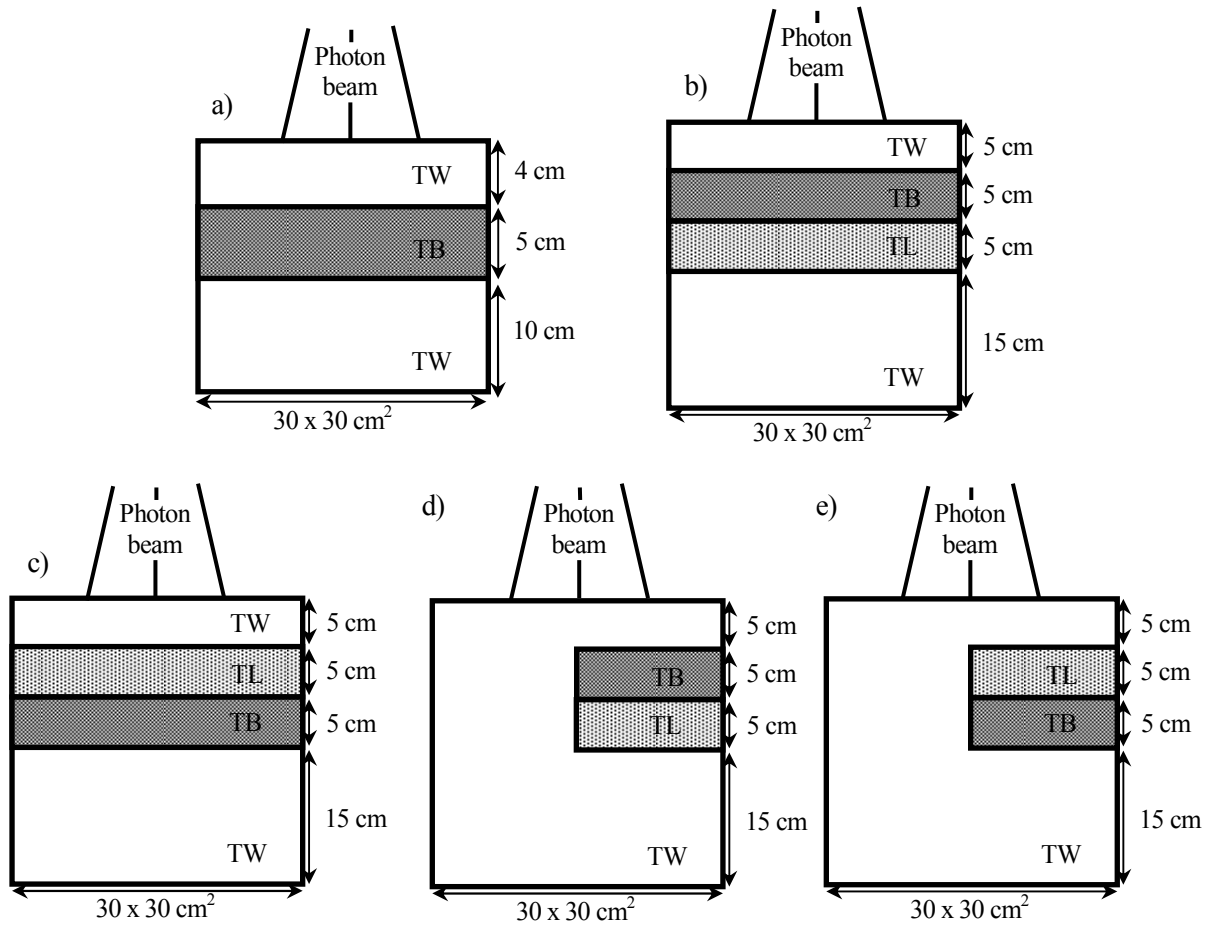


Fig. 1. Diagrams of the phantoms used in measurements and calculations

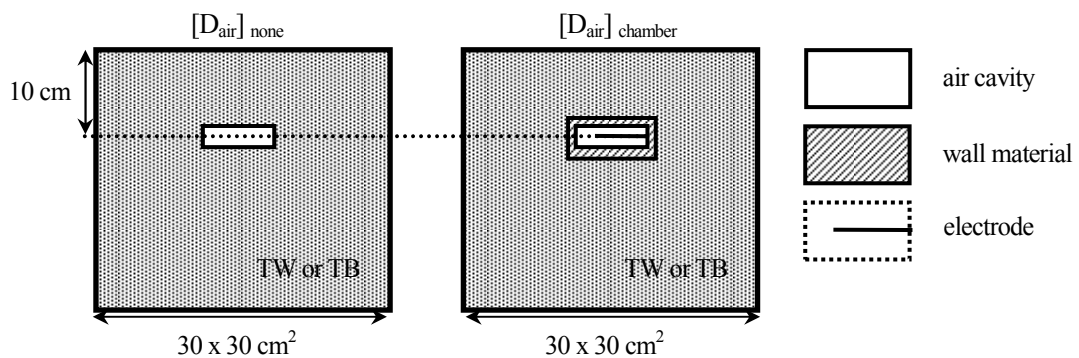


Fig. 2. Simplified schematic diagram of the two geometries used to compute the perturbation correction factor. The perturbation correction factor is computed as the ratio of doses  $[D_{air}]_{none} / [D_{air}]_{chamber}$  using EGS 5. The air cavity was  $6 \text{ mm}\Phi \times 23.6 \text{ mm}$ . The electrode was  $1.1 \text{ mm}\Phi \times 21.1 \text{ mm}$ , and material was Al. The wall thickness was  $0.335 \text{ mm}$ , and its material was PMMA.

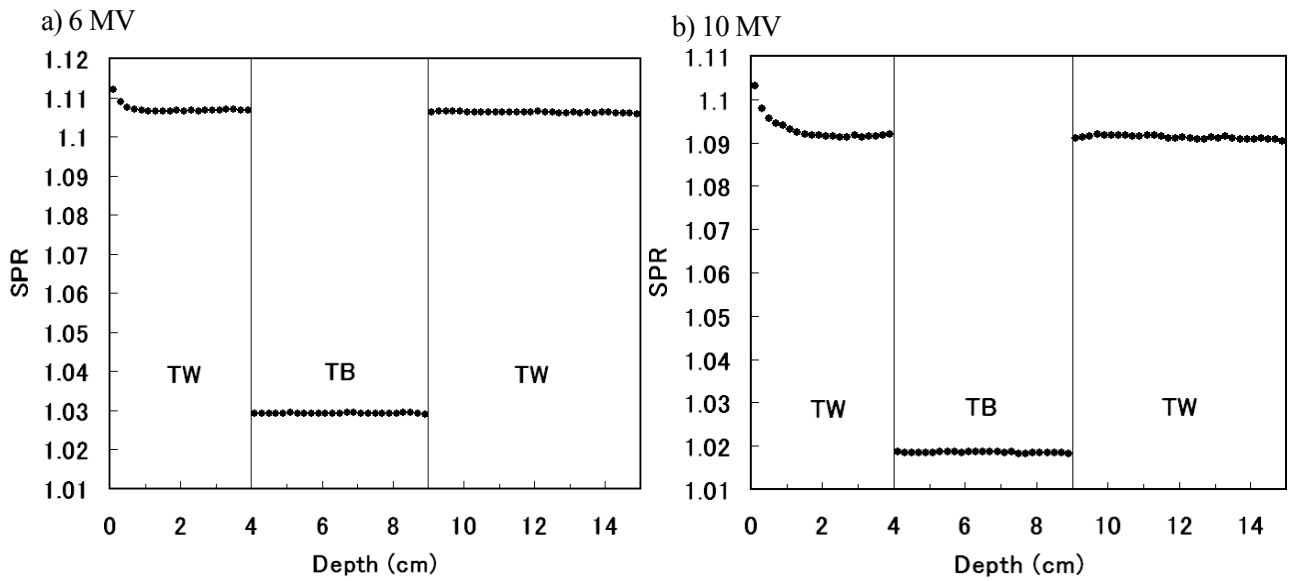


Fig. 3. Calculated SPR of TW to air or TB to air using EGSnrc/SPRRZnrc for (a) 6 MV and (b) 10 MV.

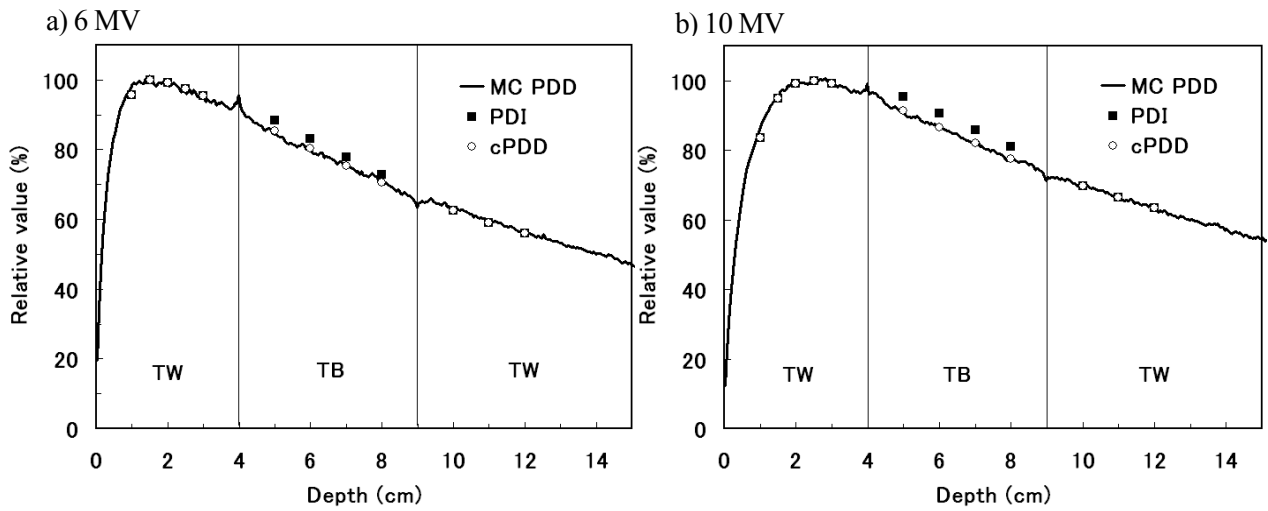
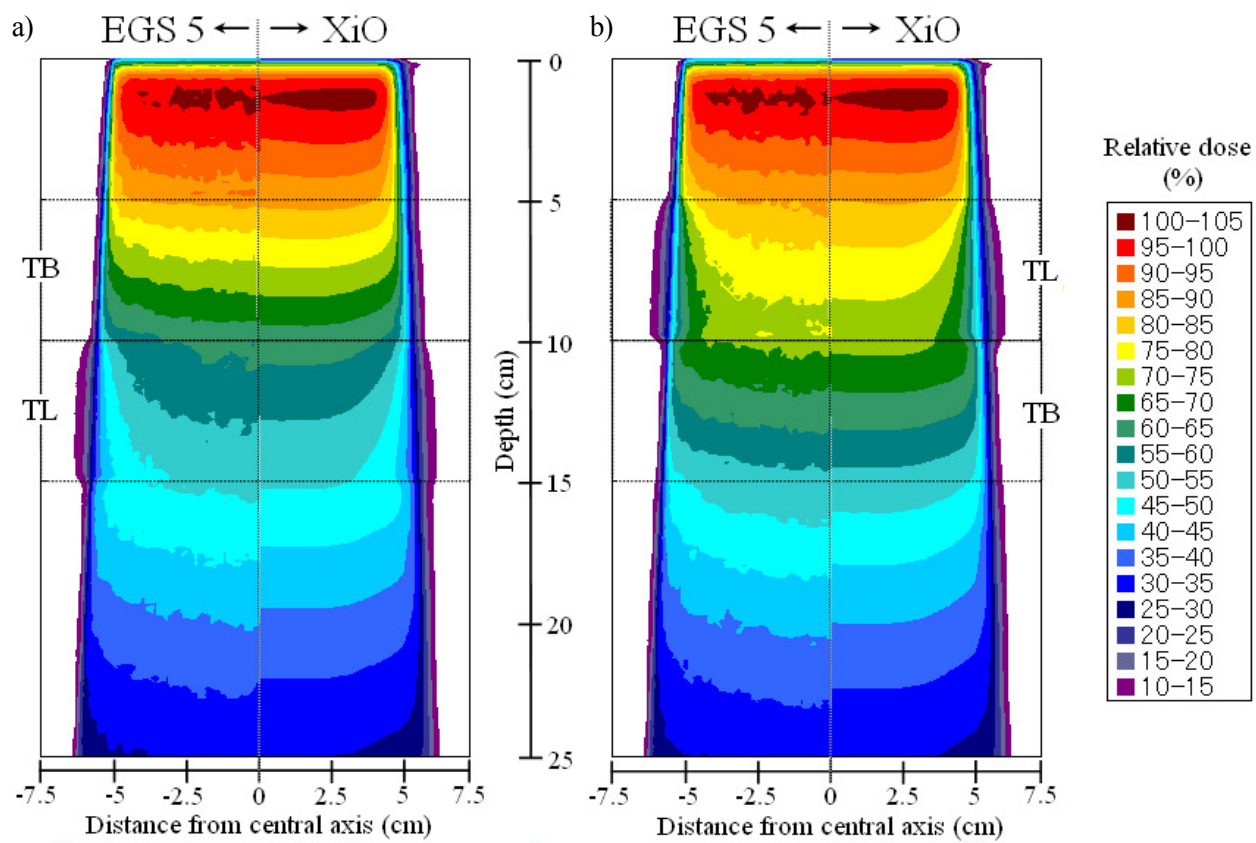


Fig. 4. Calculated PDD using EGS 5, measured PDI, and converted PDD using ICF from PDI (cPDD) for (a) 6 MV, and (b) 10 MV.



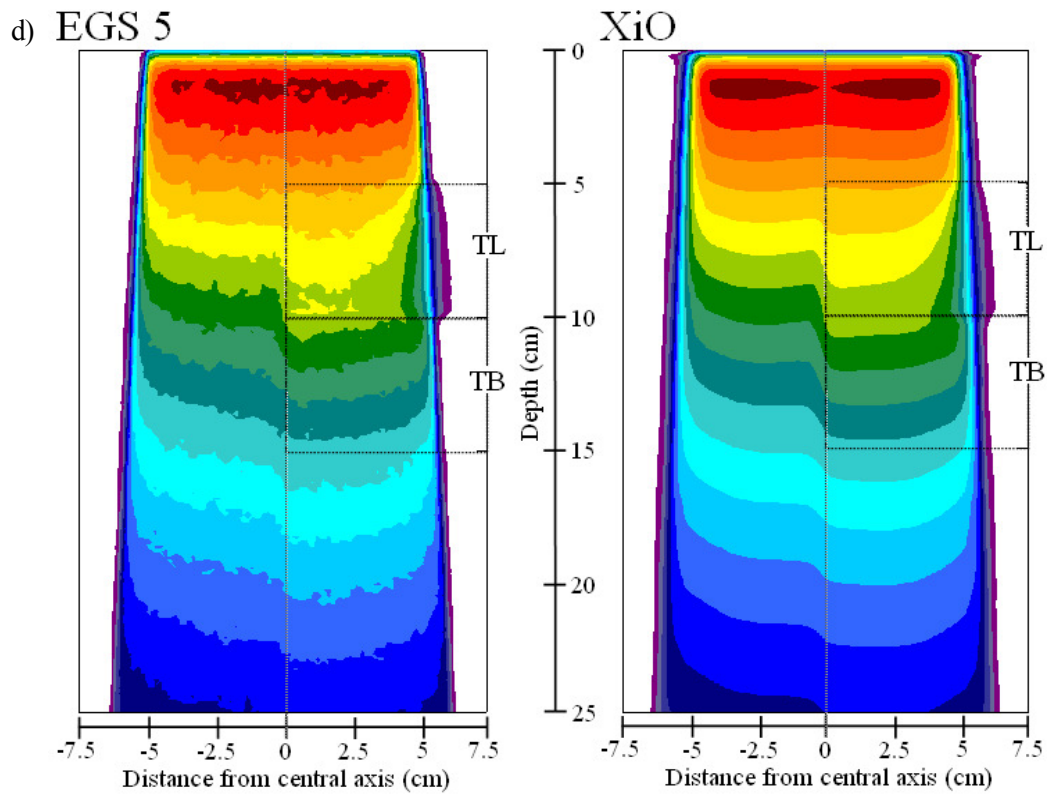
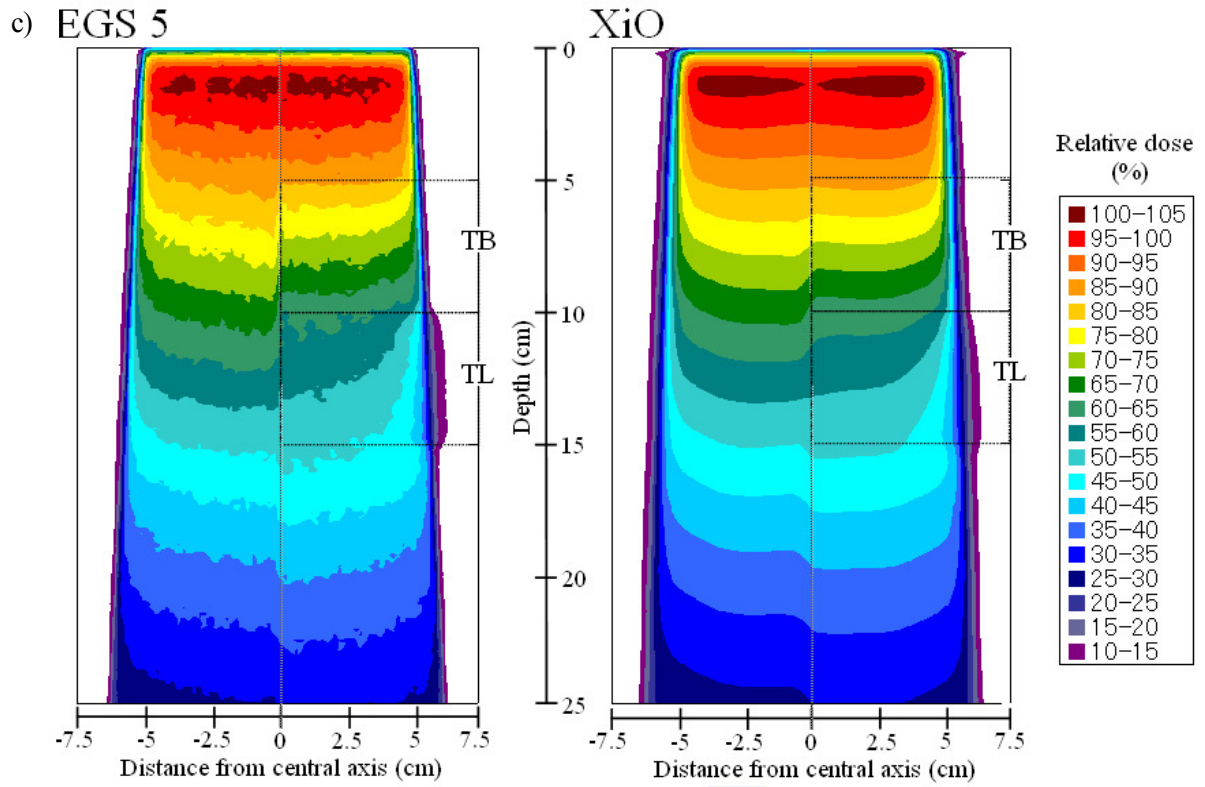


Fig. 5. Calculated dose distributions ((a)-(d)) using EGS 5 and XiO for Fig. 1 (b)-(e), respectively.

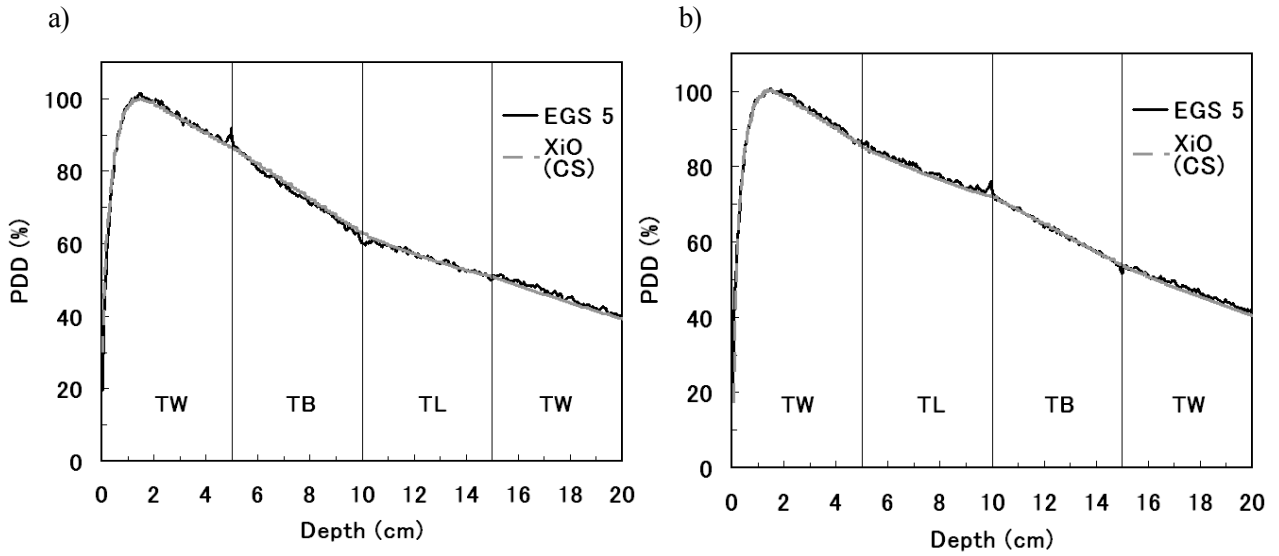


Fig. 6. Calculated PDDs ((a) and (b)) using EGS 5 and XiO (CS) for Fig. 1 (b) and (c), respectively

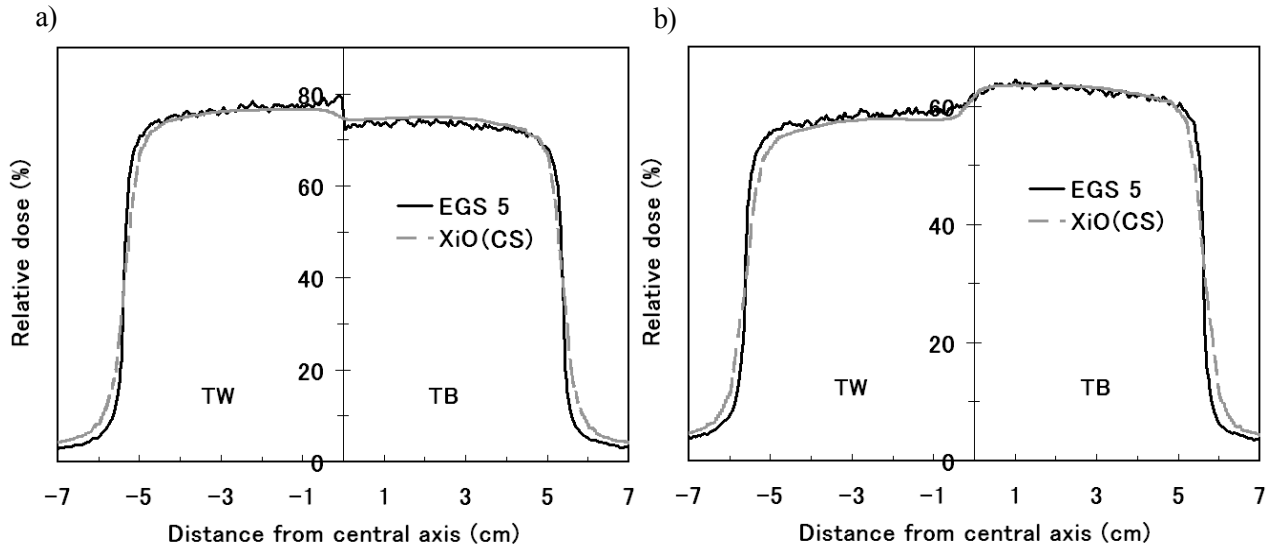


Fig. 7. Calculated dose profiles ((a) and (b)) at depth of 7.5 cm (Fig. 1 (d)) and 12.5 cm (Fig. 1 (e)), respectively.

# Development and validation of Monte Carlo dose verification system for intensity modulated radiotherapy

Y.Ishihara<sup>1</sup>, Y. Narita<sup>1</sup>, T. Yamamoto<sup>1,2</sup>, T. Mizowaki<sup>1</sup>, Y. Miyabe<sup>1</sup>, A. Sawada<sup>1</sup>, S. Yano<sup>3</sup>, T. Teshima<sup>2</sup>, and M. Hiraoka<sup>1</sup>

<sup>1</sup> Department of Radiation Oncology and Image-applied Therapy,  
Graduate School of Medicine, Kyoto University, Kyoto 606-8507, Japan

<sup>2</sup>Department of Medical Physics & Engineering,  
Graduate School of Medicine, Osaka University, Osaka 565-0871, Japan

<sup>3</sup>Clinical Radiology Service, Kyoto University Hospital, Kyoto 606-8507, Japan

*e-mail: y.ishi@kuhp.kyoto-u.ac.jp*

## Abstract

We are developing a Monte Carlo (MC) based dose calculation system as a routine verification tool for four dimensional radiation therapy planning. It is of great importance of modeling multileaf collimator which induces leakage radiation, tongue-and-groove effect, beam hardening, and rounded leaf tip effect in intensity modulated radiation treatment (IMRT) field. The purpose of this study was to achieve accurate modeling inclusive of its dynamic motion behavior for the specific MLC (Millennium 120-leaf MLC, Varian) installed in our radiation treatment system.

First, we generated a geometrical MLC model based on its specification given by the manufacture. The implementation was performed employing the EGS4/PRESTA MC code. Subsequently, leakage, picket fence, sliding window, pyramid, and clinical tests with a water phantom were simulated for well-commissioned 6 MV and 15 MV photon beams, respectively. Then, the above simulated results were compared with the measured data with the same condition using a solid water phantom (Gammex RMI, Middleton, WI).

The simulated doses were normalized to the maximum dose in the clinical field for the clinical test while normalized to the open field of 10 x 30 cm for the other tests. The averaged differences between the simulated and the measured doses were 2.1 % (maximum 3.7 %) for the clinical test and 1.9 % for the other tests.

We have achieved an accurate modeling inclusive of its dynamic motion behavior for the specific MLC. From the results, it is concluded that our modeling has a reasonable accuracy, which may be expectedly useful for a verification tool for radiation therapy planning.

## 1. Introduction

Most of the commercial treatment planning systems don't take into account MLC design which causes the leakage radiation,<sup>1)</sup> the tongue-and-groove effect,<sup>2, 3)</sup> beam hardening<sup>4)</sup> and rounded leaf tip effect<sup>4)</sup> in intensity modulated radiotherapy (IMRT) field. It is generally accepted that Monte Carlo (MC) is the most accurate dose calculation method. The strength of MC comes from the fact that it can realistically model radiation transport and interaction processes through the accelerator head, beam modifiers and the patient geometry. The only one downside about MC algorithm is time consuming. There have been several fast MC codes developed, such as VMC/xVMC , VMC++, DPM and MCDOSE. These codes employ a variety of variance reduction techniques and achieve

reduced CPU time compared to ordinary EGS4 calculations. MC is becoming fast enough to be used in clinics (especially for treatment planning purposes) with the capability of accurate dose computations. We were to develop an integrated MC dose calculation system called MCRTV (Monte Carlo for Radiotherapy Treatment plan Verification) as a routine verification tool of radiotherapy.<sup>5)</sup> The MCRTV system was originally designed to provide the dose calculation benchmark results as accurately as possible, especially for IMRT plan QA. Therefore this system uses ordinary EGS4/PRESTA code. Recently, we developed the accurate model of the Varian Millennium 120-leaf MLC and appended it to the MCRTV system. The purpose of this study is to validate 120-leaf MLC model in various conditions.

## 2. Materials and Methods

The MC models of the Varian 120-leaf Millennium MLC was constructed using the EGS4/PRESTA MC code.<sup>6)</sup> Specific design of the MLC was accurately modeled in great detail considering the inter-leaf minute air gap, the tongue-and-groove design, the rounded leaf tip and the leaf alignment parallel to the beam divergence. The dynamic motion of the MLC leaves was simulated by sampling the leaf positions for each incident history using a cumulative probability distribution function of each leaf position, which can be created from a relationship between the fractional number of monitor units (MUs) and the corresponding leaf positions specified in the leaf sequence file. A similar method was employed by Liu H *et al.* for the DMLCQ component module in the EGS4/PRESTA code.<sup>7)</sup>

All the MC simulations in MCRTV ran on a Linux cluster (Hyper Blade, Appro International, Milpitas, CA, USA), consisting of 14 nodes (2 CPUs/node) of 3.2 GHz Intel Xeon processors. The MC codes have been parallelized using the message passing interface (MPI) for interprocessor communication. Although parallel computing is a meaningful way to reduce the computation time, its accuracy is critically influenced by the quality of adopted random number generator. We have implemented the scalable parallel random number generator (SPRNG) (<http://sprng.cs.fsu.edu/>) in our EGS4 MC codes. Tyagi N *et al.* also used SPRNG in order to parallelize the DPM codes and obtained excellent agreement between the results computed with serial and parallel code.<sup>8,9)</sup>

The EGS4 transport parameters were set to  $ECUT = AE = 0.521$  MeV for electrons and  $PCUT = AP = 0.010$  MeV for photons in all simulations. Default parameters were used for the PRESTA electron transport algorithm. Then, beam file was used with well-commissioned phase space data which was calculated for treatment head model of Varian Clinac 2300C/D for a 6 MV and 15 MV photon beams by EGS4 MC code.<sup>5)</sup> To precisely estimate the statistical uncertainty for the MC dose computation, the history-by-history method was employed instead of the ordinary batch approach.<sup>10)</sup> The relative statistical uncertainty for the MC simulations was less than 1.5 % in all tests.

The static tests for validation of the MLC model were implemented for investigation of leaf leakage and picket fence effects. These effects are strongly affected by geometry of the MLC model.

To examine how well the MLC model predicts dose undulations perpendicular to the direction of leaf motion for an MLC-blocked field due to leakage radiation, film measurements with above conditions (5 cm depth and 95 cm SSD) were made for  $10 \times 30 \text{ cm}^2$  field at 6 MV. At 15 MV, the film was placed at 10 cm depth and 90 cm SSD. Kodak EDR2 film with solid water phantom (Gammex RMI, Middleton, WI) were used for these measurements. The results of film measurements were compared with those of MC calculations under the same conditions, except voxel size of  $2.0 \times 0.1 \times 0.5 \text{ cm}^3$  for MC calculations. Doses are shown in percentage for open field of a  $10 \times 30 \text{ cm}^2$ .

To evaluate the effects of the leaf edges and tongue-and-groove geometry, we used the picket-fence patterns described by Siebers *et al.*<sup>11)</sup> The one-fence pattern was generated by closing the odd leaves and opening only the even leaves (or vice versa) and was used to validate particle tracking through the MLC leaf edges. The two-fence field was created by combining two alternating one-fence fields which resulted in the maximum tongue-and-groove effect. This field was used to validate the modeling of the leaf edges and transmission calculation. The spatial resolution was  $2.0 \times 0.1 \times 2.0 \text{ cm}^3$  in MC simulation. Film measurements were performed at the same condition as leakage test.

Sliding window, pyramid, and clinical tests were practiced as the dynamic tests. Sliding window tests evaluate the MLC leaf tip contribution to dose in dynamic MLC fields. Varying the window width, leaf tip transmission, and leaf tip leakage contributed to the total dose. The widths of the sliding windows were 1, 5, 10, 20, 50, 70 and 100 mm. Dose measurements were performed using the CC-04 ion chamber (Scanditronix Wellhöfer, Schwarzenbruck, Germany) with an active volume of  $0.04 \text{ cm}^3$  at a depth of 5 cm (95 cm SSD) for 6 MV, and at a depth of 10 cm (90 cm SSD) for 15 MV. The MC simulation used a voxel size of  $0.5 \times 2.0 \times 0.5 \text{ cm}^3$ . To verify the accuracy of the leaf sampling technique used for simulating the dose delivery of dynamic IMRT fields, intensity distributions was simulated using both pyramid pattern and clinical data of prostate case with IMRT. Film measurements were performed at the same condition as leakage test. A voxel size of  $0.3 \times 0.2 \times 0.3 \text{ cm}^3$  was used for MC simulations.

### 3. Results

The comparison of measured and calculated leakage profiles for the MLC blocked field are shown in Fig 1. Measurement results were averaged over a 2.0 cm wide band in the X direction centered on  $X = 0.0 \text{ cm}$  to match the resolution of the MC calculations in that dimension. MC calculations could reproduce dose patterns by measurements in terms of the frequency and amplitude for both 6 MV and 15 MV beams. Note that even the alternating peaks of high and low intensity (present due to the

alternating leaf MLC design) was correctly predicted. The dose difference between MC calculation and film measurement was less than 0.5%. In this study MLC leakage was 1.38% on average.

The measured and calculated picket fence profiles were compared as shown in Fig 2. Fig 2(a) shows profiles on the condition that even leaves are opened, and Fig 2(b) shows on the condition that odd leaves are opened. The averaged discrepancy between MC calculated and measured doses was 1.9%. From picket fence profiles, tongue-and-groove effect reduced dose by 8.3 % on average.

Table I summarizes results for the sliding window test. The narrower sliding window width increased dose discrepancy between MC calculations and measurements.

Fig 3 shows a comparison of measured and calculated profiles for a pyramid intensity pattern delivered with a dynamic technique. Measurement results were averaged over a 2.0 cm wide band in the X direction. The averaged discrepancy was 1.6 %. However, at a single point at -2 cm from the central axis in 6 MV the simulation predicted a 2.2 % lower dose than the measurements.

Fig 4 shows an example of comparison of dose profiles between film measurements and MC results for the dynamic IMRT fields in a prostate cancer patient with 6 MV and 15 MV. Dose profiles were determined for 6 bands along in-plane (X= -1.0 cm, 0.0 cm, and 1.0 cm) and cross-plane (Y= -1.0 cm, 0.0 cm, and 1.0 cm) directions. The results MC calculation and measurements agreed less than 2.1 % almost all regions of interest. The most different point between the MC calculation and measurement was 3.7 % in the position with steep dose distribution.

## 4. Discussion

MLC models have been developed by various reasons<sup>12, 13</sup>). In this study we reconstructed accurate MLC code for dealing with this model in MCRTV. Table II shows the result of dosimetric effects in this study with other reports. MLC leakage which was reported by other studies were 1.91% by Siebers J *et al.* , 1.58% by Jang Y *et al.* , and 1.50% by Heath E *et al.*<sup>11, 13, 14</sup>). In this study MLC leakage was 1.38% on average. Siebers J *et al.* and Jang Y *et al.* showed that the underdose due to the tongue - and - groove effect would amount to about 9.0%<sup>11, 14</sup>). From results in this study, tongue - and - groove effect reduced dose by 8.3% on average. These data are within a good agreement.

On the modern accelerators, the MLC system is a critical and integral component for the delivery and modulation. The commercial MLC have evolved to have very sophisticated designs. An approach to model the geometry of MLC, in which only photon attenuation and first Compton scattered photons were simulated through the MLC geometry, has been developed by Keall *et al.*<sup>12, 15</sup>), Siebers *et al.*<sup>11</sup>), and Fix *et al.*<sup>16, 17</sup>) for the Varian 80 - leaf MLC. The leaf edges parallel to leaf motion were modeled with the tongue - and - groove, but the rounded leaf tips were simplified and modeled as planes focused at the source in other reports<sup>11, 13, 14</sup>). Thus, although most investigators

tried to reduce CPU time with variance reduction techniques, we developed MCRTV to provide benchmark data of dose calculation as accurately as possible.

That is why the averaged discrepancy of MC and measured was less than about 2.2% in all tests. The process described here for validating the IMRT dose calculation is not unique to the MC system. Any treatment planning or dose calculation for IMRT should be subjected to a similar process to determine model parameters and confirm the validity of the dose distributions<sup>18,19</sup>. However, such modeling parameters may differ from system to system. This accurate model helps to minimize computational costs by better - optimized MC calculation parameters.

## 5. Conclusions

An EGS4MC dose calculation model of Varian 120-leaf Millennium MLC for dynamic IMRT was developed and validated its accuracy. MLC dosimetric effects were then successfully reproduced for both static and dynamic test patterns. This system will be used into the QA system for the routine verification of the commercial TPS for dynamic IMRT.

## Reference

1. Mohan R, Tong S, Arnfield S, *et al.*, The impact of fluctuations in intensity patterns on the number of monitor units and the quality and accuracy of intensity modulated radiotherapy, *Med. Phys.* **27**: 1226-1237, 2000
2. Deng J, Pawlicki T, Chen Y, *et al.*, The MLC tongue-and-groove effect on IMRT dose distributions, *Phys. Med. Biol.* **46**: 1039-1060, 2001
3. Hsu I, Pickett B, Shinohara K, *et al.*, Normal tissue dosimetric comparison between HDR prostate implant boost and conformal external beam radiotherapy boost: Potential dose escalation, *Int. J. Radiat. Oncol. Biol. Phys.* **46**: 851-858, 2000
4. Kim J, Siebers J, and Keall P, A Monte Carlo study of radiation transport through multileaf collimators, *Med. Phys.* **28**: 2497-2506, 2001
5. Yamamoto T, Mizowaki T, Miyabe Y, *et al.*, An integrated Monte Carlo dosimetric verification system for radiotherapy treatment planning. *Phys Med Biol*, **52**: 1-18, 2007
6. Bielajew A and Rogers D. PRESTA: The parameter reduced electron-step transport algorithm for electron Monte Carlo transport. *Nucl. Instrum. Methods B*, **18**: 165-181, 1997
7. Liu H, Verhaegen F and Dong L. A method of simulating dynamic multileaf collimators using Monte Carlotechniques for intensity - modulated radiation therapy. *Phys Med Biol*, **46**: 2283-2298, 2001
8. Tyagi N, Bose A and Chetty I. Implementation of the DPM Monte Carlo code on a parallel

- architecture for treatment planning applications. *Med Phys*, **31**: 2721–2725, 2004
9. Sempau J, Wilderman S and Bielajew A. DPM, a fast, accurate Monte Carlo code optimized for photon and electron radiotherapy treatment planning dose calculations. *Phys Med Biol*, **45**: 2263- 2291, 2000
  10. Walters B, Kawrakow I and Rogers D. History by history statistical estimators in the BEAM code system. *Med Phys*, **29**: 2745–2752, 2002
  11. Siebers J, Keall P, Kim J, *et al.* A method for photon beam Monte Carlo multileaf collimator particle transport. *Phys Med Biol*, **47**: 3225-3249, 2002 Walle J V, Martens C, Reynaert N, *et al.*, Monte Carlo model of the Elekta SLiplus accelerator: validation of a newMLC component module in BEAM for a 6 MV beam, *Phys. Med. Biol.* **48**: 371-385, 2003
  12. Walle J, Martens C, Reynaert N, *et al.*, Monte Carlo model of the Elekta SLiplus accelerator: validation of a newMLC component module in BEAM for a 6 MV beam, *Phys. Med. Biol.* **48**: 371-385, 2003
  13. Jang S, Vassiliev O, Liu H, *et al.*, Development and commissioning of a multileaf collimator model in Monte Carlo dose calculations for intensity-modulated radiation therapy, *Med. Phys.* **33**: 770-781, 2005
  14. Heath E and Seuntjens J, Development and validation of a BEAMnrc component module for accurate Monte Carlo modelling of the Varian dynamic Millennium multileaf collimator, *Phys. Med. Bio.* **48**: 4045-4063, 2003
  15. Keall P, Siebers J, Arnfield M, *et al.*, Monte Carlo dose calculations for dynamic IMRT treatments, *Phys. Med. Biol.* **46**: 929-941, 2001
  16. Fix M, Manser P, Born E, *et al.*, Monte Carlo simulation of a dynamic MLC based on a multiple source model, *Phys. Med. Biol.* **46**: 3241–3257, 2001
  17. Fix M, Manser P, Born E, *et al.*, Monte Carlo simulation of a dynamic MLC: implementation and applications *Z, Med. Phys.* **11**: 163–170, 2001
  18. Ma C, Li J, Pawlicki T, *et al.*, A Monte Carlo dose calculation tool for radiotherapy treatment planning, *Phys. Med. Biol.* **47**: 1671–1689, 2002
  19. Chetty I, Charland P, Tyagi N, *et al.*, Photon beam relative dose validation of the DPM Monte Carlo code in lung-equivalent media, *Med. Phys.* **30**: 563–573, 2003

Table I. Measured and computed point doses for sliding window test

Window Width (mm)	6MV		15MV	
	Measured (%)	MC (%)	Measured (%)	MC (%)
1	4.67	2.85	5.03	3.98
5	8.26	6.92	8.61	7.69
10	12.39	11.07	12.69	12.01
20	19.61	18.42	19.92	19.17
50	35.49	34.44	35.68	35.25
70	43.01	42.03	43.19	42.71
100	51.61	51.04	51.73	51.39

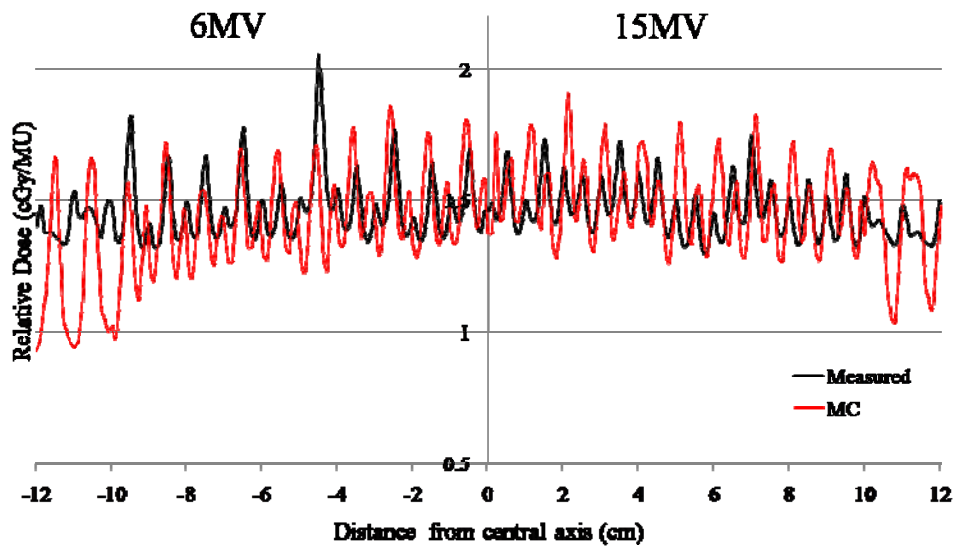


Fig 1. Measured and calculated MLC leakage radiation

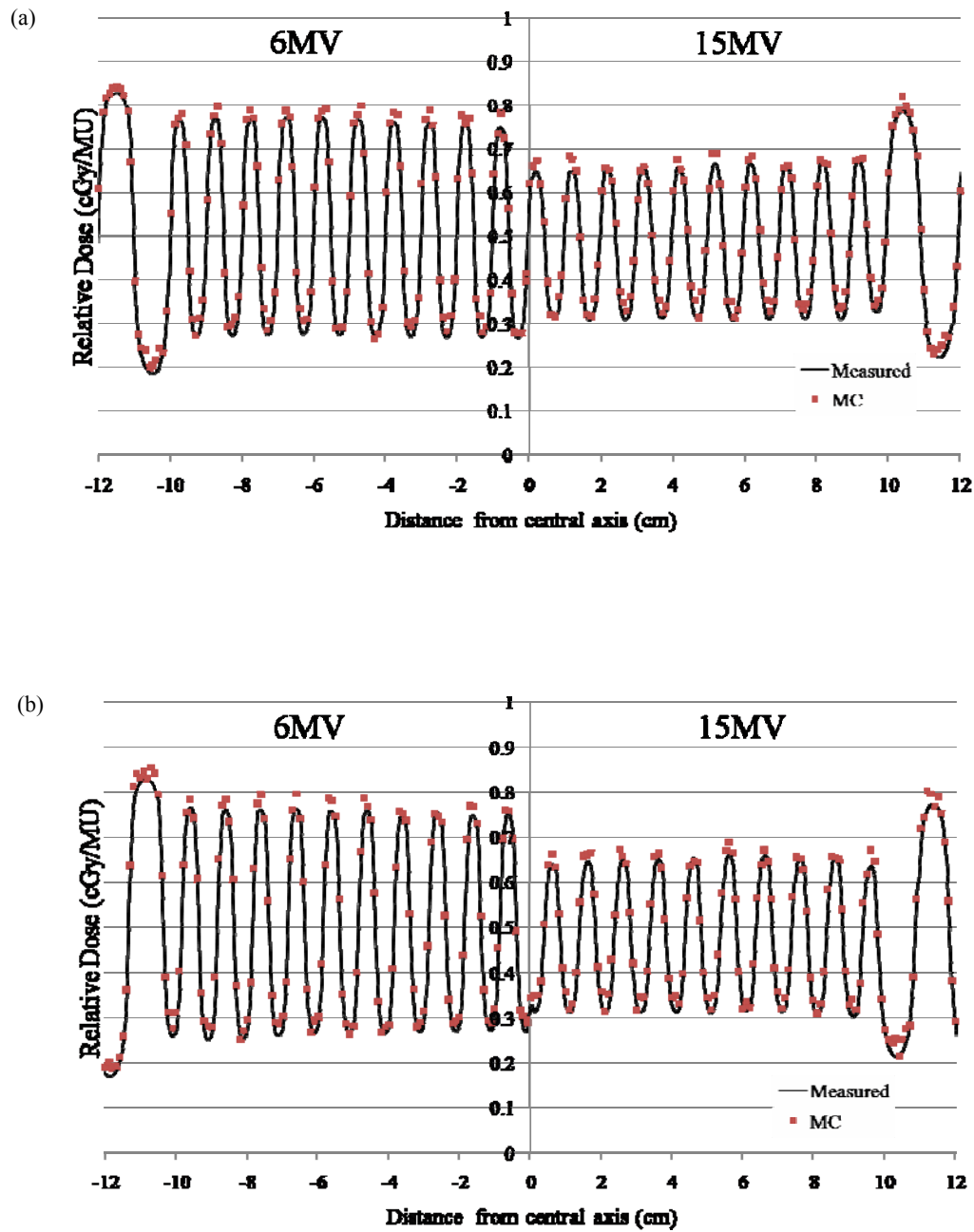


Fig 2. Measured and calculated dose blocked by odd leaves (a) and blocked by even leaves (b).

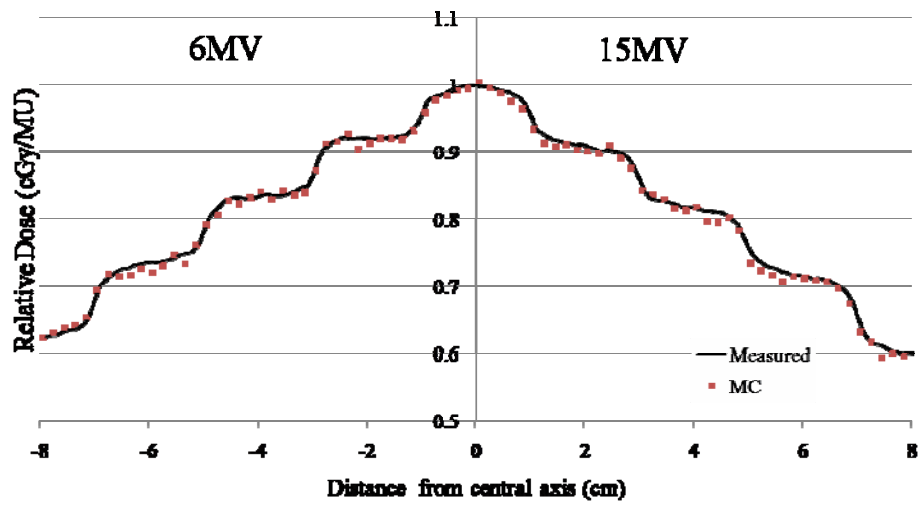
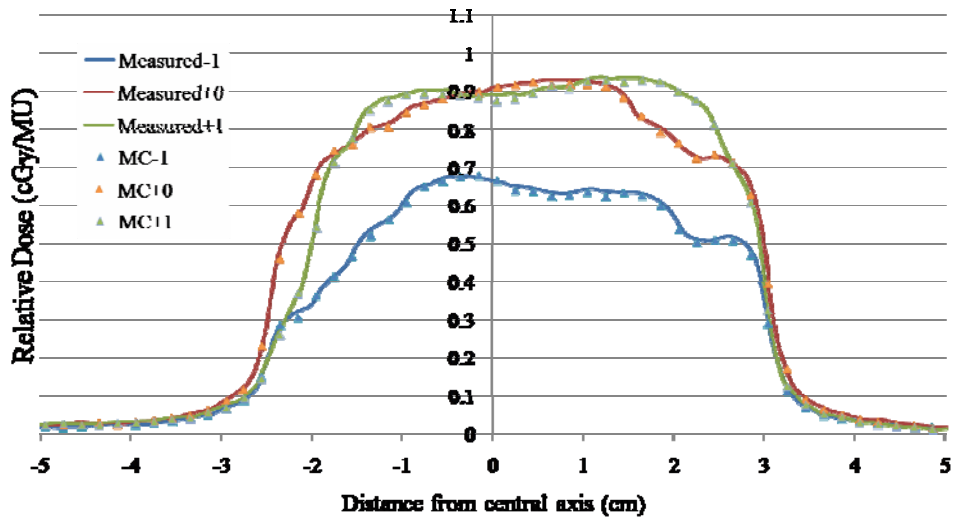
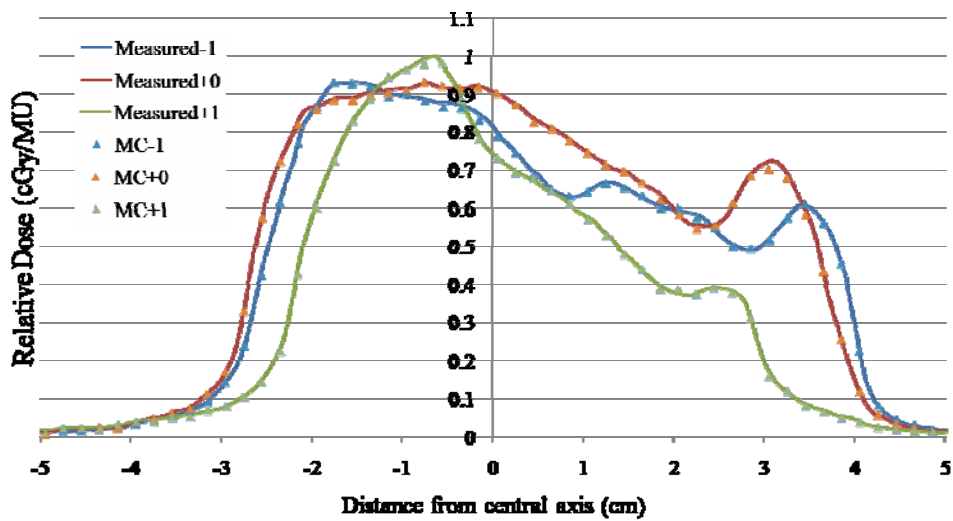


Fig 3. Measured and calculated profile for

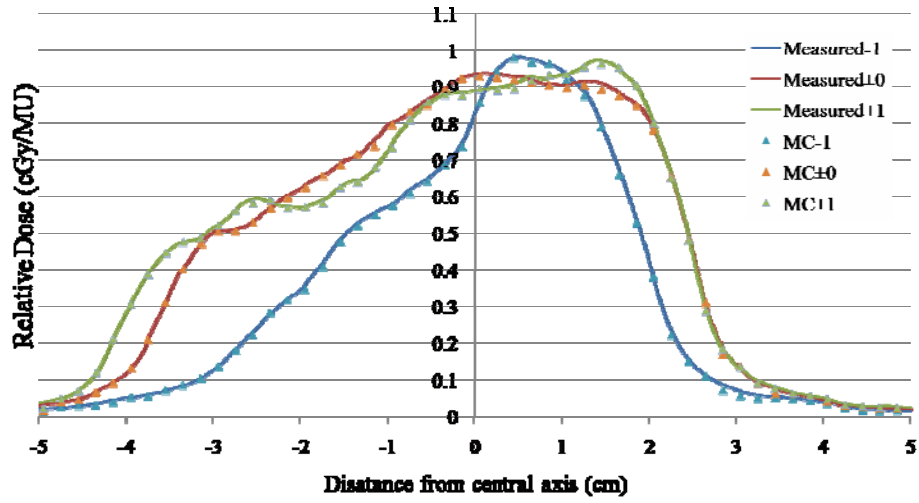
(a)



(b)



(c)



(d)

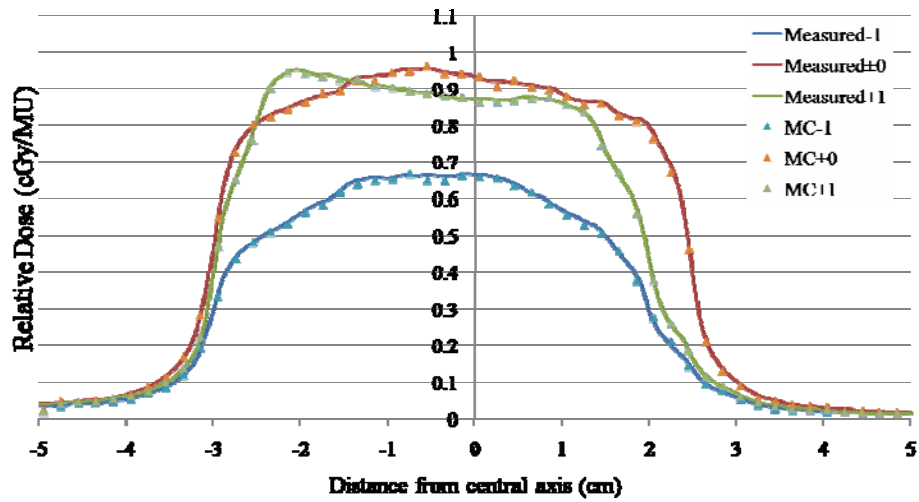


Fig 4. Measured and calculated profiles for 6MV cross-plane (a), 6MV in-plane (b), 15MV cross-plane (c), and 15MV in-plane (d).

Table II. Result of dosimetric effects in this study and other reports.

	This study	Heath E <i>et al.</i>	Siebers S <i>et al.</i> <sup>1</sup>	Jang Y <i>et al.</i>
Leakage (%)	1.38	1.50	1.91	1.58
Picket fence profile	<2.0	<2.0	<2.0	—
Dose difference (%)				
Sliding window test	<1.8	—	<1.5	<2.0
Pyramid test	<2.2	<4.0	—	—

# Investigation of uniform exposure to surface lesion using Ir-192 source

Keisuke Yasui<sup>1)</sup>, Yuuichi Aoyama<sup>2)</sup>, Tomohiro Shimozato<sup>3)</sup>,  
Ryota Kawanami<sup>1)</sup>, Kousaku Habara<sup>1)</sup>, Masataka Komori<sup>3)</sup>, Yasunori Obata<sup>3)</sup>

*<sup>1)Department of Radiological Technology, Graduate School of Medicine, Nagoya University</sup>*

*1-1-20 Daiko-Minami, Higashi-ku, Nagoya, Japan*

*<sup>2)Division of Radiology, Nagoya University Hospital</sup>*

*<sup>3)Nagoya University School of Health Science</sup>*

e-mail: [yasui.keisuke@a.mbox.nagoya-u.ac.jp](mailto:yasui.keisuke@a.mbox.nagoya-u.ac.jp)

## Abstract

Ir-192 sources have been widely used in clinical brachytherapy. For example, an intracavitary radiation therapy, an endovascular brachytherapy and a surface radiation therapy were performed using the Ir-192 sources. However, the appropriate step size, the catheter distance and reference points in the surface radiation therapy have not been investigated. The purpose of this study is to determine the appropriate treatment parameters, such as the step size, the catheter interval and the reference point for the uniform exposure to a surface lesion using the Ir-192 sources. To determine appropriate alignment of radiation sources, treatment planning systems (TPS) and Monte Carlo calculations were used. Active source dwell positions were investigated at intervals of 0.5 cm and 1.0 cm for each applicator and each step, and reference points were investigated at distance of 1.0 cm and 2.0 cm from the center of each source. The results of this study revealed that the step size and the catheter distance of 1.0 cm, and reference points placed at 1.0 cm distance from the center of each source are appropriate for the uniform exposure to the surface lesion.

## 1. Introduction

Ir-192 sources have been used in the conventional brachytherapy of tumors. An intracavitary radiation therapy, an endovascular brachytherapy and a surface radiation therapy [1-6] were performed using the Ir-192 sources, and conventional treatment planning systems (TPS) were used to create the plan. [1,5] The conventional TPS generally follows the AAPM TaskGroup-43 (TG-43) brachytherapy dose calculation formalism. This calculation bases on the application of the superposition principle to cylindrically symmetric dose distributions of single brachytherapy source that emits photon. The calculation algorithm by conventional brachytherapy TPS algorithm is fitted where the source shielding can be negligible, water can be estimated to be equivalent to the tissue over the photon energy range, high-Z or low density materials are not present and scatterings are similar to the single-source brachytherapy dose distributions obtained by either measurements or Monte Carlo methods. [7] TPS algorithm works well for the calculation of the single source dose distributions in water media. However, in clinical situations where the complex geometry or inhomogeneity regions are present, it is difficult to calculate accurately. Additionally, for the surface radiation therapy, the appropriate step size, the catheter interval and the reference points have not been investigated.

The purpose of this study is to investigate the appropriate geometry for uniform exposure to surface lesion using Ir-192 sources. Measurements by an ionization chamber and a radiochromic film were performed using the water phantom. Those measurements are provided for verifications of the relative dose distributions calculated using our Monte Carlo simulations. TPS was used to make the treatment plans for the uniform exposure to the surface lesion. Those plans were used to determine the dwell times at each source position, and Monte Carlo calculations were performed using these dwell times.

## **2. Materials and Methods**

### **2.1 Ir-192 source**

The brachytherapy source chosen for this study was a gamma-emitting isotope Ir-192 from the microSelectron HDR classic. The active core and the encapsulation geometry of the source is illustrated in Fig. 1 and as well as their compositional data is given in Table 1. [8]

### **2.2 Monte Carlo calculations**

Monte Carlo calculations were performed using Monte Carlo code (Electron Gamma Shower version 5; EGS) [9]. Photons with seven discrete energies ( 0.296, 0.308, 0.317, 0.468, 0.589, 0.604, and 0.612 MeV ) were isotropically emitted from the source core in the simulations. Emission rates of the energies were obtained from Ref. 10. The simulations were performed in water (size 10 x 10 x 10 cm<sup>3</sup>) and calculations geometry of relative dose were illustrated in Fig. 2 (a), (b). The tally grid was 0.1 x 0.1 x 0.1 cm<sup>3</sup>, and 2 x 10<sup>9</sup> photon histories were simulated. Typical statistical uncertainties were within  $\pm 3.0\%$ . The beta energy spectrum of Ir-192 has a mean value of about 0.2 MeV (with a maximum value of about 0.67 MeV) and the dose contribution of the beta particles emitted Ir-192 plays a role only near the source. Since it was reported that these effects can be ignored in the range over 0.2 cm [11], beta particles emitted Ir-192 were ignored in this study. Cut off energy of photon (PCUT) is 0.01 MeV and cut off energy of electron (ECUT) is 0.521 MeV (include rest energy).

### **2.3 Ionization chamber and radiochromic film measurements**

To obtain the relative dose of short axis, the ionization chamber (Semiflex Chamber type 31010, PTW Freiburg) and the electrometer (UNIDOS, PTW Freiburg) were used. It was selected due to its characteristics that its size was small and the chamber volume was 0.125 cm<sup>3</sup>. The dose measurements were performed in 0.01 cm increments for 0.43<d<0.5 cm, in 0.1 cm increments for 0.6<d<2.0 cm and at distance of 0.55, 2.5, and 3.0 cm from the source center. The sum of the catheter radius and the chamber radius is equal to 0.43 cm. Measured doses were normalized by the dose at 2.0 cm distance from the source center for the subsequent relative comparisons of the results from Monte Carlo methods and TPS.

The dose distributions were measured with radiochromic film (Gafchromic EBT film; EBT, ISP.Inc.) to provide a validation. Main characteristics of the EBT are the high spatial resolution, the slight energy dependence, the near tissue equivalence, the small dose uncertainty and the usability in water. [12-14] In this study, the EBT measurements were performed at 2.0 cm distance from the source center in water. The films were scanned using an ES-10000G flatbed scanner (EPSON. Co.) and read using film-analysis software (DD-system version 9.0.0.0, R-TECH.Inc.). Both measurements geometry were illustrated in Fig. 2 (a), (b).

### **2.4 TPS calculations for uniform exposure**

TPS calculations were performed using a commercial TPS (PLATO v14.3, Nucletron). Active source dwell positions were investigated at intervals of 0.5 cm and 1.0 cm in each applicator and each step. The dose distributions were normalized by the dose at the distance of 2.0 cm from the center of the central source. Reference points were placed at 1.0 cm or 2.0 cm distance from the center of each source. Target lesion of 2.0 x 2.0 cm<sup>2</sup> or 4.0 x 4.0 cm<sup>2</sup> was

irradiated by twenty five dwell positions (Fig. 3).

### 3. Results and discussions

#### 3.1 Validation of Monte Carlo calculations

To validate our results calculated by Monte Carlo method, the relative dose distributions were compared with measurement results of chamber or EBT and they are given in Figs. 4, and 5, and Tables 2 and 3. Fig. 4 shows the relative dose curve along the short axis of the source. The dose distribution is normalized at 2.0 cm distance from the source center. On average, the deviation between chamber and PLATO is 0.82 % and those between EGS and PLATO is 2.74 % (Table 1). Fig. 5 shows the relative dose profile along the long axis of the source. On average, the deviation between EBT and PLATO is 2.29 % and those between EGS and PLATO is 2.12 % (Table 2). These results show that the accuracies of dose distributions calculated using Monte Carlo in this study were confirmed.

#### 3.2 Investigation of uniform exposure to surface lesion

Figs. 6 (a) and (b) show the contour maps of the dose distribution when twenty-five Ir-192 sources are placed with 0.5 cm step size and catheter distance, and reference points are placed at distance of 1.0 cm from the center of each source (plan I). Figs. 7 (a) and (b) show the contour maps of the dose distribution when twenty five Ir-192 sources are placed with 1.0 cm step size and catheter distance, and reference points are placed at distance of 1.0 cm from the center of each source (plan II). Figs. 8 (a) and (b) show the contour maps of the dose distribution when twenty five Ir-192 sources are placed with 0.5 cm step size and catheter distance, and reference points are placed at distance of 2.0 cm from the center of each source (plan III). Figs. 9 (a) and (b) show the contour maps of the dose distribution when twenty five Ir-192 sources are placed with 1.0 cm step size and catheter distance, and reference points are placed at distance of 2.0 cm from the center of each source (plan IV). Table 4 shows the average doses of each reference point calculated by EGS and PLATO for each plan, and Table 5 shows the deviations between EGS simulation results and PLATO calculations for each plan. Table 6 shows the average dose and standard deviation (SD) of the target plane calculated by EGS.

From Table 4, it is observed that the average dose of each reference point calculated by each source position are almost same. However, from Figs. 6-9 and Table 6, it is observed that the dose distribution, the average dose and SD of target plane calculated by plan I and plan II are more uniform than those calculated by plan III and plan IV. In this study, since the plan with step size and catheter distance of 1.0 cm can irradiate uniformly in larger range than those of 0.5 cm, step size and catheter distance of 1.0 cm are appropriate for the uniform exposure to surface lesion.

### 4. Conclusions

The dose distributions for twenty-five Ir-192 sources with 0.5 cm or 1.0 cm step size and catheter distance, and with the reference points placed at distance of 1.0 cm or 2.0 cm from the center of each source were investigated in this study. The results show that the calculations using EGS show lower value than those using PLATO when the reference points are placed at 1.0 cm, while the results using EGS show higher value when the reference points are placed at 2.0 cm. The reason may be the typical statistical uncertainties of EGS and limitations of PLATO algorithm. The step size and catheter distance of 1.0 cm, and the reference points placed at 1.0 cm distance from the center of each source are appropriate for the uniform exposure to the surface lesion.

### References

- 1) C. Kirisits, B. POKRAJAC, D. Berger, E. Minar, R. Potter, D. Georg, "Treatment parameters for beta and gamma devices in peripheral endovascular brachytherapy," *Int. J. Radiation Oncology Biol Phys.* 60, 1652–1659, 2004
- 2) C. Sureka, C. Sunny, K. Subbaiah, P. Aruna, S. Ganesan "Dose distribution for endovascular brachytherapy using Ir-192 sources: comparison of Monte Carlo calculations with radiochromic film measurements," *Phys. Med. Biol.* 52, 525–537, 2007

- 3) H. Song, D. Eduardo, N. Yue, F. Errico, Z. Chen, R. Nath "Application of Gafchromic® film in the dosimetry of an intravascular brachytherapy source," Med. Phys. 33, 2519-2514, 2006
- 4) M. Imai, T. Nishimura, M. Nozue, et al "The 192Ir surface-mold technique for a whole scalp irradiation," J Jpn Soc Ther Radiol Oncol 11, 7-31,1999
- 5) R. Nakamura, S. Harada, T. Obara, S. Ehara, A. Yoshida, T. Akasaka, M. Shozushima, "Iridium-192 brachytherapy for hemorrhagic Angiosarcoma of the scalp: a case report," Jpn J Clin Oncol 33, 198-201, 2003
- 6) Hongquan Niu, W. Hsi, J.Chu, M. Kirk, "Dosimetric characteristics of the Leipzig surface applicators used in the high dose rate brachy radiotherapy," Med. Phys. 31, 3372-3374, 2004,
- 7) M. Rivard, C. Melhus, "An approach to using conventional brachytherapy software for clinical treatment planning of complex, Monte Carlo-based brachytherapy dose distributions," Med Phys 36, 1968-1975, 2009
- 8) M. Daskalov, E. Loffler, F. Williamson," Monte Carlo-aided dosimetry of a new high dose-rate brachytherapy source," Med Phys 25 .2200-2208, 1998
- 9) H. Hirayama, Y. Namito, A. Bielajew," The EGS5 code system SLAC-R-730," 2005
- 10) E. Browne, R. Firestone, "Table of radioactive isotopes," J. Wiley & Sons, New York, 1986
- 11) D. Baltas, P. Karaiskos, P. Papagiannis, L. Sakelliou, E. Loeffler, N. Zamboglou, "Beta versus gamma dosimetry close to Ir-192 brachytherapy sources," Med Phys 28, 1875-1882, 2001
- 12) Sou-Tung Chiu-Tsao,a\_ Yunsil Ho, Ravi Shankar,b\_ Lin Wang, and Louis B. Harrison, "Energy dependence of response of new high sensitivity radiochromic films for megavoltage and kilovoltage radiation energies," Med Phys 32, 3350-3354, 2005
- 13) S. Tsao, T. Duckworth, N. Patel, J Pisch, L. Harrison, "Verification of Ir-192 near source dosimetry using GAFCHROMIC film," Med Phys 31, 201-207, 2004
- 14) L. Menegotti, A. Delana, A. Martignano, "Radiochromic film dosimetry with flatbed scanners: A fast and accurate method for dose calibration and uniformity correction with single film exposure," Med Phys 35, 3078-3085, 2008

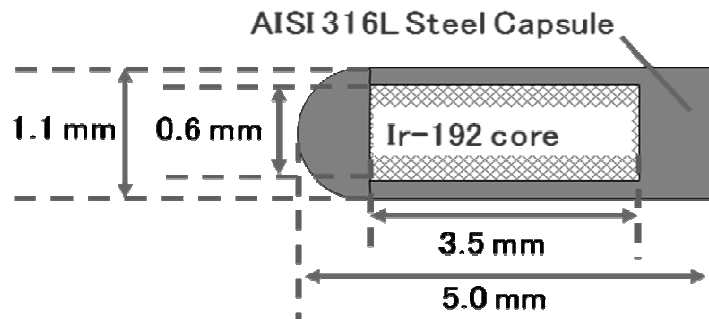
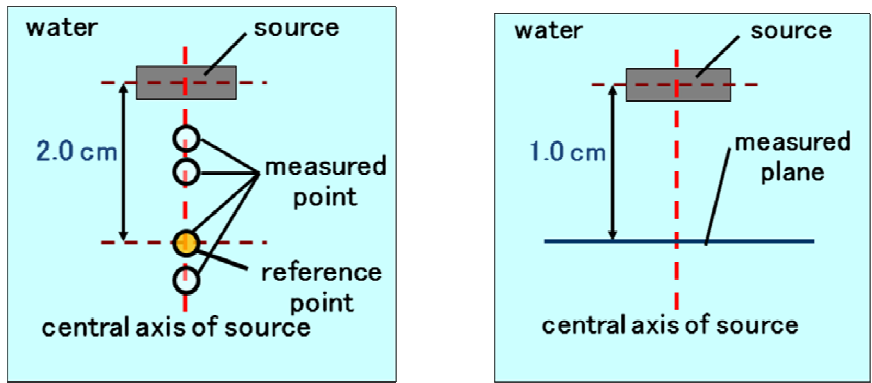


Fig. 1 The active core and encapsulation geometry of the source.

Table 1 Compositional data for the encapsulation of the sources.

elements	Fe	Cr	Ni	Mn	Si	Density
by weight	68 %	17 %	12 %	2 %	1 %	8.02 (g/cm <sup>3</sup> )



(a)

(b)

Fig. 2 The geometry to measure and calculate the relative dose.

(a) Geometry for the measurement by chamber. (b) Geometry for the measurement by EBT film.

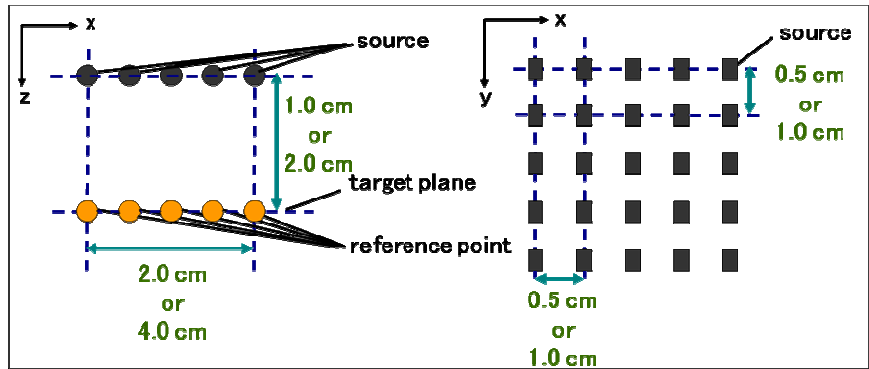


Fig. 3 Geometry of Ir-192 sources for the uniform exposure.

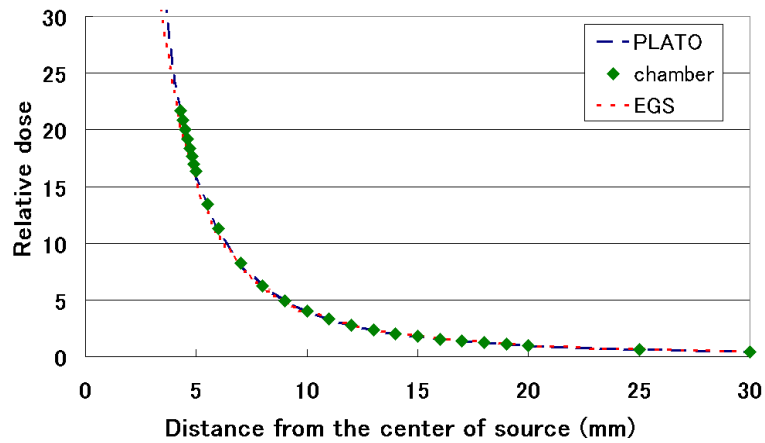


Fig. 4 Relative dose curves measured by chamber and calculated by EGS in comparison with PLATO calculation.

Table 2 The deviations between chamber and EGS, for PLATO (%)

	$(\text{chamber} - \text{PLATO}) / \text{PLATO} \times 100$	$(\text{EGS} - \text{PLATO}) / \text{PLATO} \times 100$
Average	0.82	2.74
Maximum	4.18 (0.5 cm distance)	5.70 (1.6 cm distance)

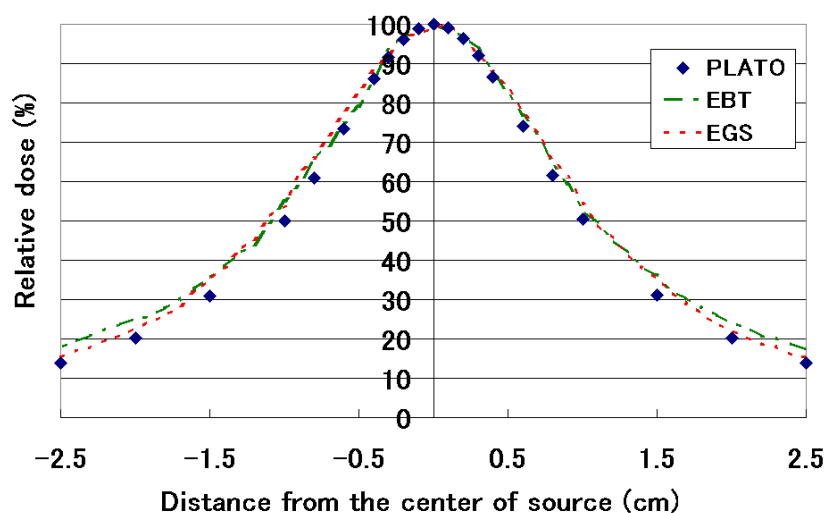


Fig. 5 Relative dose profiles measured by EBT and calculated by EGS in comparison with PLATO calculation.

Table.3 The deviations between EBT and EGS, for PLATO (%)

	EBT-PLATO	EGS-PLATO
High dose region (70%~) • Maximum	2.89	4.09
Low dose region (~30%) • Maximum	5.07	3.98
Average	2.29	2.12

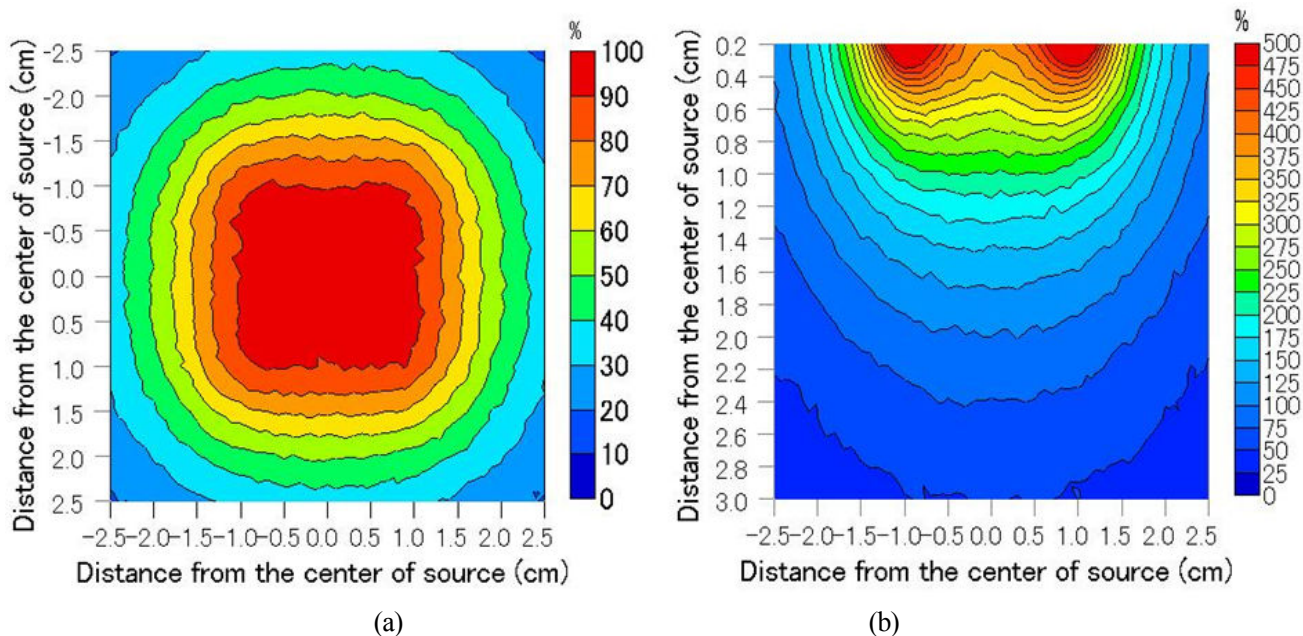


Fig. 6 The dose distributions when twenty-five Ir-192 sources are placed with 0.5 cm step size and catheter distance, and reference points are placed at 1.0 cm distance from the center of each source.

(a) X-Y plane at 1.0 cm (b) X-Z plane at Y=0.0 cm (plan I)

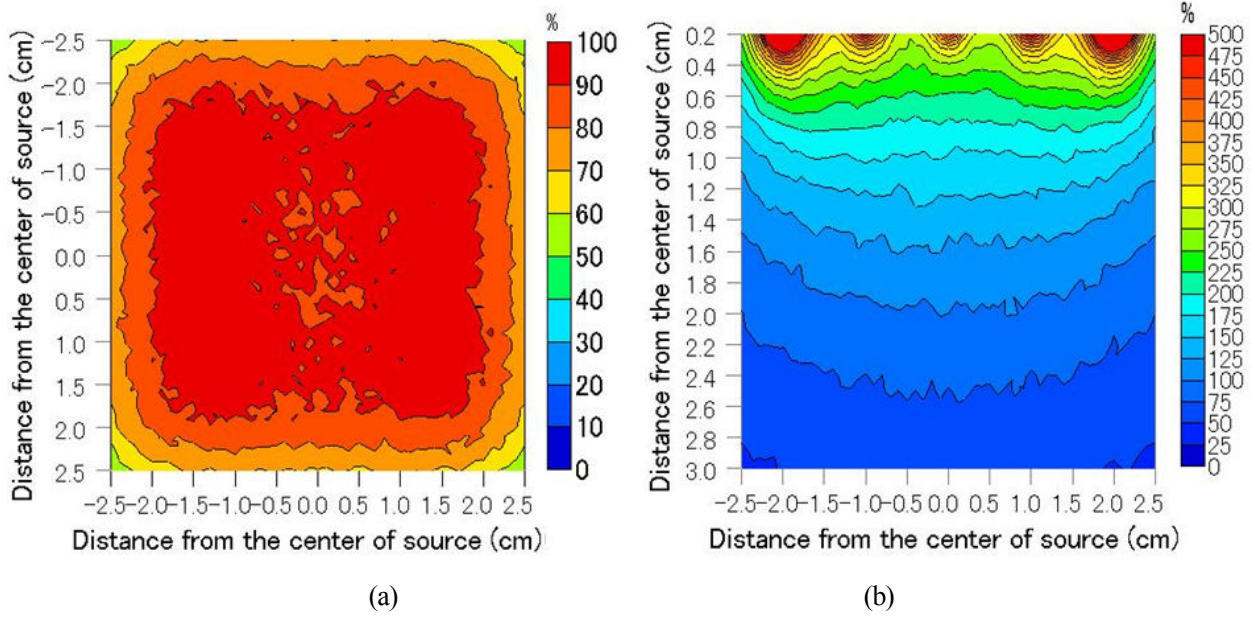


Fig. 7 The dose distributions when twenty-five Ir-192 sources are placed with 1.0 cm step size and catheter distance, and reference points are placed at 1.0 cm distance from the center of each source.

(a) X-Y plane at 1.0 cm (b) X-Z plane at Y=0.0 cm (plan II)

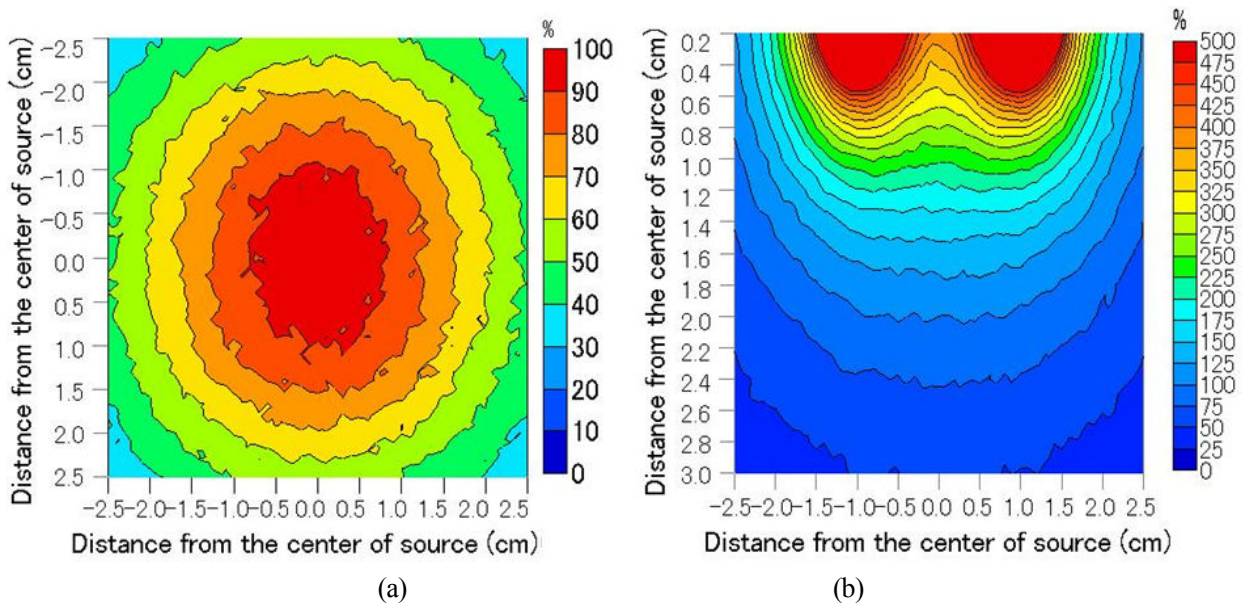


Fig. 8 The dose distributions when twenty-five Ir-192 sources are placed with 0.5 cm step size and catheter distance, and reference points are placed at 2.0 cm distance from the center of each source.

(a) X-Y plane at 2.0 cm (b) X-Z plane at Y=0.0 cm (plan III)

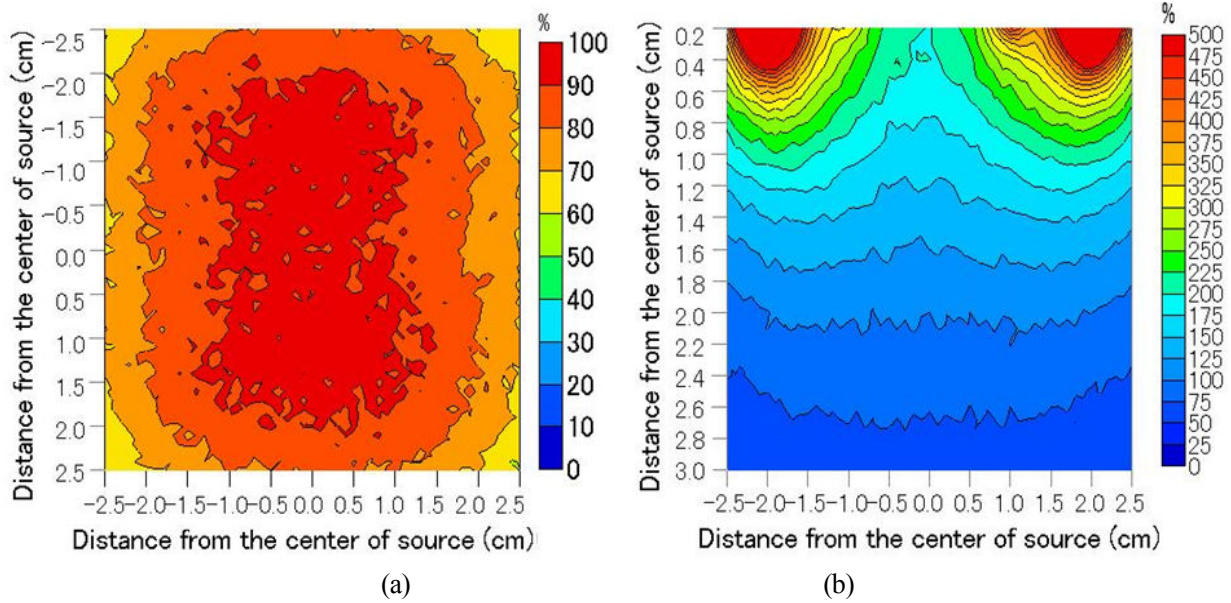


Fig. 9 The dose distributions when twenty-five Ir-192 sources are placed with 1.0 cm step size and catheter distance, and reference points are placed at 2.0 cm distance from the center of each source.

(a) X-Y plane at 2.0 cm (b) X-Z plane at Y=0.0 cm (planIV)

Table 4 The average dose of each reference point calculated by EGS and PLATO.

Average dose of each reference point (Gy)				
	plan I	plan II	plan III	plan IV
PLATO	1.99	2.00	1.98	1.96
EGS	1.98	2.00	2.05	2.00

Table 5 The deviations between results of EGS and PLATO calculations for each plan.

The deviations between results (%), (results of EGS – results of PLATO)				
	plan I	plan II	plan III	plan IV
Average	-0.61	-0.25	3.18	2.17

Table 6 The average dose and standard deviation (SD) of the target plane calculated by EGS

	plan I	plan II	plan III	plan IV
Average dose (Gy)	2.00	2.05	2.10	2.09
SD (%)	2.86	3.27	5.13	5.84

# COMPARING WITH THE CALCULATIONS OF PLATO CLINICAL TREATMENT PLANNING SYSTEM AND EGS5 SIMULATIONS FOR BRACHYTHERAPY

S. TSUJI and N. NARIHIRO<sup>†</sup>

*Kawasaki Medical School, Kurashiki 701-0192, Japan*

<sup>†</sup>*Kawasaki College of Allied Health Professions, Kurashiki 701-0194, Japan*

## Abstract

The microSelectron-HDR remote afterloading device has used for high dose-rate brachytherapy. We use the calculations of PLATO clinical treatment planning system for brachytherapy. Detailed Monte Carlo simulation EGS5 has also used in medical radiations. We compared the calculations of PLATO clinical treatment planning system and EGS5 simulations for brachytherapy. We found that the difference between the calculations of PLATO and EGS5 simulations is approximately less than 5%.

## 1 Introduction

Brachytherapy is a useful clinical treatment for a prostate cancer [1, 2]. We use the microSelectron-HDR remote afterloading device for brachytherapy. This treatment is used high-intensity <sup>192</sup>Ir sources. The sources capsuled in a stainless are embedded and irradiated the prostate. Generally, we calculate dose as a clinical treatment planning before an actual irradiation in a body. The calculated values are derived from PLATO clinical planning system. The calculation algorithm follows American Association of Physicists in Medicine Task group No.43 Report (AAPM TG-43) [3], and they are based on dose-rate distributions used for clinical implementation and dose-calculation methodologies. The EGS5 is the powerful simulation for electromagnetic interactions and can be applied in the field of radiology [4]. EGS5 simulations are thought to be comparable to the calculation of PLATO planning system. We compare EGS5 simulation and the calculation of PLATO planning system and report differences of them.

## 2 The calculation of PLATO planning system

The PLATO brachytherapy planning system calculate based on AAPM TG-43 [3]. The dose-rate equation is following,

$$\dot{D}(r, \theta) = S_k \cdot \Lambda \cdot \frac{G(r, \theta)}{G(r_0, \theta_0)} \cdot g(r) \cdot F(r, \theta), \quad (1)$$

where  $r$  denote the distance (in centimeters) from the center of the active source to the point of interest,  $r_0$  denotes the reference distance which is specified to be 1 cm in this protocol, and  $\theta$  denotes the polar angle specifying the point of interest,  $\theta_0$  denotes the reference angle which is specified to be 90° shown as Fig.1. The other parameter  $S_k$ ,  $\Lambda$ ,  $G(r, \theta)$ ,  $g(r)$  and  $F(r, \theta)$  represent the air-kerma strength, the dose rate constant, the geometry function, the radial dose function and the 2D anisotropy function respectively.  $S_k$  is calculated as the source intensity when the treatment starts.  $\Lambda$  is used the value 1.108 cGy/h/U in this planning system. The unit U is defined as the air-kerma strength, 1U=1cGy·cm<sup>2</sup>/h.

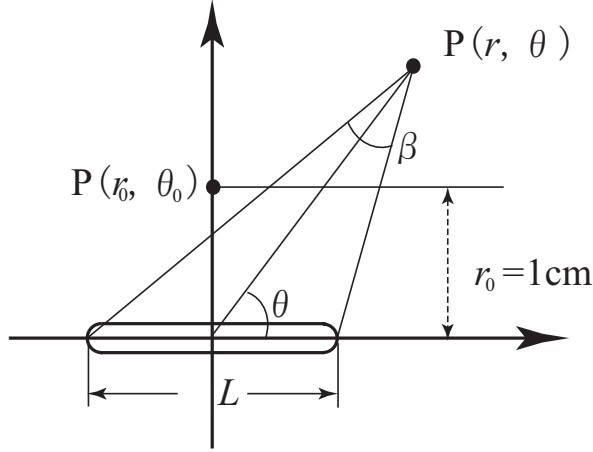


Figure 1: Coordinate system used for brachytherapy dose calculations.  $P(r, \theta)$  represents the interesting point.  $r_0$  and  $\theta_0$  mean 1 cm and  $90^\circ$  respectively.

## 2.1 Geometry function

The purpose of the geometry function is to improve the accuracy with which dose rate can be estimated by interpolation from data tabulated at discrete points. The protocol uses of point and line source models give the following functions,

$$G_P(r, \theta) = r^{-2} \quad \text{point source approximation,} \quad (2)$$

$$G_L(r, \theta) = \begin{cases} \frac{\beta}{Lr \sin \theta} & \text{if } \theta \neq 0^\circ \\ (r^2 - L^2/4)^{-1} & \text{if } \theta = 0^\circ \end{cases} \quad \text{line source approximation,} \quad (3)$$

where  $\beta$  is the angle as shown in Fig.1.

## 2.2 Radial dose function

The radial dose function,  $g_X(r)$ , accounts for dose fall-off on transverse-plane due to photon scattering and attenuation, and is defined by Eq.(4),

$$g_X(r) = \frac{\dot{D}(r, \theta_0) G_X(r_0, \theta_0)}{\dot{D}(r_0, \theta_0) G_X(r, \theta_0)}. \quad (4)$$

The subscript “X” represents whether a point source, “P”, or line source, “L” is used in transforming the data.

## 2.3 2D anisotropy function

The 2D anisotropy function,  $F(r, \theta)$ , is defined as

$$F(r, \theta) = \frac{\dot{D}(r, \theta) G_L(r, \theta_0)}{\dot{D}(r, \theta_0) G_L(r, \theta)}. \quad (5)$$

The Geometry function  $G_L$  is the formula in case of the line source.  $g_X(r)$  and  $F(r, \theta)$  are investigated by the experiment and the Monte Carlo simulations in each point or line sources. We use a high-intensity  $^{192}\text{Ir}$  source which is the Microelectron-HDR new design type. Each values of this radial dose function  $g(r)$  and the 2D anisotropy function  $F(r, \theta)$  are tabulated by G.M.Daskalov [5].

### 3 Results

For the EGS5 simulating, the following parameters are considered in various regions or mediums, sampling of angular distributions of photoelectrons, K and L edge fluorescent photons, K and L Auger electrons, Rayleigh scattering, linearly polarized photon scattering, incoherent scattering and Doppler broadening of Compton scattering energies. We continued the simulations until the cut off kinetic energy 1 KeV for one track. As other conditions, the emission rate of  $^{192}\text{Ir}$  is 2.072. We calculate the dose with the probability of radiations going out the stainless steel capsule.

#### 3.1 Comparing results of the experiment and the EGS5 simulations

Before comparing with the EGS5 simulation and the calculation of PLATO planning system, we need to check the EGS5 simulation compared with the measurements of source intensities. We used the  $^{192}\text{I}$  Microselectron-HDR new design type and measured in two positions, 8cm and 5cm, with  $\theta = 90^\circ (= \theta_0)$  as shown in Fig. 1. The ionization chamber type is PTW N3001 which has 0.6

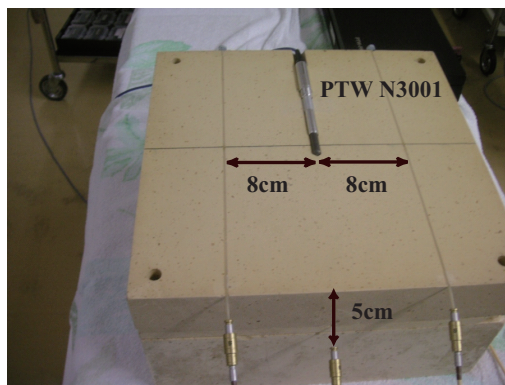


Figure 2: The picture shows the experiment in which the absorbed dose in the Mix-Dp phantom plate is measured. The ionization chamber is used PTW N3001. The distances are 5cm and 8cm.

$\text{cm}^3$  detectable volume. and using a medium is the Mix-Dp phantom. Used radiation of  $^{192}\text{Ir}$  has 288.18GBq. Fig. 2 shows the setting the source and the chambers in the experiment. The number of simulated showers is  $1.0 \times 10^8$ , the statistical error is less than 1% in 5cm, 2% in 8cm. The results of the experiment and the EGS5 simulation are tabulated in Table 1. For quantitative comparisons,

Table 1: The results of the experiment and the EGS5 simulation. Values need to apply  $\times 10^{-3}$  and the unit is Gy/sec.

distance	Experiment	EGS5
5 cm	$3.8975 \pm 0.0016$	$3.8138 \pm 0.0299$
8 cm	$1.4690 \pm 0.0024$	$1.4280 \pm 0.0174$

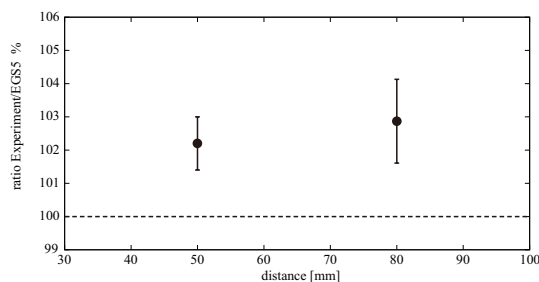


Figure 3: The ratios Experiment/EGS5. The ratios are shown by %.

we express the ratio, the experimental results divided by EGS5 results. Fig.3 represents the results. The ratios are  $1.220 \pm 0.0080$  in the distance 50 mm and  $1.0287 \pm 0.0126$  in the distance 80 mm. Both differences are about 2 ~ 3 %. The results of the experiment are larger than the simulations.

### 3.2 Comparing results of the calculation of PLATO planning system and the EGS5 simulations

We compare the results of the calculation of PLATO planning system and the EGS5 simulations from 10 mm to 100 mm for each 10 mm. In these calculations and simulations,  $\theta$  in Fig.1 is equal to  $90^\circ (= \theta_0)$ . Total showers used in the simulation are  $10^8$  events. Every statistical error is less than 1.5 %. Calculations and simulations use water as media. Fig.4 shows the absolute absorbed

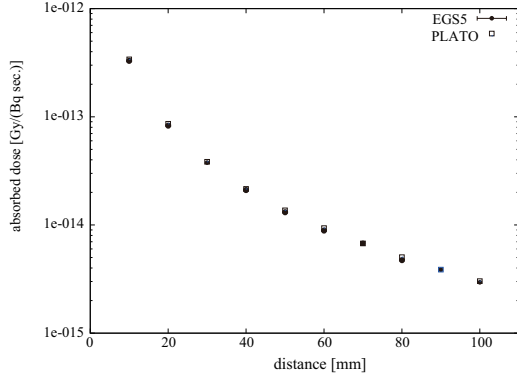


Figure 4: The results of absorbed dose in water. ●: EGS5 simulations. □: PLATO calculations.

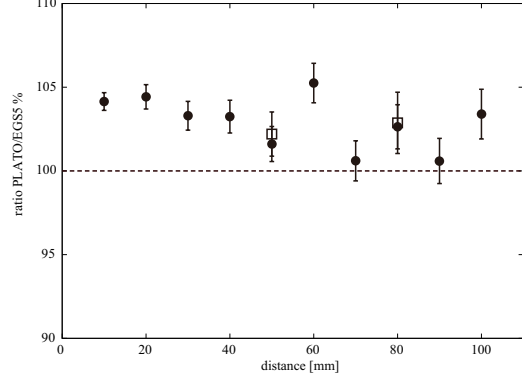


Figure 5: The ratios PLATO/EGS5. The ratios are added as predicted experimental results divided by EGS5. ●: PLATO/EGS5. □: Exp.(predict)/EGS5.

Table 2: The results of absorbed dose EGS5 simulations in water shown in Fig.4. The unit is Gy / ( Bq sec.).

distance(mm)	10	20	30	40	50
EGS5	$(3.260 \pm 0.017)$ $\times 10^{-13}$	$(8.251 \pm 0.058)$ $\times 10^{-14}$	$(3.716 \pm 0.031)$ $\times 10^{-14}$	$(2.084 \pm 0.020)$ $\times 10^{-14}$	$(1.343 \pm 0.014)$ $\times 10^{-14}$
distance(mm)	60	70	80	90	100
EGS5	$(8.884 \pm 0.100)$ $\times 10^{-15}$	$(6.708 \pm 0.080)$ $\times 10^{-15}$	$(4.909 \pm 0.063)$ $\times 10^{-15}$	$(3.845 \pm 0.052)$ $\times 10^{-15}$	$(2.926 \pm 0.042)$ $\times 10^{-15}$

Table 3: The ratios PLATO/EGS5 and Exp.(predict)/EGS5 shown in Fig.5.

distance(mm)	10	20	30	40	50
PLATO/EGS5	$1.041 \pm 0.005$	$1.044 \pm 0.007$	$1.033 \pm 0.009$	$1.032 \pm 0.010$	$1.016 \pm 0.010$
Exp.(predict)/EGS5					$1.022 \pm 0.013$
distance(mm)	60	70	80	90	100
PLATO/EGS5	$1.053 \pm 0.012$	$1.006 \pm 0.012$	$1.026 \pm 0.013$	$1.006 \pm 0.013$	$1.034 \pm 0.015$
Exp.(predict)/EGS5			$1.029 \pm 0.018$		

dose in the water for each distance. The difference in Fig.4 is almost negligible in the log scale. We also express the ratio, the calculation of PLATO divided by EGS simulations. Fig.5 shows the ratio as closed circles. Open squares are expected ratio from the mentioned experimental results. The difference are shown  $\approx 4\%$  near the point source ( $\approx 10$  mm) and  $\approx 2\%$  at the distance 50 mm.

The ratios more than 50 mm fluctuate for the statistical errors. The experimental results in the distance 50 mm and 80 mm are good agreement with the calculation of PLATO planning system. The EGS5 values in Fig.4 are tabulated in Table 2 and the ratios in Fig.5 are tabulated in Table 3.

## 4 Conclusion

We compare the EGS5 simulation and the calculation of PLATO planning system. First of all, we compare the EGS5 simulation and experimental results. We measured absorbed doses in the distances 50 mm and 80 mm. The experimental results are  $\approx 2\%$  larger than the EGS5 simulations. The differences of the EGS5 simulations and the calculation of PLATO planning system are less than  $\approx 5\%$  in the distance 10 mm to 100 mm. The experimental results in the distance 50 mm and 80 mm are good agreement with the calculation of PLATO planning system, because the AAPM TG-43 protocol used in the PLATO planning system is based on the experimental results. Nevertheless the EGS5 is not specialized in the field of radiology, the difference  $\approx 4\%$  between the EGS5 simulation and the calculation of PLATO planning system is small. We conclude that the EGS5 simulation is useful for the brachytherapy. We compare the EGS5 simulation and the calculation of PLATO planning system in the only special case along on the transverse-plane of the source ( $= \theta_0$ ). This means 2D anisotropy function  $F(r, \theta) = 1$ . Hence 2D anisotropy function  $F(r, \theta)$  dose not contribute the calculation of PLATO planning system in this time. The different results of the comparison may be led in another case  $\neq \theta_0$ .

## References

- [1] AT. Porter, JW. Scrimger, JS. Pocha, Int J Radiat Oncol Biol Phys. **14** 3, 571(1988).
- [2] D. Miszczak, "Proceedings of the XLII Zakopane School of Physics, Zakopane 2008", ACTA PHYSICA POLONICA A **115**, 583(2009).
- [3] M. J. Rivard et.al., Med. Phys.**31** 3,633(2004).
- [4] T. Oshima et al., Phys. Med. Biol. **54** 3491(2009).
- [5] G. M. Daskalov, E. Löffler, J. F. Williamson, Med. Phys. **25** 11, 2200(1998).

# MONTE CARLO CHARACTERIZATION OF THE PHOTON SOURCE FROM A CLINICAL LINEAR ACCELERATOR

**N. Mukumto and T. Teshima**

*Department of Medical Physics & Engineering,  
Osaka University Graduate School of Medicine, Osaka 565-0871, Japan  
e-mail: mukumoto@sahs.med.osaka-u.ac.jp*

## **Abstract**

Monte Carlo (MC) method provides the most accurate dose distributions. A drawback of the method is the long computing time needed to commission dose calculations of acceptable accuracy. Physical characteristics of the photon source from a clinical linear accelerator were important for MC commissioning. In this study we simulated a 6 MV photon beam from Varian Clinac and analyzed their characteristics, such as planar fluence, energy fluence, angular distribution, and energy spectrum. Phase space data (PSD) was scored for the field size 40 cm  $\times$  40 cm at source surface distance (SSD) of 100 cm. Due to the geometry of the flattening filter, planar fluence were increased with the off axis distance increased. Energy fluence was plateau due to the change of mean energy. Energy spectra based on the locations of the last interaction, such as target, primary collimator, and flattening filter, were different from each particle position at the isocenter. We investigated that physical characteristics of the photon source from a clinical linear accelerator was significantly different from each particle position at the isocenter.

## **1. Introduction**

High precision radiotherapy needs complex beam delivery. Dose calculation is one of the most important factors for quality assurance (QA) and quality control (QC) in radiotherapy. Accurate dose calculation algorithms are essential. In commercial treatment planning systems (TPS), comparatively accurate dose calculation algorithms, such as convolution/superposition method [1-3], have been used. However, the conventional dose calculation algorithms often fail to predict accurate dose distributions, mainly due to the inhomogeneities in the patient anatomy, such as lung and bone [4-6]. For example, widespread conventional algorithms in the commercial TPSs cause systematic error that exceeds 10% in the thoracic area [7]. The accuracy required for dose computation is generally within 2% [8-10], however, large errors in the doses calculated by conventional dose algorithms exceeding that criteria were reported [8]. These uncertainties in dose distributions may cause the unintended overdose or underdose to the target or the surrounding normal tissues and influence clinical outcome.

Currently, Monte Carlo (MC) is the most accurate dose calculation algorithm, since it can precisely calculate realistic radiation transport through the treatment head of the clinical linear accelerator and the in the patient anatomy. There are several possible approaches to generate an accurate source model to achieve the accurate dose calculations. One approach to generate a source model is to characterize the beam analytically [11,12]. The parameters of the beam model are approximately determined from the measured data of the dose distribution in a homogeneous phantom. Hence, this source model has risk to model physically unreal conditions [12]. The other approach is to perform full MC simulations of the radiation transport through the accelerator head and to generate phase-space data (PSD) that contains

the necessary data (position, direction, and energy) for each particle traversing the phase-space (PS) scoring plane perpendicular to the beam axis and above the irradiated body. This PSD provides accurate particle distributions in the PS plane, thus, PSD can be used directly as source models [13-16]. A drawback of the method is the long computing time needed to commission dose calculations of acceptable accuracy. Physical characteristics of the photon source from a clinical linear accelerator are important for MC commissioning.

In this study, we simulated a 6 MV photon beam from Varian Clinac and analyzed their characteristics, such as planar fluence, energy fluence, angular distribution, and energy spectrum.

## 2. Materials and Methods

### 2.1 MC simulation

We have developed the MC models of the treatment head of the Varian Clinac 23EX (Varian Medical Systems, Palo Alto, CA) linear accelerator for a 6 MV photon beam. Figure 1 shows schematic drawings of the Varian Clinac. The EGS5 MC code [17] was used in this study. The modeled linac head components were as follows: target/backing, primary collimator, vacuum window, flattening filter and jaws on the X and Y coordinates. The jaws were set to produce  $40 \times 40 \text{ cm}^2$  open field at source surface distance (SSD) of 100 cm. The monitor ion chamber and field mirror were omitted from modeling since they were present only a small attenuation to the photon beam. [12] The mean electron beam energy incident on the target and the FWHM of the radial intensity distribution were set to 5.95 MeV and 0.8 mm, respectively. The FWHM of energy distribution was consistently 3% of the mean energy. The distributions of the energy and intensity were assumed Gaussian in shape. Figure 2 shows Gaussian distribution calculated for the simulation. In the MC simulation, a total of  $1.0 \times 10^9$  electron histories was simulated. The energy cut-offs for particle transport were set to  $AE = E_{\text{CUT}} = 0.700 \text{ MeV}$  and  $AP = PCUT = 0.010 \text{ MeV}$ . The PSD file contained approximately a total of  $3.5 \times 10^7$  photon which correspond to 1.0 GB file size.

### 2.2 PSD Analysis

A Analysis application was developed in C++ Builder (Borland Software Corp., Scotts Valley, CA) and runs under the Windows XP (Microsoft, Inc., Redmond, WA) operating system. To analyze the PSD related to the locations of the last interaction, *zlast* and *LATCH* variables were introduced to the EGS5 code. Each physical characteristics, such as planar fluence, energy fluence, angular distribution, and energy spectrum were analyzed with respect to each *LATCH*. Planar fluence was calculated by counting the particle of the PSD with respect to each off-axis distance. Energy fluence was also calculated by considering the each particle energy. Angular distribution was calculated by reconstructing the radiation angle between the position of last interaction and isocenter plane. Energy spectrum was calculated by counting the particle of the PSD with respect to each energy.

## 3. Results and discussion

Figure 3 shows the distribution of the origin sites of photons for a Varian 6 MV photon beam. Particle interacted with the treatment head components. Figure 4 shows the planar fluence (a), energy fluence (b) and angular distribution (c) with respect to each treatment head components. Due to the geometry of the flattening filter, planar fluence were increased with the off axis distance increased. Energy fluence was plateau due to the change of mean energy. Angular distribution was increased with distance from the central axis and rapidly decreased due to the geometry of the flattening filter and the primary collimator. Flattening filter decreased the fluence of the central axis due to the thick material. Primary

collimator eliminated the particle that was unnecessary because of their large radiation angle. Figure 4 shows energy spectra based on the locations of the last interaction, such as target, primary collimator, and flattening filter, were different from each particle position at the isocenter. Energy spectrum at the region of the field edge was hardened compared to that at the central axis due to the flattening filter.

## 4. Conclusions

We developed the PSD analysis application and investigated that physical characteristics of the photon source from a clinical linear accelerator was significantly different from each particle position at the isocenter. This information will be helpful for MC commissioning.

## References

- 1) M. M. Aspradakis, R. H. Morrison, N. D. Richmond, *et al.*, Experimental verification of convolution/superposition photon dose calculations for radiotherapy treatment planning, *Phys. Med. Biol.* **48**: 2873–2893, 2003.
- 2) G. Starkschall, R. E. Steadham, R. A. Popple, *et al.*, Beam-commissioning methodology for a three dimensional convolution/superposition photon dose algorithm, *J. Appl. Clin. Med. Phys.* **1**: 8–27, 2000.
- 3) H. H. Liu, T. R. Mackie, and E. C. McCullough, Calculating dose and output factors for wedged photon radiotherapy fields using a convolution/superposition method, *Med. Phys.* **24**: 1714–1728, 1997.
- 4) J. J. DeMarco, T. D. Solberg, and J. B. Smathers, A CT-based Monte Carlo simulation tool for dosimetry planning and analysis, *Med. Phys.* **25**: 1-11, 1998.
- 5) C. M. Ma, E. Mok, A. Kapur, *et al.*, Clinical implementation of a Monte Carlo treatment planning system, *Med. Phys.* **26**: 2133-2143, 1999.
- 6) P. Carrasco, N. Jorret, M. A. Duch, *et al.*, Comparison of dose calculation algorithms in phantoms with lung equivalent heterogeneities under conditions of lateral electronic disequilibrium, *Med. Phys.* **31**: 2899-2911, 2004.
- 7) F. C. P. Plessis, C. A. Willemse, M. G. Lötter, *et al.*, Comparison of the Batho, ETAR and Monte Carlo dose calculation methods in CT based patient models, *Med. Phys.* **28**: 582–589, 2001.
- 8) AAPM TG-65, Tissue inhomogeneity corrections for megavoltage photon beams, *AAPM Report No. 85 (Madison, WI, USA: Medical Physics Publishing)* p9, 2004.
- 9) ICRU, Determination of absorbed dose in a patient by beams of X or gamma rays in 485 radiotherapy procedures, *ICRU Report 24 (Bethesda, MD, USA: ICRU)*, 1976.
- 10) ICRU, Use of computers in external beam radiotherapy procedures with high-energy photons and electrons, *ICRU Report 42 (Bethesda, MD, USA: ICRU)*, 1987.
- 11) S. B. Jiang, A. L. Boyer, and C. M. Ma, Modeling the extrafocal radiation and monitor chamber backscatter for photon beam dose calculation, *Med. Phys.* **28**: 55–66, 2001.
- 12) M. Fippel, F. Haryanto, O. Dohm, *et al.*, A virtual photon energy fluence model for Monte Carlo dose calculation, *Med. Phys.* **30**, 301–311, 2003.
- 13) D. M. Lovelock, C. S. Chui, and R. Mohan, A Monte Carlo model of photon beams used in radiation therapy, *Med. Phys.* **22**, 1387–1394, 1995.
- 14) D. W. O. Rogers, B. A. Faddegon, G. X. Ding, *et al.*, BEAM: a Monte Carlo code to simulate radiotherapy treatment units, *Med. Phys.* **22**, 503–524, 1995.
- 15) G. X. Ding, Energy spectra, angular spread, fluence profiles and dose distributions of 6 and 18 MV photon beams: results of Monte Carlo simulations for a Varian 2100EX accelerator, *Phys. Med. Biol.* **47**: 1025-1046, 2002.
- 16) D. S. Bagheri and D. W. O. Rogers, Monte Carlo calculation of nine megavoltage photon beam spectra using the BEAM code, *Med. Phys.* **29**, 391–402, 2002.
- 17) H. Hirayama, Y. Namito, A. F. Bielajew, *et al.*, The EGS5 Code System. *SLAC-R-730*, 2005.

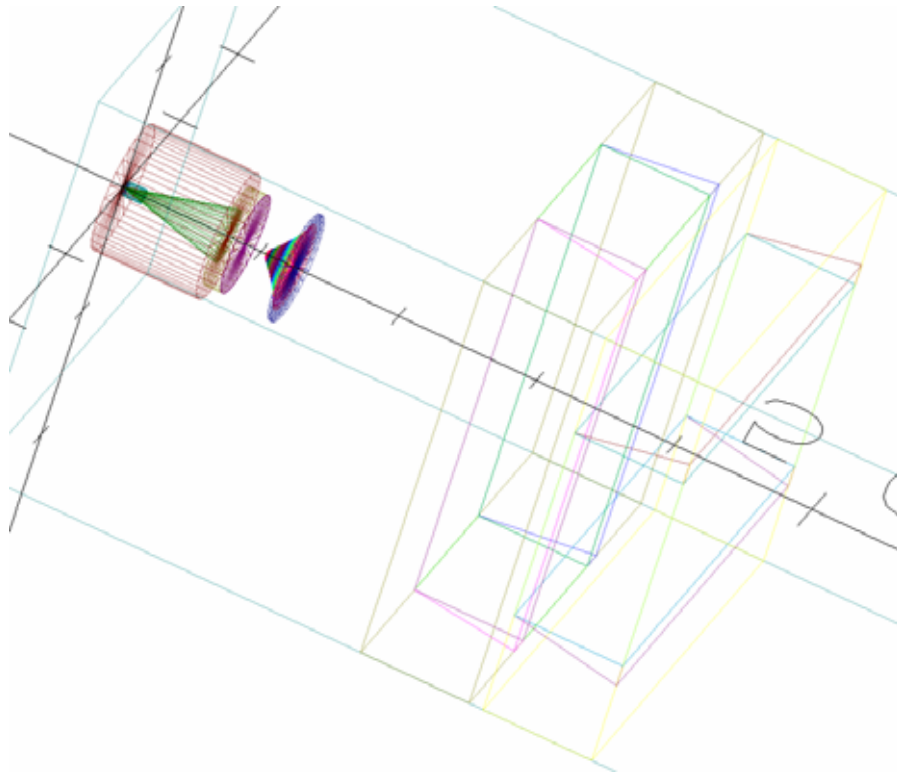


**Figure 1.** Schematic drawings of Varian Clinac 23EX.

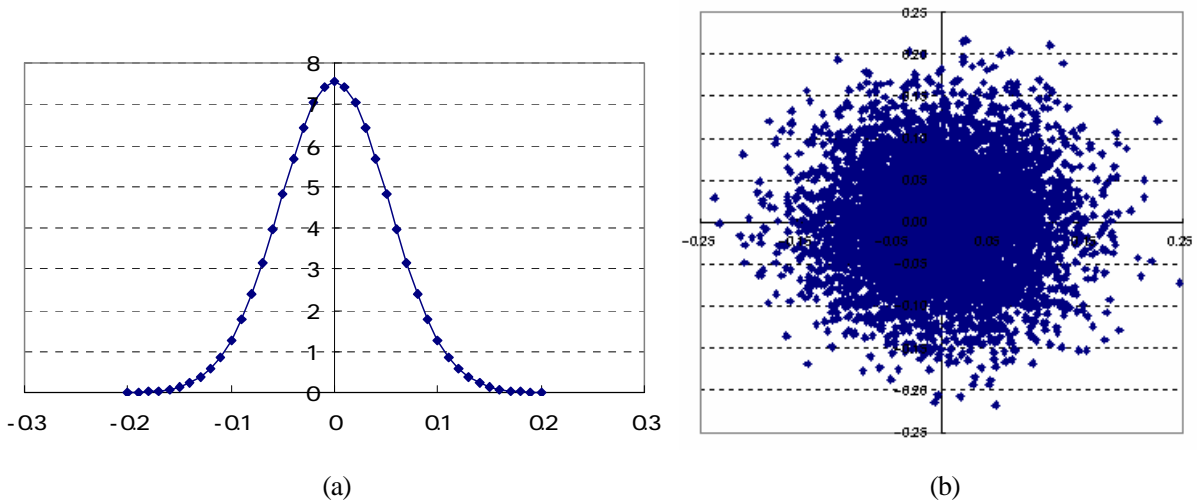


**Figure 2.** Gaussian distribution (a) and sampled intensity distribution (b).

+

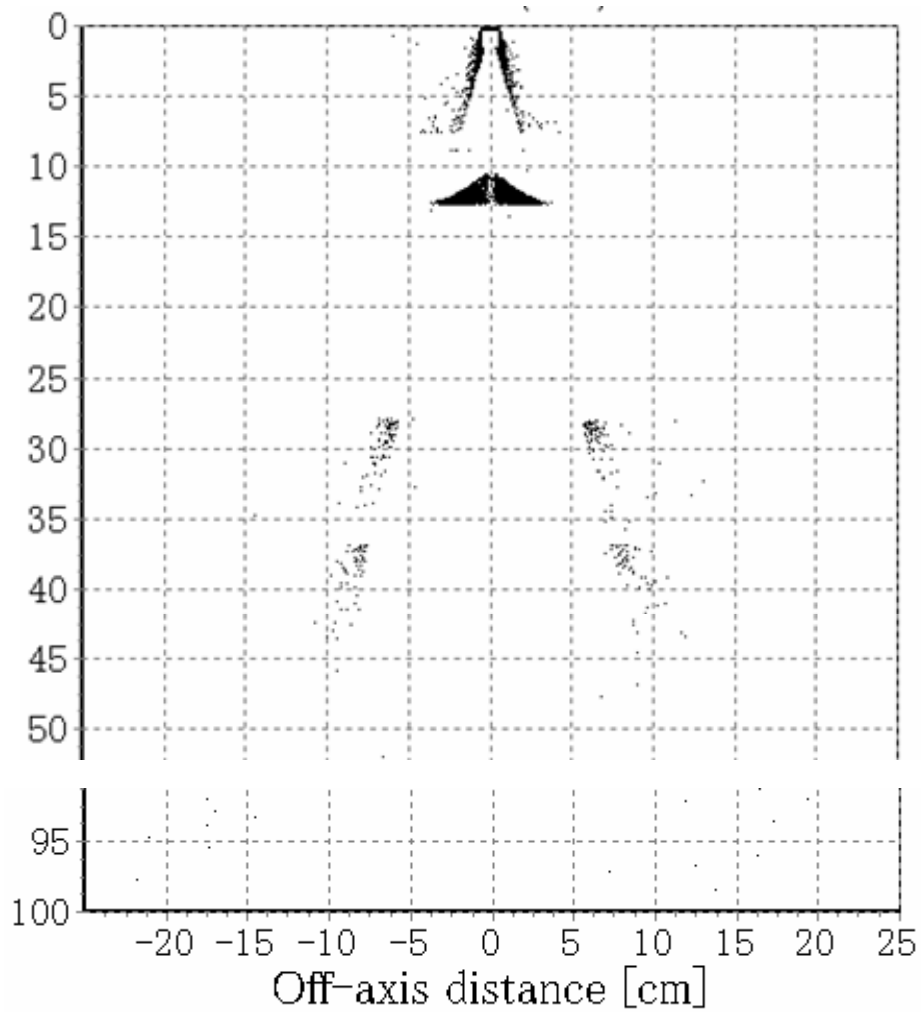


**Figure 3.** Distribution of the origin sites of photons for a Varian 6 MV photon beam.

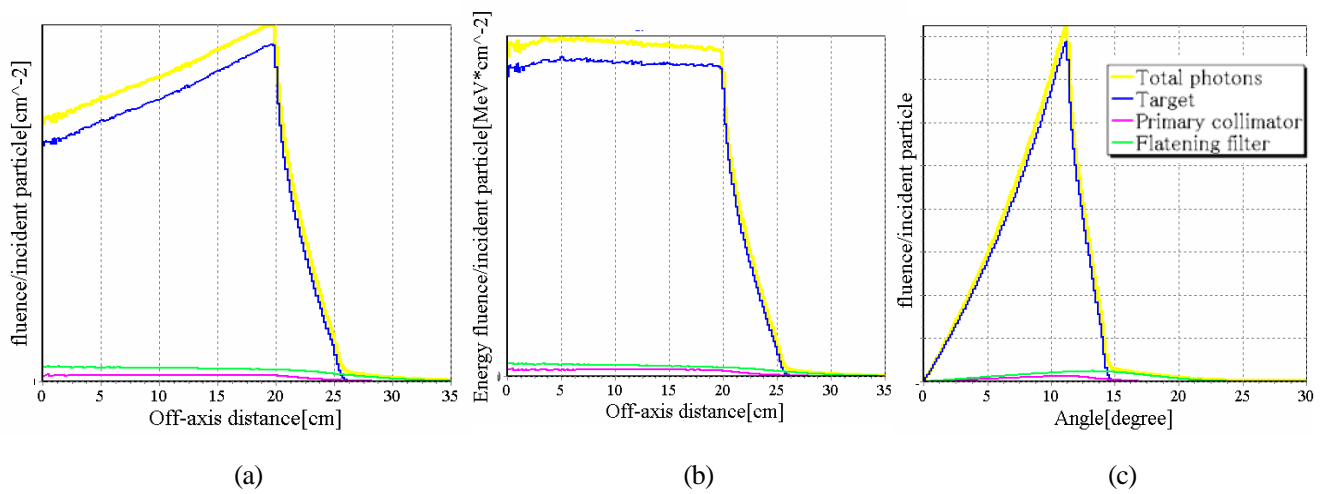
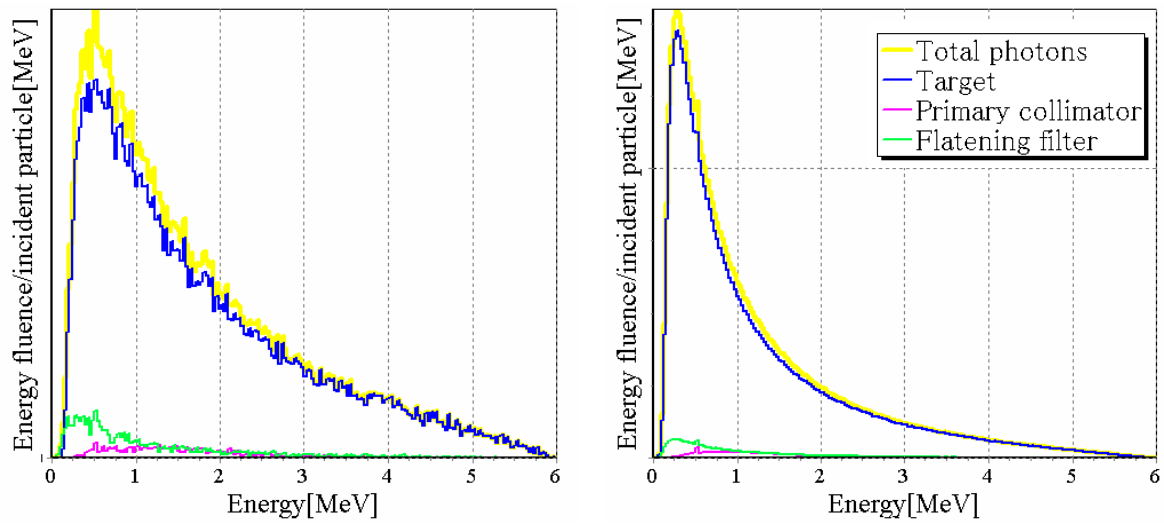


**Figure 4.** Planar fluence (a), energy fluence (b) and angular distribution (c).



(a) (b)  
**Figure 5.** Energy spectra at the central axis (a) and the field edge (b).

# Effect of the beam shaping filter in the X-ray CT simulation

Y. Morishita<sup>1</sup>, S. Koyama<sup>2</sup>

*<sup>1</sup>Department of Radiological Technology, Graduate School of Medicine, Nagoya University*

*1-1-20 Daikou-Minami, Higashi-ku, Nagoya, Japan*

*<sup>2</sup>Nagoya University School of Health Sciences*

*e-mail: morishita.yuki@e.mbox.nagoya-u.ac.jp*

## Abstract

There is specific beam molding filter called beam-shaping filter or Bow-tie filter in front of an X-ray tube of X-ray CT device. The beam-shaping filter equalizes radiation quality after X-rays penetrated an object. The geometry and composition of the filter is secret in each manufacturer and is complex. Therefore, it is difficult to build in mathematical model of the actual beam shaping filter in the simulation code. In this study, we incorporated data sets of dose distribution and energy change in an X-ray fan beam based on measurement into the EGS5 simulation code. In this measurement, a semiconductor dosimeter called rapidose was used. Evaluation of calculated result was performed by comparing computed tomography dose index (CTDI) of the calculation and the measurement. The simulation value was higher around 2 times than measurement value when the dose distribution in the X-ray fan beam was not considered. The measurement value and the simulation value were comparatively close when the dose distribution was considered.

## 1.Introduction

There is specific beam molding filter called beam - shaping filter or Bow-tie filter in front of an X-ray tube of X-ray CT device. The beam-shaping filter equalizes radiation quality after X-rays penetrated an object. This filter is essential to make an accurate computation in X-ray CT Monte Carlo simulation. The geometry and composition of the filter is secret in each manufacturer and is complex. Therefore, it is difficult to build in mathematical model of the actual beam shaping filter in the simulation. In general, the geometry of the beam-shaping filter is thin in the center and is thickened with increasing distance from the center. We attempted to simulate using measured value of X-rays after transmitted the filter instead of modeling the actual filter.

Evaluation of calculated result was performed by comparing computed tomography dose index (CTDI) of the calculation and the measurement.

## 2.Materials and Methods

### 2.1 Consideration of effect by beam-shaping filter

A fan angle of X-ray CT device used for measurement is 38°. An angle of X-ray from the center was defined “beam angle”. X-ray tube was stated at top position of rotation angle while the measurement. Along the beam angle, the data of the exposure dose and the Al Half Value Layer (HVL) were gotten from 0° to 19°. In this measurement, a semiconductor dosimeter called Rapidose (radcal corp. Monrovia, CA) was used. With using this dosimeter, we can obtain the exposure

dose, Al HVL and wave of tube voltage. This dosimeter is connected to PC by USB wire and these data are displayed on a PC screen (fig.1). We attempted to simulate phantom irradiation of the X-ray CT using these data obtained from the semiconductor dosimeter.

## 2.2 Computed Tomography Dose Index (CTDI) measurements

The Computed Tomography Dose Index (CTDI) is based on measuring the absorbed dose in a cylindrical acrylic phantom with a 10 cm pencil ion chamber in the phantom's center hole and four phantom's peripheral holes (0 ° ,90 ° ,180 ° ,270 ° ). This is useful when comparing several different CT (computed tomography) units. CTDI is derived from measuring the dose from a single scan.

CTDI peripheral (CTDI<sub>100,p</sub>) is the average of four doses, CTDI center (CTDI<sub>100,c</sub>) is dose at center position. A relative value was given by

$$A \text{ relative value} = \frac{CTDI_{100,p}}{CTDI_{100,c}} \quad (1)$$

With this relative value, we compared the measurement with the EGS5 calculation.

## 2.3 Comparison of measurement with EGS5 simulation

In the EGS5 simulation, the geometry of the situation same as measurement was made. The distance between the source and isocenter was 60 cm. The source rotated at intervals 2.8125 degrees (360/128) along the X-ray tube orbit, and photons were emitted at each position. The incident photon number at the each beam angle was calculated from the exposure dose at the same angle. The incident photon energy spectrum along the each beam angle was calculated by Birch's formula corresponding to measured Al HVL (Fig.2).

Four different types of the simulation with relative photon number and X-ray spectrum change at each beam angle were performed as follows:

- a) Only for the relative photon number
- b) Only for the energy change
- c) Both are considered (relative photon value and energy change)
- d) Neither is considered (relative photon value and energy change)

## 3. Results

### 3.1 Measured data of the Rapidose

The exposure dose and the effective energy calculated from Al HVL at each point were shown in Fig.3 (a) and Fig.3 (b). Distribution of the exposure dose was flat up to about 4 degrees of the beam angle, and at angles higher than 4 degrees the exposure dose decreased with increasing the beam angle. The effective energy was flat up to about 4 degrees of the beam angle, and at angles higher than 4 degrees the effective energy increased with increasing the beam angle.

### 3.2 Dose distribution in the acrylic phantom

Fig.4 shows dose distribution in the acrylic phantom using EGS5 simulation. The dose distributions of a)only the relative photon number and c)both are considered were comparatively homogeneous. On the other hand, dose distributions of b)only the energy change and d)both neither considered were inhomogeneous and the dose decreased from peripheral to the center. The dose distribution was little affected by the energy change. On the other hand, the dose distribution was significantly-affected whether or not to consider the relative photon number change along the beam angle.

### **3.3 Comparison of CTDI**

Fig.5 shows the relative value of CTDI (equation 1) in the simulation of four different types. The relative value of the CTDI by the measurement is 1.281. In contrast, the relative values of the CTDI by the four EGS5 simulations were a) 1.282, b) 2.322, c) 1.266 and d) 2.370.

As a result, the simulation value was higher around 2 times than measurement value when the relative photon number change was ignored. The measurement value and the simulation value were comparatively close when the relative photon number change was considered. The effect of energy change was negligible.

## **4. Discussion**

There was a difference between the measurement value and the simulation value whether or not to consider the effect of the beam-shaping filter in the simulation. For this reason, after X-rays transmitted thorough the beam-shaping filter, photon number around the center were significantly large and photon number rapidly decreased with increasing beam angle from the center. In recent years, the organ dose has been measured by placing the dosimeter in the anthropomorphic phantom with improved measurement technology. The organ dose has been also estimated using voxel phantom in the Monte Carlo simulation. In order to estimate the accurate organ dose in X-ray CT simulation, consideration of the beam-shaping filter is absolutely necessary.

## **5. Conclusions**

With the dose distribution obtained by the measured exposure dose and the X-ray spectrum calculated from Al HVL in the fan beam, the effect of beam-shaping filter was incorporated in X-ray CT Monte Carlo simulation. The measurement value and the simulation value were comparatively close when the dose distribution was considered. The dose distribution was especially important for the X-ray CT simulation.

## **References**

- 1) James V Athertont and Walter Huda , CT doses in cylindrical phantoms , *Phys. Med. Biol.* 40 (1995) 891-911.
- 2) N.Ogama et al ,The effective energy measurement of diagnosis domain X-ray, *Japanese Society of Radiological Technology* 57(5) 550-556 (2001)
- 3) M.TACHIBANA et al , Effect of the Beam-shaping Filter of Computed Tomography Scanners on the Conversion of Absorbed Dose in Water and a Polymethyl Methacrylate Phantom , *Japanese Society of Radiological Technology* 57(1) 51-58 (2001)



General Dose & Dose Rate	
Ave. Peak Voltage <b>113.4 kV</b>	Exposure Time <b>10.7 s</b>
Dose (Multi) <b>431.9 <math>\mu</math>Gy</b>	Dose Rate (Multi) <b>38.7 <math>\mu</math>Gy/s</b>
Half Value Layer <b>8.1 mm</b>	Typical Pulse Count <b>1</b>

(a) The appearance of the Rapidose

(b) The output on the PC screen

**Figure 1.** New type semiconductor dosimeter "Rapidose"

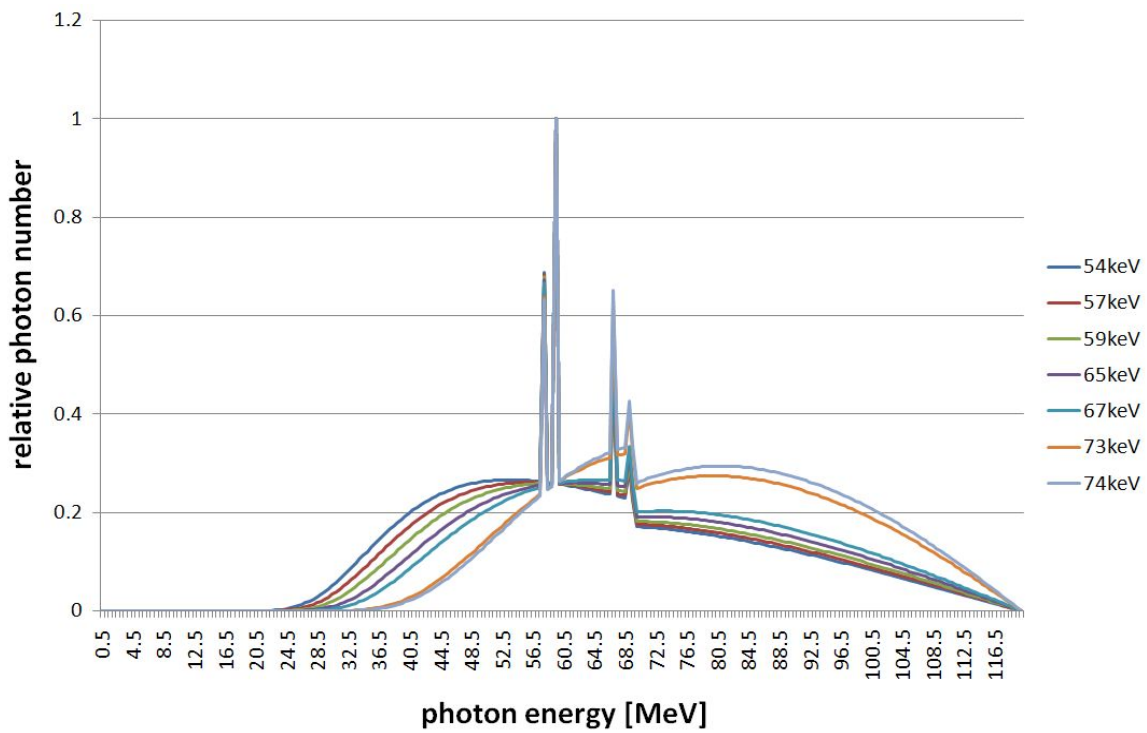


**Figure 2.** Incident spectrum of different seven energies were calculated by Birch's formula.

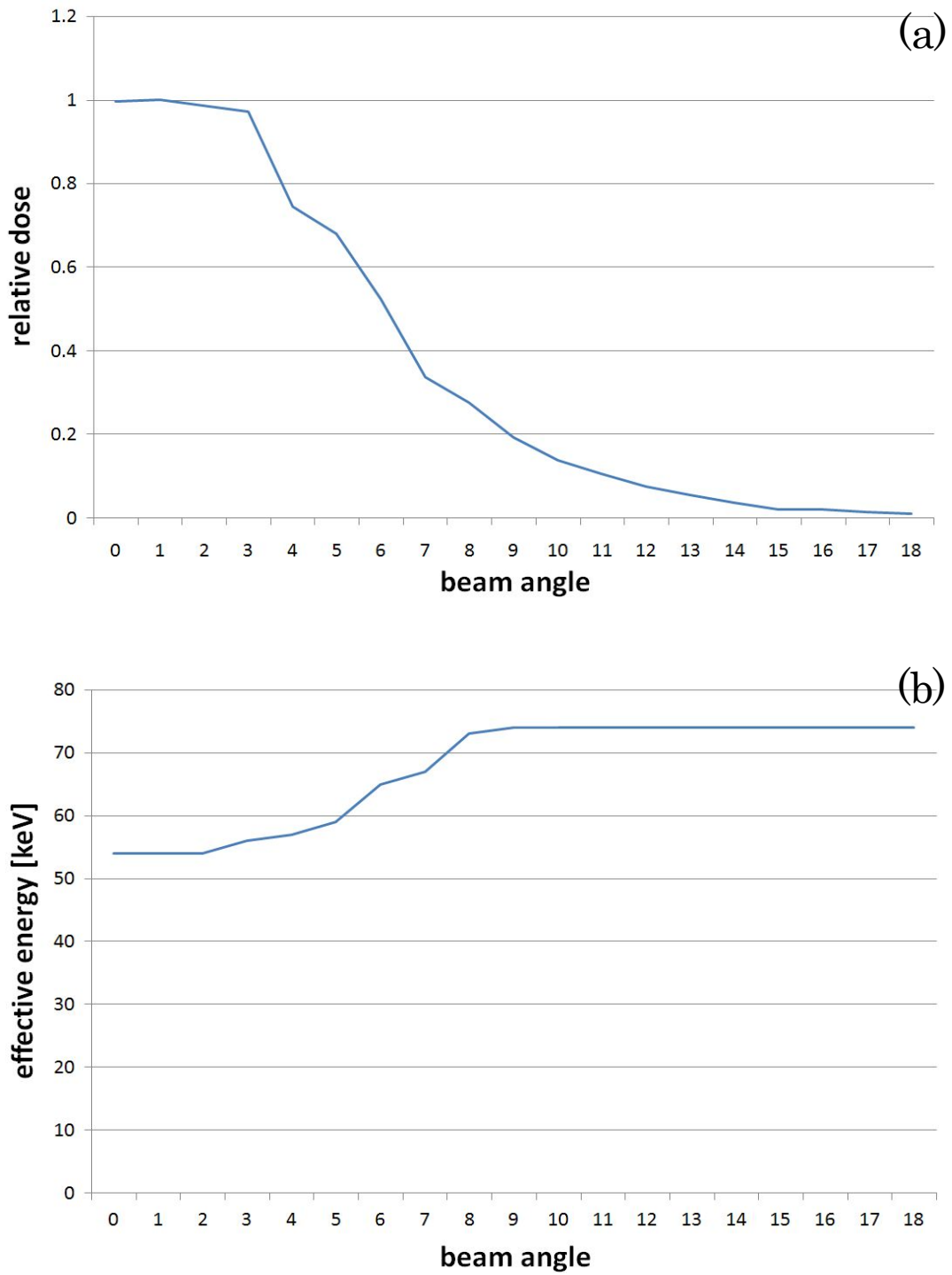


**Figure 3.** Relative dose and effective energy measured by Rapidose at each “beam angle”.

(a) The relative dose at each “beam angle”.

(b) The effective energy calculated by the Half Value Layer at each “beam angle”.

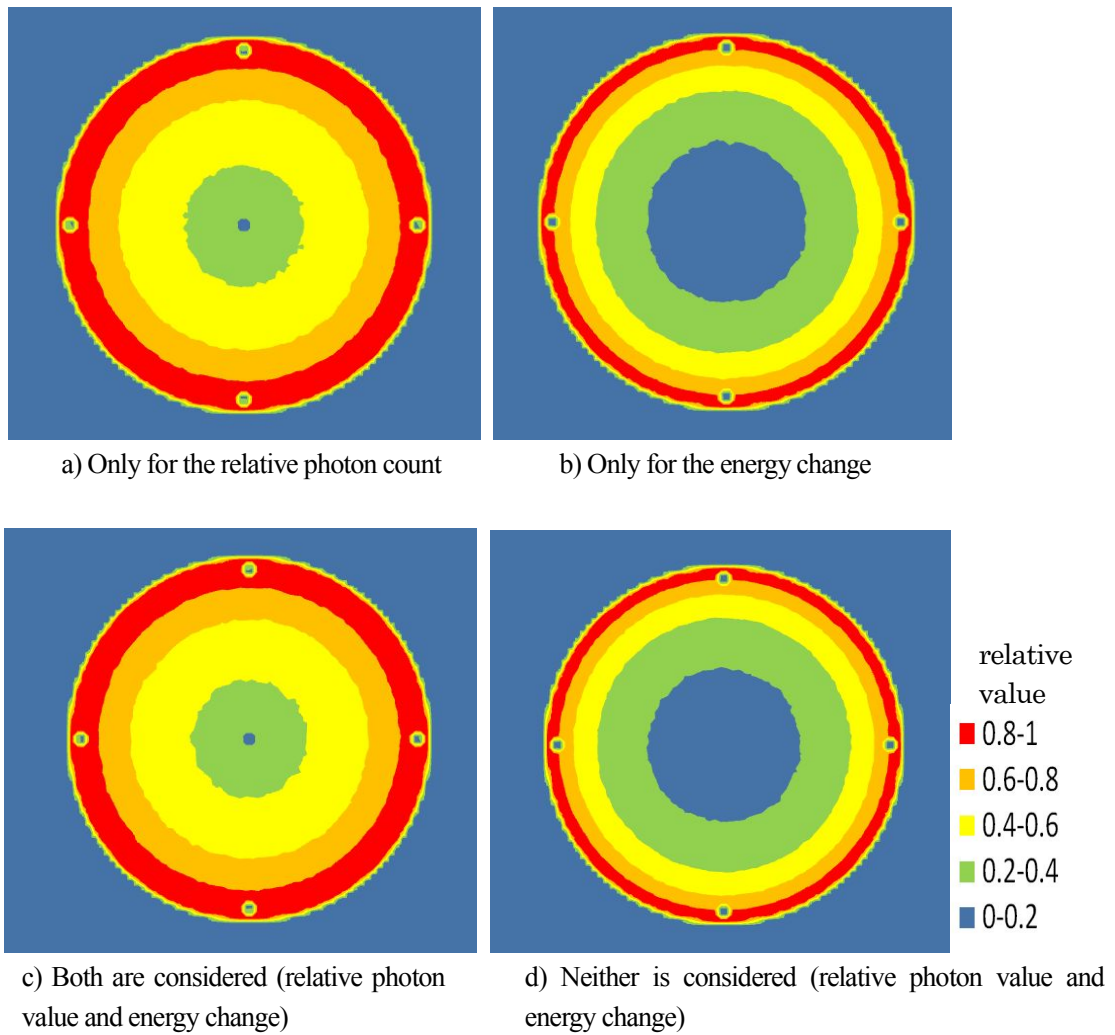


**Figure 4.** Dose distribution in the acrylic phantom with four different types.

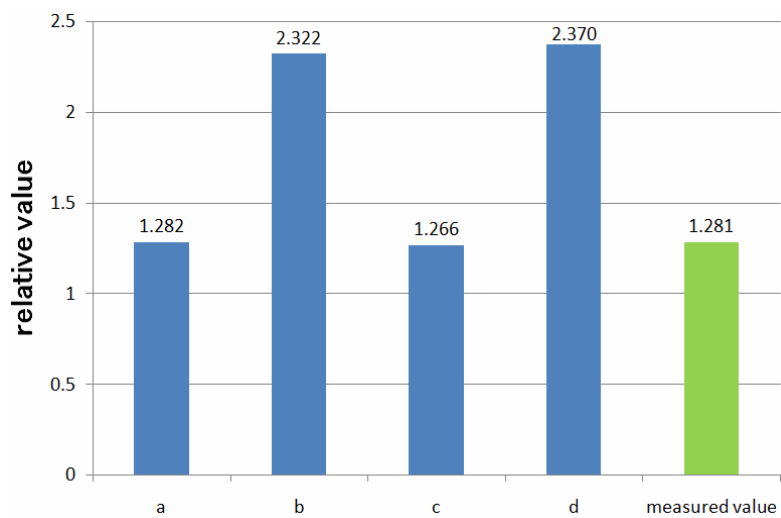


**Figure 5.** Relative value of CTDI with four different types.

- a) Only for the relative photon number
- b) Only for the energy change
- c) Both are considered (relative photon value and energy change)
- d) Neither is considered (relative photon value and energy change)

# Assessment of the validity of virtual grid using Monte Carlo code EGS5

Y. Chujo<sup>1</sup>, S. Koyama<sup>2</sup>,

*<sup>1</sup>Department of Radiological Technology, Graduate school medicine,  
Nagoya University,*

*1-1-20 Daikou-Minami, Higashi-ku, Nagoya, 461-8673, Japan*

*<sup>2</sup>Nagoya University School of Health Sciences*

*e-mail: y\_chujo@tokai-i.ac.jp*

## Abstract

Antiscatter grid is a equipment to reduce scattered radiation incident on the image plane. It is being generally used in plain radiography or mammography. Consideration of antiscatter grids is needed when Monte Carlo simulation is used to evaluate image quality in these situations. Because to build grid shape into a simulation geometry is possible but poses several issues we invented virtual grid with numerical calculation. Virtual grid reduces scattered radiation by angle calculation. In the present study, we presupposed that tube voltage, material of grid interspace, grid ratio and strip density were 80KV, aluminum, 8/1 and 60lines/cm respectively. We simulated geometry conformed to the experimental configuration of JISz4910 with Monte Carlo codes as EGS5. Physical performances of virtual grid were compared to experimental values and representative values. Though virtual grid don't exactly recreate an antiscatter grid, physical performances of which are acceptable. Because all you have to do is setting some parameters and you can add a grid to your program, we consider that virtual grid is useful.

## 1. Introduction

In recent years, using Monte Carlo simulation methods in diagnosis domain is increasing. When Monte Carlo simulation is used to evaluate image quality in diagnosis domain such as plain radiography or mammography, consideration of antiscatter grids may be needed. Antiscatter grid is an equipment to reduce scattered radiation incident on the image plane. Motion grid is generally used which employed with a reciprocating device during x-ray exposure so that the grid lines are blurred. Though it is possible to build grid shape into simulation geometry, there are following issues. The program is complicated. Enormous numbers of regions increase computation time. It is difficult that Motion grid is simulated with this method. Consequently, we invent virtual grid with numerical calculation and assess of the validity.

## 2. Methods

### 2.1 A virtual grid by calculation

At first region of antiscatter grid is separated into two layers at the midpoint. The medium of those regions is a material of grid interspace. We presuppose that lead strips are set becoming perpendicular to the X-axis. Whether a current particle should be discarded or not is decided with the coordinate data (x(np),u(np)) of particle at plane between two layers.

### 2.1.1 In the case of $x(np) > 0$ (figure 1,2)

“f0”, “h” and “D” are Focusing distance of antiscatter grid, height of lead strips and distance of lead strips respectively. Corresponding x-coordinate  $x_1$  to  $x(np)$  is calculated.

$x_1$  given by

$$x_1 = x(z_1 - h/2) / (f_0 + h/2) \\ = (1 - (h/2) / (f_0 + h/2)) x - D/2 \quad (1)$$

where  $x$  is the x-coordinate data  $x(np)$ . Magnitude of a vector  $r_1$  and  $r_2$  are calculated. “ $r_1$ ” is magnitude of the vector joining  $x_1$  to  $x(np)$ . “ $r_2$ ” is magnitude of the vector joining  $x_1 + D$  to  $x(np)$ .  $r_1$  and  $r_2$  are given as follows:

$$r_1 = \sqrt{(x - x_1)^2 + (h/2)^2} \quad (2)$$

$$r_2 = \sqrt{(x - x_1 - D)^2 + (h/2)^2} \quad (3)$$

“ $u_1$ ” and “ $u_2$ ” are direction cosine of  $r_1$  and  $r_2$  respectively.  $u_1$  and  $u_2$  are given as follows:

$$u_1 = (x - x_1) / r_1 \quad (4)$$

$$u_2 = (x - x_1 - D) / r_2 \quad (5)$$

In the case of  $u_2 > u_1$ , the particle satisfies an angle condition.

### 2.1.2 In the case of $x(np) = 0$ (figure 3)

Magnitude of a vector  $r_0$  and direction cosine  $u_0$  are calculated. “ $r_0$ ” is magnitude of the vector joining  $x_1$  to  $x(np)$ . “ $u_0$ ” is direction cosine of  $r_0$ .  $r_0$  and  $u_0$  are given as follows:

$$r_0 = \sqrt{(D/2)^2 + (h/2)^2} \quad (6)$$

$$u_0 = (D/2) / r_0 \quad (7)$$

In the case of  $u_0 > u(np)$ , the particle satisfies an angle condition.

### 2.1.3 In the case of $x(np) < 0$ (figure 4)

$x(np)$  is converted into positive value. Direction cosine  $u_1$  and  $u_2$  are calculated as previously described. “ $u_3$ ” and “ $u_4$ ” are values multiplied -1.0 by  $u_1$  and  $u_2$ . In the case of  $u_3 > u(np)$ , the particle satisfies an angle condition.

### 2.1.4 Scattered X-rays which go through lead strips

Part of particles which are dissatisfied with an angle condition go through lead strips. Then they reach detector. The rate of transmission depends on tube voltage or lead content. It has been calculated with tube voltage and lead content used by the following methods[1] in advance. Only particles which are dissatisfied with an angle condition are exposed to lead sheet obtained by the lead content. The rate of transmission “ $tr$ ” is given with deposit energy with or without lead sheet.

### 2.1.5 Primary X-ray falling on a lead strip

Part of particles which are satisfied with an angle condition collide with a lead strip not a spacer. The rate “loss” is given by

$$\text{loss} = d / (d + D) \quad (8)$$

“ $d$ ” and “ $D$ ” are thickness of strips and distance of strips. These particles are discarded.

### 2.1.6 Subroutine Howfar (figure 5)

Program for virtual grid is added in subroutine HOWFAR. It is necessary to input seven parameters (dis, height, thick, f0, grid1, grid2, tr) in the program. “dis” is distance of lead strips. “height” is height of lead strips. “thick” is thickness of lead strips. “f0” is focusing distance. “grid1” is region of incident side grid. “grid2” is region of exit side grid. “tr” is the rate that particles which are dissatisfied with an angle condition go through lead sheet. Whether a particle should be discarded or not is decided automatically by use of these parameters and random numbers.

## 2.2 Performance of virtual grid

We simulated to evaluate validity of physical performance of virtual grid. Geometry conformed to the experimental configuration of JIS z 4910 (figure 6). We presupposed that tube voltage, material of grid interspace, grid

ratio and strip density were 80KV, aluminum, 8/1 and 60lines/cm respectively. For the calculation of primary transmission, narrow-beam geometry was used. For the calculation of total transmission, broad-beam geometry was used. Primary and total transmission were calculated from the ratio of deposition energy in the fluorescence substance with and without a grid.

### 3. RESULTS AND DISCUSSION

Table 1 shows the transmission of primary radiation and the transmission of total radiation obtained from experimental measurements and Monte Carlo calculations. The experimental values were extracted a treatise[2]. The representative values were released values from a manufacturer[3]. The numbers of histories for the primary transmission were about 20,000,000 particles. The fractional standard deviation were 0.80% and 0.65%, with and without a grid respectively. The numbers of histories for the total transmission were about 6,400,000,000 particles. The fractional standard deviations were 1.30% and 0.94%, with and without a grid respectively. The uncertainties of primary transmission and total transmission in the Monte Carlo results for the experimental value are 2% and 0.8%. K means contrast improvement factor. K is defined as the ratio of radiographic contrast with a grid to that without a grid. B is defined as the factor by which the incident radiation is increased. K and B are given as follows:

$$K = T_p/T_t \quad (9)$$

$$B = 1/T_t \quad (10)$$

where  $T_p$  is the transmission of primary radiation and  $T_t$  is the transmission of total radiation of the grid. The uncertainties of K and B in the Monte Carlo results for the experimental values were 3% and 0.8%. The uncertainties of K and B in the Monte Carlo results for the representative values were 13% and 7.7%. The uncertainties of Monte Carlo results for the experimental values were lower than that of the experimental values for the representative values.

### 4. CONCLUSION

The purpose of this study is not a performance evaluation of a grid. The purpose is to add a grid to individual program readily. Though virtual grid don't exactly recreate an antiscatter grid, physical performances of which are acceptable compared with experimental values or representative values. All you have to do is setting some parameters and you can add a grid to your program. Therefore we consider that virtual grid is useful. Further studies are needed to verify validity in other conditions; tube voltage, grid ratio and strip density.

### References

- [1] H.Maruishi et al., Theory of X-ray Transmission through an Anti-scatter Grid, Japanese Society of Radiological Technology 55(7) 692-699 (1999)
- [2] M.Ishikawa et al., Physical Characteristics of Anti-scatter Grids According to Old and New JIS Standards, Japanese Society of Radiological Technology 60(8) 1123-1131(2004)
- [3] Mitaya Manufacturing Co.,Ltd.

**Table 1** Comparison of physical performances

	$T_p$	$T_t$	K	B
Experimental value	0.638	0.254	2.51	3.94
representative value	-	-	2.97	4.30
Monte Carlo result	0.651	0.252	2.58	3.97

Tp: Transmission of primary radiation, Tt: Transmission of total radiation,  
 K: Contrast improvement ratio, B: Grid exposure factor

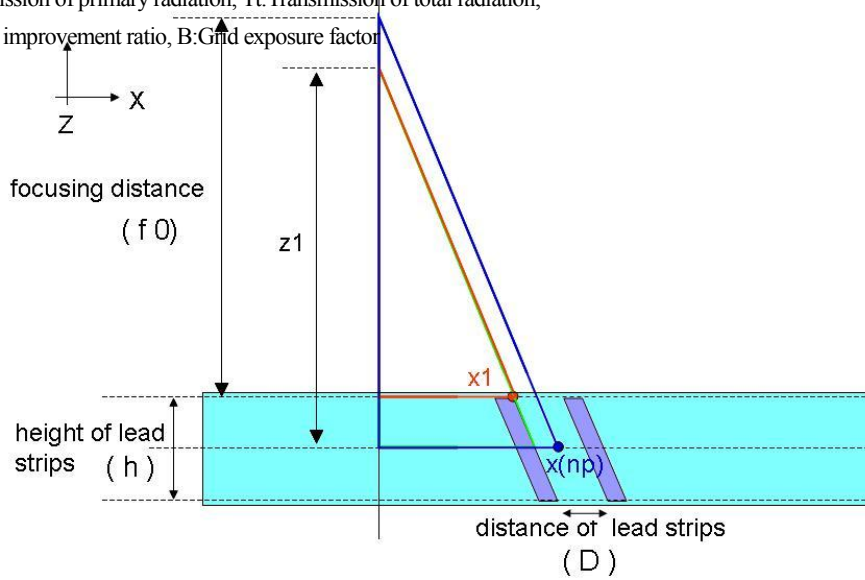


**Figure 1.** Conceptual diagram in the case of  $x(np) > 0$ .

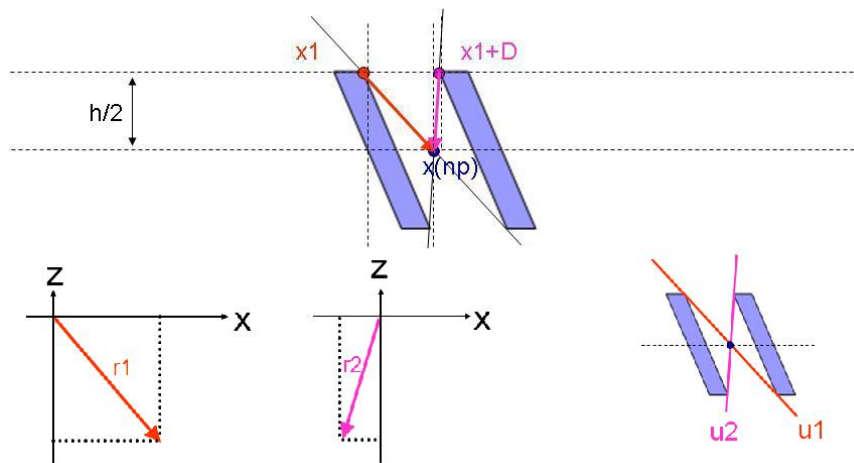


**Figure 2.** Direction cosine in the case of  $x(np) > 0$ .

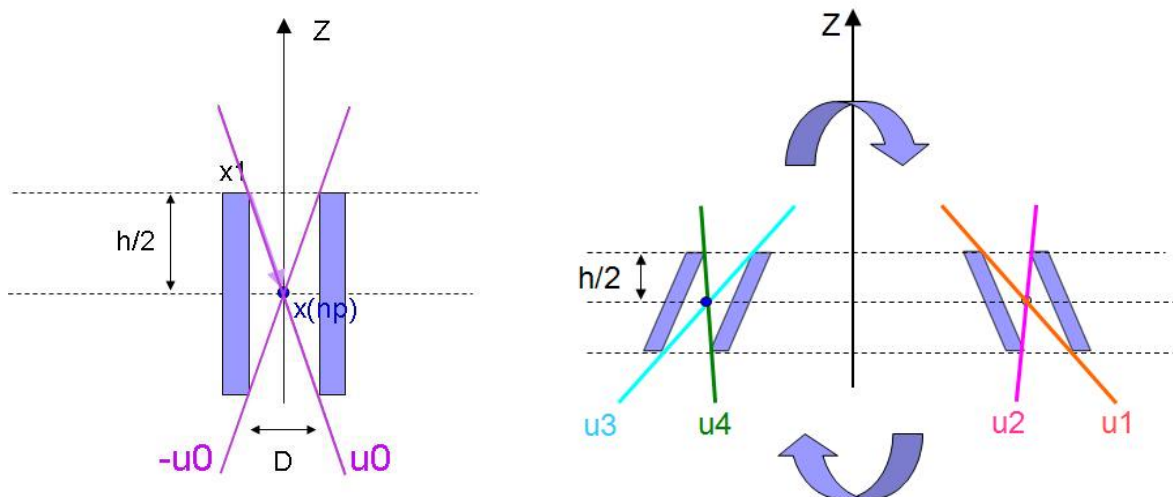


**Figure 3.** Conceptual diagram in the case of  $x(np)=0$ .

```

c
dis=0.012      ! distance of strips
height=0.096  ! height of strips
thick=0.0045  ! thickness of strips
f0=100.0      ! focusing distance
grid1=5        ! region of incident side grid
grid2=6        ! region of exit side grid
tr=0.0471     ! fraction transmitted
loss=thick/(dis+thick)
if(ir(np).eq.grid2)then
if(ir(np).ne.iroid.and.iroid.eq.grid1.and.iarg.eq.0.
and.ia(np).eq.0)then
if(x(np).eq.0)then
r=dsqrt((dis/2)**2+(height/2)**2)
u0=(dis/2)/r
u00=u0*(-1.0)
if(u(np).lt.u00.or.u(np).gt.u0)then
call randomset(rans1)
if(rans1.le.tr)then
goto 189
end if
idisc=1
else
goto 188
end if
else if(x(np).gt.0)then
x1=(1-(height/2)/(f0+height/2))*x(np)-(dis/2)
r1=dsqrt((x(np)-x1)**2+(height/2)**2)
u1=(x(np)-x1)/r1
r2=dsqrt((x(np)-x1-dis)**2+(height/2)**2)
u2=(x(np)-x1-dis)/r2
if(u(np).lt.u2.or.u(np).gt.u1)then
call randomset(rans2)
if(rans2.le.tr)then
goto 189
end if
idisc=1
else
goto 188
end if
end if

```

**Figure 4.** Conceptual diagram in the case of  $x(np)<0$ .

```

else
xa=x(np)*(-1.0)
x1=(1-(height/2)/(f0+height/2))*xa-(dis/2)
r1=dsqrt((xa-x1)**2+(height/2)**2)
u1=(xa-x1)/r1
r2=dsqrt((xa-x1-dis)**2+(height/2)**2)
u2=(xa-x1-dis)/r2
u3=u1*(-1.0)
u4=u2*(-1.0)
if(u(np).lt.u3.or.u(np).gt.u4)then
call randomset(rans3)
if(rans3.le.tr)then
goto 189
end if
idisc=1
else
goto 188
end if
end if
188 continue
call randomset(ranloss)
if(ranloss.le.loss)then
idisc=1
end if
end if
end if
189 continue

```

**Figure 5.** Instance case of subroutine HOWFAR.

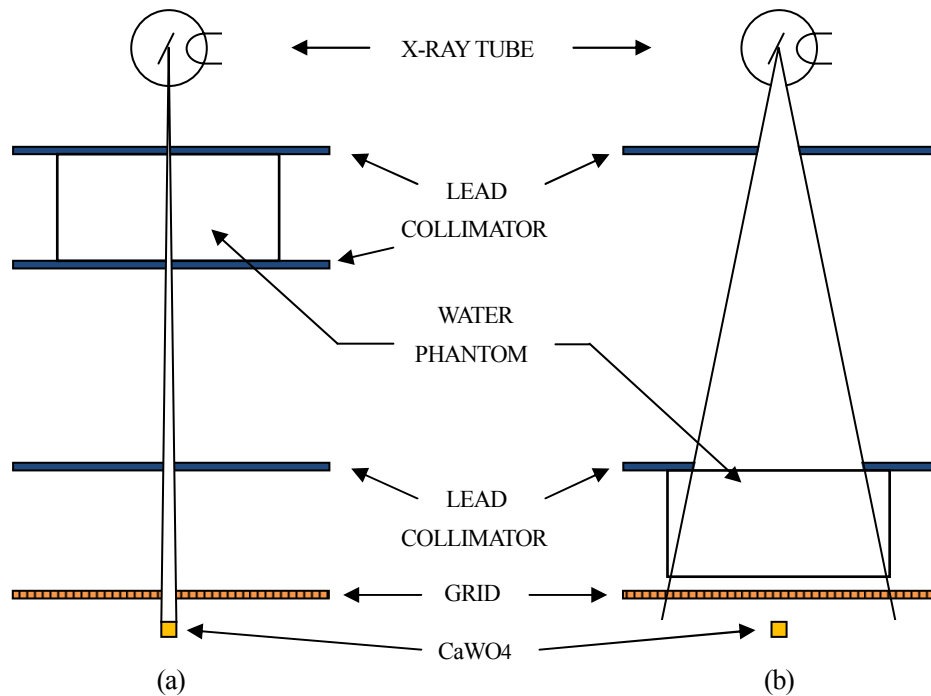


**Figure 6.** Geometry for (a) primary transmission and (b) total transmission.

# SIMULATIONS OF PHOTON SPECIFIC ABSORBED FRACTIONS IN A MOUSE VOXEL PHANTOM

A. Mohammadi<sup>1</sup> and S. Kinase<sup>1</sup>

<sup>1</sup>Japan Atomic Energy Agency,  
2-4 Shirakata, Shirane, Tokai-mura, Naka-gun, Ibaraki 319-1195, Japan  
e-mail: mohammadi.akram@jaea.go.jp

## Abstract

For preclinical assessments of several radiopharmaceuticals, photon SAFs were evaluated using a voxel-based mouse phantom. The sources were considered to be mono-energetic in the photon energy range from 10 keV to 4 MeV. The radiation transport was simulated using the Monte Carlo method. Consequently, it was confirmed that the photon SAFs for organ self-absorption are dependent on the masses of the source/target organs. The photon SAFs for self- and cross-irradiation changed continuously with photon energy emitted by the source. The photon SAFs for cross-irradiation might be subject to the geometry effect, such as size and shape of source/target and distance between the source and target. In addition, photon-only S values were calculated in spleen and liver of the mouse phantom for <sup>131</sup>I, <sup>153</sup>Sm and <sup>188</sup>Re using the results of the photon SAFs.

## 1. Introduction

Preclinical evaluations of new radiopharmaceuticals are performed in murine, such as mouse and rat, before testing is started in humans. Understanding dose responses, radiation-related side-effects and toxicity of radiopharmaceuticals makes these studies more important since they can be translated to preclinical results for humans. Accurate dose estimates for these animals have become indispensable. In particular, mice are widely used in the preclinical examinations. Various studies have been performed on mouse organ dosimetry [1-6]. The absorbed doses of the organs were estimated by the point-kernel convolution [1,2] and the Monte Carlo method [3-6]. Organ doses can be estimated by applying the Medical Internal Radiation Dose (MIRD) method, which uses specific absorbed fractions (SAFs in kg<sup>-1</sup>) - the absorbed fraction in the target organ per unit mass of the target organ - or S values (Gy/Bq.s), mean absorbed dose to a target organ per unit cumulated activity in the source organ.

Mouse dosimetry was done using several mathematical mouse phantoms. A stylized mouse phantom [1-3], which used ellipsoids, spheroids and cylinders as organs, was applied to evaluate SAFs and S values for some organs. To improve the accuracy of dosimetry, voxel mouse phantoms[4-6] which have a more realistic anatomy were developed from computed tomography (CT) and magnetic resonance imaging (MRI) data.

To perform accurate absorbed dose calculations, it may be important to use voxel phantom data with similar anatomy and size of the organs to the mouse being used in a particular experimental study. Dosimetry of mouse with different sizes seems to be worth since these animals are widely used in preclinical studies of radiopharmaceutical developments. The specific absorbed fractions of photons for self- and cross-irradiation can be used to predict mouse-organ doses. These factors are an effective tool for the preclinical dose estimates required to develop radiopharmaceuticals which emit photons. For the reasons we evaluated photon SAFs in a mouse voxel phantom using the Monte Carlo method in the energy range from 10 keV to 4 MeV and then obtained photon-only S values for <sup>131</sup>I,

$^{153}\text{Sm}$  and  $^{188}\text{Re}$  for liver and spleen dosimetry.

## 2. Materials and Methods

### 2.1 Digimouse voxel phantom

The general geometry setting for "Digimouse" phantom [7] was used. The Digimouse phantom was generated using co-registered micro-CT and color cryosection images of a normal nude male mouse. This phantom was developed at the University of Southern California. A matrix of  $380 \times 992 \times 208$  elements, with a voxel size of 0.1 mm was constructed. The organs segmented from these data are: whole brain, external cerebrum, cerebellum, olfactory bulbs, striatum, medulla, masseter muscles, eyes, lachrymal glands, heart, lungs, liver, stomach, spleen, pancreas, adrenal glands, kidneys, testes, bladder, skeleton and skin.

### 2.2 Specific absorbed fractions

The Digimouse phantom was converted to an input file for the Monte Carlo code, EGS4 [8], in conjunction with an EGS4 user code, UCSAF [9]. In the EGS4-UCSAF code, the transport of photons in the phantom was simulated and the correlations between primary and secondary particles are included. The material composition and density of the simulated organs were assumed the same as human tissues and they were taken from the report 44 of ICRU (the International Commission on Radiation Unit and Measurement) [10]. Three different tissues were considered for the mouse organs including skeleton ( $1.40 \text{ g/cm}^3$ ), soft tissue ( $1.04 \text{ g/cm}^3$ ) and lungs ( $0.269 \text{ g/cm}^3$ ). The mass of each organ was calculated from the number of voxels of the organ and the organ density. **Table 1** shows the mass of simulated organs of the Digimouse.

Major abdominal organs were assumed as the source and the target and the others were only considered as the targets. Each source organ was evaluated separately in order to calculate the SAFs from the absorbed energy within the organs. The source was distributed uniformly in the main organs and emitted isotropically. Mono-energetic photon particles were simulated for the chosen source organs. Photon energies were 10, 15, 20, 30, 40, 50, 100, 200, 500, 1000, 1500, 2000 and 4000 keV. The photon and electron cut-offs energy were set to 1 keV and the photon histories were run at numbers sufficient ( $10^7$ ) to reduce uncertainties (fractional standard deviation [FSDs]) less than 5%. The cross section data for photons and electrons were taken from PHOTX [11, 12] and ICRU report 37 [13], respectively.

### 2.3 Photon-only S values

Photon-only S values in the spleen and liver were calculated for the Digimouse phantom using the results of photon SAFs.  $^{131}\text{I}$ ,  $^{153}\text{Sm}$  and  $^{188}\text{Re}$  were considered as interested nuclides for liver and spleen dosimetry. The photon SAFs were converted to photon-only S values considering energies of emitted photons from the radioisotopes. The photon emitted for  $^{131}\text{I}$ ,  $^{153}\text{Sm}$  and  $^{188}\text{Re}$  were extracted from decay data [14] and the photons with the intensities higher than 1% were used for calculation of S values.

## 3. Results and discussion

### 3.1 Specific absorbed fractions

Photon SAFs in eleven identified organs including skeleton, heart, bladder, testes, stomach, spleen, pancreas, liver, kidneys, adrenal glands and lungs of the Digimouse were calculated at discrete initial photons from 10 keV to 4 MeV. The photon SAFs for self- and cross-irradiation in the chosen organs are given in **Table 2**. The SAFs values set to zero when the FSDs exceed 5% for the purpose of calculating S values for the radio nuclides.

**Figure 1** shows the photon SAFs for self-irradiation, the source organ is the target organ, for the Digimouse in the photon energy range from 10 keV to 4 MeV in heart, spleen, liver, pancreas and stomach. The photon SAFs for self-irradiation changes continuously with initial photon energy for all organs hence it depends on photon energy. In this

figure, the SAFs has the highest and lowest values for pancreas and liver while these organs are lightest and heaviest organs among heart, stomach and spleen. Thus, the mass dependency of SAFs for self-irradiation is confirmed from the results.

**Figure 2** is an example of photon SAFs for cross-irradiation, the source organ is not the target organ, in the photon energy range from 10 keV to 4 MeV. Figure 2(a) gives the photon SAFs in bladder while source is distributed in heart, stomach, spleen, pancreas, or liver and figure 2(b) shows the SAFs in heart, stomach, spleen, pancreas, and liver while source is in bladder. The SAFs in liver and spleen for all energy have the same values although the masses of them are completely different with large difference. These results suggest that the photon SAFs for cross irradiation do not always change with the differences in mass of targets. It seems that the geometry including source size, target size and their distance significantly affect on the SAFs for cross-irradiation since SAFs for heart/bladder and pancreas/bladder in figure 2 have maximum and minimum value due to longest and shortest distance between source and target. The SAFs for cross-irradiation show a maximum in 30 keV and for photons with energies higher than 100 keV the SAFs change smoothly with the photon energy. Figures 2(a) and (b) seem almost the same and show validity of the reciprocity principle for the photon SAFs in the Digimouse phantom.

### 3.2 Photon-only S values

Photon-only S values in the liver and spleen of the Digimouse are compared with Kolbert et al. results in Fig. 3 and Fig. 4 for self-irradiation and cross-irradiation respectively. Kolbert *et al.* results were obtained in a mouse voxel phantom using the point kernel method. The masses of liver and spleen in their study are 1.530 and 0.064 g. Large differences can be observed between S values obtained for self-irradiation especially for spleen owing to large difference between mass of spleen in two studies (fig. 4(a)). The S values for cross-irradiation from Kolbert *et al.* studies are even lower than half of S values in this study for liver and spleen (fig. 4(b)), and this large discrepancy is attributed to the different geometry of phantoms and different calculation methods. Comparison of S values for cross-irradiation in liver and spleen for this study (figures 4(a) and (b)) shows that the reciprocal dose principle is valid within 1.6%.

## 4. Conclusions

The specific absorbed fractions (SAFs) of photons in the Digimouse phantom were evaluated using EGS4-UCSAF code. The new set of photon SAFs were tabulated for the photon energies from 10 keV to 4 MeV in order to evaluate mouse organ doses in preclinical experiments of new radiopharmaceuticals. In this study, it was confirmed that the photon SAFs for self-irradiation depended on the photon energy and the mass of the target/source organ. The photon SAFs for cross-irradiation also was an energy dependent function but did not change by the mass of target and it might be affected by source size, target size, their shape and distance between the source and target. Organ dose evaluation should be performed in the phantom with the Monte Carlo method since the minor changes in the geometry had a large effect on photon-only S values and organ dose. From photon-only S value results, it can be stated that minor changes in the source-target geometry are likely to change dramatically the resulting S values. The photon SAFs or S values is an effective tool for the preclinical dose evaluations required to develop pharmaceuticals which emit photons.

## Acknowledgments

The authors would like to thank Dr. Ishioka, the group leader of radioisotope drug delivery systems group, Japan Atomic Energy Agency, for her support to this work.

## References

- 1) T. E. Hui, D. R. Fisher, J. A. Kuhn, L. E. Williams, C. Nourigat, C. C. Badger, B. G. Beatty and J. D. Beatty, "A mouse model for calculating cross-organ beta-doses from yttrium-90-labeled immunoconjugates," *Cancer*, 73, 951 (1994).

- 2) K. S. Kolbert, T. Watson, C. Matei, S. Xu, J. A. Koutcher and G. Sgouros, "Murine S factors for liver, spleen, and kidney", *J. Nucl. Med.* 44, 784 (2003).
- 3) C. Hindorf, M. Ljungberg and S-E. Strand, "Evaluation of parameters influencing S values in mouse dosimetry," *J. Nucl. Med.* 45, 1960 (2004).
- 4) M. G. Stabin, T. E. Peterson, G. E. Holburn and M. A. Emmons, Voxel-based mouse and rat models for internal dose calculations," *J. Nucl. Med.* 47, 655 (2006).
- 5) A. Bitar, A. Lisbona, P. Thedrez, C. S. Maurel, D. L. Forestier, J. Barbet and M. Bardies, "A voxel-based mouse for internal dose calculations using Monte Carlo simulations (MCNP)," *Phys. Med. Biol.* 52, 1013 (2007).
- 6) R. Taschereau and A. F. Chatziioannou, "Monte Carlo simulations of absorbed dose in a mouse phantom from 18-fluorine compounds," *Med. Phys.* 34, 1026 (2007).
- 7) B. Dogdas, D. Stout, A. F. Chatziioannou and R. M. Leahy, "Digimouse: a 3D whole body mouse atlas from CT and cryosection data," *Phys. Med. Biol.* 52, 577 (2007).
- 8) W. R. Nelson, H. Hirayama and D. W. O. Rogers, "The EGS4 Code System," SLAC-265 (1985).
- 9) S. Kinase, M. Zankl, *et al.*, "Evaluation of specific absorbed fractions in voxel phantoms using Monte Carlo simulation," *Radiat. Prot. Dosi.* 105, 557 (2003).
- 10) "Tissue substitutes in radiation dosimetry and measurement", ICRU Report 44 International Commission on Radiation Units and Measurements (1989).
- 11) "Photon Interaction Cross Section Library," DLC-136/PHOTX, contributed by National Institute of Standards and Technology (1989).
- 12) Y. Sakamoto, "Photon cross section data PHOTX for PEGS4," KEK Proceedings 93-15, 77-82(in Japanese).
- 13) "Stopping Powers for Electrons and Positrons," ICRU Report 37 International Commission on Radiation Units and Measurements (1984).
- 14) A., Endo and Y. Yamaguchi (2001), "Compilation of Nuclear Decay Data Used for Dose Calculation Revised Data for Radionuclides Listed in ICRP Publication 38", JAERI-Data/Code 2001-004.

**Table 1** The mass of simulated organs of the Digimouse

Organ	Organ mass (g)
Skin	$1.7 \times 10^1$
Skeleton	$1.7 \times 10^0$
Eye	$5.8 \times 10^{-3}$
Medulla	$4.8 \times 10^{-2}$
Striatum	$2.7 \times 10^{-2}$
Olfactory bulbs	$1.9 \times 10^{-2}$
External cerebrum	$1.4 \times 10^{-1}$
Cerebellum	$3.2 \times 10^{-2}$
Heart	$2.3 \times 10^{-1}$
Rest of the brain	$1.6 \times 10^{-1}$
Masseter muscles	$1.1 \times 10^{-1}$
Lachrymal glands	$3.2 \times 10^{-2}$
Bladder	$2.0 \times 10^{-1}$
Testis	$1.6 \times 10^{-1}$
Stomach	$2.3 \times 10^{-1}$
Spleen	$1.4 \times 10^{-1}$
Pancreas	$4.7 \times 10^{-2}$
Liver	$2.1 \times 10^0$
Kidneys	$5.1 \times 10^{-1}$
Adrenal glands	$5.9 \times 10^{-3}$
Lungs	$1.2 \times 10^{-1}$

**Table 2** Photon specific absorbed fractions (SAFs in 1/kg) in some organs of the Digimouse phantom (1).

<b>Source organ : Skeleton</b>										
Energy(MeV)	Skeleton	Heart	Bladder	Stomach	Spleen	Pancreas	Liver	Kidneys	Adrenal	Lungs
0.01	3.9×10 <sup>2</sup>	1.6×10 <sup>1</sup>	1.3×10 <sup>0</sup>	3.1×10 <sup>0</sup>	2.4×10 <sup>0</sup>	0.0	6.8×10 <sup>0</sup>	2.1×10 <sup>0</sup>	1.0×10 <sup>1</sup>	4.5×10 <sup>1</sup>
0.015	2.7×10 <sup>2</sup>	1.9×10 <sup>1</sup>	5.1×10 <sup>0</sup>	5.3×10 <sup>0</sup>	3.9×10 <sup>0</sup>	2.7×10 <sup>0</sup>	8.8×10 <sup>0</sup>	5.1×10 <sup>0</sup>	1.5×10 <sup>1</sup>	3.6×10 <sup>1</sup>
0.02	1.6×10 <sup>2</sup>	1.4×10 <sup>1</sup>	5.9×10 <sup>0</sup>	5.4×10 <sup>0</sup>	4.0×10 <sup>0</sup>	3.5×10 <sup>0</sup>	7.6×10 <sup>0</sup>	5.6×10 <sup>0</sup>	1.2×10 <sup>1</sup>	2.3×10 <sup>1</sup>
0.03	6.2×10 <sup>1</sup>	6.2×10 <sup>0</sup>	3.3×10 <sup>0</sup>	2.9×10 <sup>0</sup>	2.4×10 <sup>0</sup>	2.4×10 <sup>0</sup>	3.7×10 <sup>0</sup>	3.1×10 <sup>0</sup>	0.0	9.1×10 <sup>0</sup>
0.05	1.6×10 <sup>1</sup>	2.0×10 <sup>0</sup>	1.2×10 <sup>0</sup>	1.0×10 <sup>0</sup>	8.1×10 <sup>-1</sup>	9.1×10 <sup>-1</sup>	1.2×10 <sup>0</sup>	1.1×10 <sup>0</sup>	0.0	2.7×10 <sup>0</sup>
0.1	4.2×10 <sup>0</sup>	1.2×10 <sup>0</sup>	6.7×10 <sup>-1</sup>	6.1×10 <sup>-1</sup>	5.1×10 <sup>-1</sup>	4.8×10 <sup>-1</sup>	7.5×10 <sup>-1</sup>	6.5×10 <sup>-1</sup>	0.0	1.6×10 <sup>0</sup>
0.2	3.5×10 <sup>0</sup>	1.3×10 <sup>0</sup>	7.4×10 <sup>-1</sup>	6.8×10 <sup>-1</sup>	5.7×10 <sup>-1</sup>	5.4×10 <sup>-1</sup>	8.4×10 <sup>-1</sup>	7.3×10 <sup>-1</sup>	0.0	1.7×10 <sup>0</sup>
0.5	3.4×10 <sup>0</sup>	1.5×10 <sup>0</sup>	8.5×10 <sup>-1</sup>	7.8×10 <sup>-1</sup>	6.2×10 <sup>-1</sup>	6.1×10 <sup>-1</sup>	9.3×10 <sup>-1</sup>	8.1×10 <sup>-1</sup>	0.0	1.9×10 <sup>0</sup>
1	2.5×10 <sup>0</sup>	1.4×10 <sup>0</sup>	7.8×10 <sup>-1</sup>	7.3×10 <sup>-1</sup>	5.9×10 <sup>-1</sup>	6.0×10 <sup>-1</sup>	8.8×10 <sup>-1</sup>	7.7×10 <sup>-1</sup>	0.0	1.6×10 <sup>0</sup>
1.5	1.8×10 <sup>0</sup>	1.2×10 <sup>0</sup>	7.4×10 <sup>-1</sup>	6.7×10 <sup>-1</sup>	5.3×10 <sup>-1</sup>	5.6×10 <sup>-1</sup>	7.8×10 <sup>-1</sup>	7.2×10 <sup>-1</sup>	0.0	1.3×10 <sup>0</sup>
2	1.4×10 <sup>0</sup>	1.0×10 <sup>0</sup>	6.7×10 <sup>-1</sup>	5.7×10 <sup>-1</sup>	4.9×10 <sup>-1</sup>	5.3×10 <sup>-1</sup>	6.9×10 <sup>-1</sup>	6.5×10 <sup>-1</sup>	0.0	1.1×10 <sup>0</sup>
4	6.6×10 <sup>-1</sup>	5.7×10 <sup>-1</sup>	4.4×10 <sup>-1</sup>	4.0×10 <sup>-1</sup>	3.4×10 <sup>-1</sup>	3.6×10 <sup>-1</sup>	4.3×10 <sup>-1</sup>	4.2×10 <sup>-1</sup>	5.5×10 <sup>-1</sup>	5.4×10 <sup>-1</sup>
<b>Source organ : Liver</b>										
Energy(MeV)	Skeleton	Heart	Bladder	Stomach	Spleen	Pancreas	Liver	Kidneys	Adrenal	Lungs
0.01	2.3×10 <sup>1</sup>	3.1×10 <sup>1</sup>	2.8×10 <sup>1</sup>	8.2×10 <sup>1</sup>	1.8×10 <sup>1</sup>	3.1×10 <sup>1</sup>	3.2×10 <sup>2</sup>	2.9×10 <sup>1</sup>	1.3×10 <sup>2</sup>	7.3×10 <sup>1</sup>
0.015	3.2×10 <sup>1</sup>	3.8×10 <sup>1</sup>	2.7×10 <sup>0</sup>	8.0×10 <sup>1</sup>	2.6×10 <sup>1</sup>	3.5×10 <sup>1</sup>	2.1×10 <sup>2</sup>	3.4×10 <sup>1</sup>	1.1×10 <sup>2</sup>	6.6×10 <sup>1</sup>
0.02	2.8×10 <sup>1</sup>	2.8×10 <sup>1</sup>	4.4×10 <sup>0</sup>	5.2×10 <sup>1</sup>	2.2×10 <sup>1</sup>	2.6×10 <sup>1</sup>	1.1×10 <sup>2</sup>	2.6×10 <sup>1</sup>	6.8×10 <sup>1</sup>	4.2×10 <sup>1</sup>
0.03	1.4×10 <sup>1</sup>	1.1×10 <sup>1</sup>	2.8×10 <sup>0</sup>	2.0×10 <sup>1</sup>	9.3×10 <sup>0</sup>	1.1×10 <sup>1</sup>	3.8×10 <sup>1</sup>	1.1×10 <sup>1</sup>	2.4×10 <sup>1</sup>	1.6×10 <sup>1</sup>
0.05	3.9×10 <sup>0</sup>	3.5×10 <sup>0</sup>	9.7×10 <sup>-1</sup>	5.9×10 <sup>0</sup>	2.9×10 <sup>0</sup>	3.4×10 <sup>0</sup>	1.1×10 <sup>1</sup>	3.4×10 <sup>0</sup>	7.3×10 <sup>0</sup>	4.7×10 <sup>0</sup>
0.1	1.1×10 <sup>0</sup>	2.1×10 <sup>0</sup>	5.9×10 <sup>-1</sup>	3.4×10 <sup>0</sup>	1.7×10 <sup>0</sup>	2.0×10 <sup>0</sup>	6.6×10 <sup>0</sup>	2.0×10 <sup>0</sup>	4.5×10 <sup>0</sup>	2.6×10 <sup>0</sup>
0.2	8.5×10 <sup>-1</sup>	2.3×10 <sup>0</sup>	6.6×10 <sup>-1</sup>	3.9×10 <sup>0</sup>	2.0×10 <sup>0</sup>	2.2×10 <sup>0</sup>	7.5×10 <sup>0</sup>	2.2×10 <sup>0</sup>	4.6×10 <sup>0</sup>	2.8×10 <sup>0</sup>
0.5	9.1×10 <sup>-1</sup>	2.5×10 <sup>0</sup>	7.0×10 <sup>-1</sup>	4.2×10 <sup>0</sup>	2.1×10 <sup>0</sup>	2.5×10 <sup>0</sup>	7.9×10 <sup>0</sup>	2.4×10 <sup>0</sup>	5.4×10 <sup>0</sup>	3.2×10 <sup>0</sup>
1	8.4×10 <sup>-1</sup>	2.4×10 <sup>0</sup>	6.6×10 <sup>-1</sup>	4.0×10 <sup>0</sup>	2.0×10 <sup>0</sup>	2.3×10 <sup>0</sup>	6.6×10 <sup>0</sup>	2.3×10 <sup>0</sup>	4.9×10 <sup>0</sup>	2.9×10 <sup>0</sup>
1.5	7.5×10 <sup>-1</sup>	2.1×10 <sup>0</sup>	6.3×10 <sup>-1</sup>	3.5×10 <sup>0</sup>	1.8×10 <sup>0</sup>	2.0×10 <sup>0</sup>	5.3×10 <sup>0</sup>	2.0×10 <sup>0</sup>	3.8×10 <sup>0</sup>	2.5×10 <sup>0</sup>
2	6.5×10 <sup>-1</sup>	1.9×10 <sup>0</sup>	5.9×10 <sup>-1</sup>	2.9×10 <sup>0</sup>	1.6×10 <sup>0</sup>	1.8×10 <sup>0</sup>	4.1×10 <sup>0</sup>	1.8×10 <sup>0</sup>	3.4×10 <sup>0</sup>	2.1×10 <sup>0</sup>
4	4.0×10 <sup>-1</sup>	1.1×10 <sup>0</sup>	4.6×10 <sup>-1</sup>	1.5×10 <sup>0</sup>	1.0×10 <sup>0</sup>	1.1×10 <sup>0</sup>	1.9×10 <sup>0</sup>	1.1×10 <sup>0</sup>	1.7×10 <sup>0</sup>	1.1×10 <sup>0</sup>
<b>Source organ : Lungs</b>										
Energy(MeV)	Skeleton	Heart	Bladder	Stomach	Spleen	Pancreas	Liver	Kidneys	Adrenal	Lungs
0.01	1.4×10 <sup>2</sup>	3.4×10 <sup>2</sup>	0.0	4.7×10 <sup>0</sup>	7.8×10 <sup>-1</sup>	0.0	6.6×10 <sup>1</sup>	3.5×10 <sup>1</sup>	0.0	1.8×10 <sup>3</sup>
0.015	1.1×10 <sup>2</sup>	2.4×10 <sup>2</sup>	3.0×10 <sup>-1</sup>	1.4×10 <sup>1</sup>	4.7×10 <sup>0</sup>	3.8×10 <sup>0</sup>	5.9×10 <sup>1</sup>	3.2×10 <sup>0</sup>	1.2×10 <sup>1</sup>	8.3×10 <sup>2</sup>
0.02	7.6×10 <sup>1</sup>	1.3×10 <sup>2</sup>	1.1×10 <sup>0</sup>	1.4×10 <sup>1</sup>	6.3×10 <sup>0</sup>	5.6×10 <sup>0</sup>	3.8×10 <sup>1</sup>	5.0×10 <sup>0</sup>	1.3×10 <sup>1</sup>	3.7×10 <sup>2</sup>
0.03	3.1×10 <sup>1</sup>	4.4×10 <sup>1</sup>	9.6×10 <sup>-1</sup>	6.4×10 <sup>0</sup>	3.4×10 <sup>0</sup>	3.2×10 <sup>0</sup>	1.4×10 <sup>1</sup>	2.9×10 <sup>0</sup>	0.0	1.1×10 <sup>2</sup>
0.05	7.9×10 <sup>0</sup>	1.3×10 <sup>1</sup>	4.1×10 <sup>-1</sup>	2.1×10 <sup>0</sup>	1.2×10 <sup>0</sup>	1.1×10 <sup>0</sup>	4.3×10 <sup>0</sup>	1.0×10 <sup>0</sup>	0.0	3.1×10 <sup>1</sup>
0.1	2.1×10 <sup>0</sup>	7.5×10 <sup>0</sup>	2.3×10 <sup>-1</sup>	1.2×10 <sup>0</sup>	7.0×10 <sup>-1</sup>	6.2×10 <sup>-1</sup>	2.5×10 <sup>0</sup>	6.0×10 <sup>-1</sup>	0.0	1.7×10 <sup>1</sup>
0.2	1.7×10 <sup>0</sup>	8.5×10 <sup>0</sup>	2.7×10 <sup>-1</sup>	1.3×10 <sup>0</sup>	8.0×10 <sup>-1</sup>	6.6×10 <sup>-1</sup>	2.8×10 <sup>0</sup>	6.6×10 <sup>-1</sup>	0.0	1.9×10 <sup>1</sup>
0.5	1.8×10 <sup>0</sup>	9.2×10 <sup>0</sup>	3.1×10 <sup>-1</sup>	1.5×10 <sup>0</sup>	8.6×10 <sup>-1</sup>	7.6×10 <sup>-1</sup>	3.1×10 <sup>0</sup>	7.5×10 <sup>-1</sup>	0.0	1.7×10 <sup>1</sup>
1	1.5×10 <sup>0</sup>	8.0×10 <sup>0</sup>	2.9×10 <sup>-1</sup>	1.4×10 <sup>0</sup>	8.1×10 <sup>-1</sup>	7.1×10 <sup>-1</sup>	2.8×10 <sup>0</sup>	6.8×10 <sup>-1</sup>	0.0	9.8×10 <sup>0</sup>
1.5	1.2×10 <sup>0</sup>	6.2×10 <sup>0</sup>	2.7×10 <sup>-1</sup>	1.3×10 <sup>0</sup>	7.7×10 <sup>-1</sup>	6.7×10 <sup>-1</sup>	2.4×10 <sup>0</sup>	6.3×10 <sup>-1</sup>	0.0	6.1×10 <sup>0</sup>
2	9.5×10 <sup>-1</sup>	4.6×10 <sup>0</sup>	2.5×10 <sup>-1</sup>	1.2×10 <sup>0</sup>	7.1×10 <sup>-1</sup>	6.4×10 <sup>-1</sup>	2.0×10 <sup>0</sup>	6.0×10 <sup>-1</sup>	1.1×10 <sup>0</sup>	4.1×10 <sup>0</sup>
4	4.8×10 <sup>-1</sup>	1.7×10 <sup>0</sup>	2.0×10 <sup>-1</sup>	7.6×10 <sup>-1</sup>	5.1×10 <sup>-1</sup>	5.2×10 <sup>-1</sup>	1.0×10 <sup>0</sup>	4.6×10 <sup>-1</sup>	8.1×10 <sup>-1</sup>	1.4×10 <sup>0</sup>

SAFs were set to zero when statistical uncertainty exceeds 5%.

**Table 2** Photon specific absorbed fractions (SAFs in 1/kg) in some organs of the Digimouse phantom (2).

<b>Source organ : Kidneys</b>										
Energy(MeV)	Skeleton	Heart	Bladder	Stomach	Spleen	Pancreas	Liver	Kidneys	Adrenal	Lungs
0.01	$7.0 \times 10^0$	0.0	$1.4 \times 10^0$	$2.2 \times 10^1$	$7.0 \times 10^1$	$2.5 \times 10^2$	$2.9 \times 10^1$	$1.1 \times 10^3$	$1.6 \times 10^2$	$3.8 \times 10^1$
0.015	$1.8 \times 10^1$	$1.6 \times 10^0$	$8.1 \times 10^0$	$3.7 \times 10^1$	$7.2 \times 10^1$	$1.9 \times 10^2$	$3.4 \times 10^1$	$5.9 \times 10^2$	$1.4 \times 10^2$	$3.6 \times 10^0$
0.02	$2.1 \times 10^1$	$3.2 \times 10^0$	$1.0 \times 10^1$	$2.9 \times 10^1$	$4.7 \times 10^1$	$1.1 \times 10^2$	$2.6 \times 10^1$	$2.9 \times 10^2$	$8.7 \times 10^1$	$5.6 \times 10^0$
0.03	$1.2 \times 10^1$	$2.2 \times 10^0$	$5.4 \times 10^0$	$1.2 \times 10^1$	$1.8 \times 10^1$	$3.7 \times 10^1$	$1.1 \times 10^1$	$9.1 \times 10^1$	$3.2 \times 10^1$	$3.2 \times 10^0$
0.05	$3.4 \times 10^0$	$7.8 \times 10^{-1}$	$1.8 \times 10^0$	$3.8 \times 10^0$	$5.3 \times 10^0$	$1.0 \times 10^1$	$3.4 \times 10^0$	$2.6 \times 10^1$	$9.3 \times 10^0$	$1.1 \times 10^0$
0.1	$9.3 \times 10^{-1}$	$4.5 \times 10^{-1}$	$1.1 \times 10^0$	$2.2 \times 10^0$	$3.1 \times 10^0$	$6.4 \times 10^0$	$2.0 \times 10^0$	$1.5 \times 10^1$	$5.4 \times 10^0$	$6.4 \times 10^{-1}$
0.2	$7.5 \times 10^{-1}$	$5.3 \times 10^{-1}$	$1.2 \times 10^0$	$2.5 \times 10^0$	$3.5 \times 10^0$	$7.2 \times 10^0$	$2.2 \times 10^0$	$1.8 \times 10^1$	$5.9 \times 10^0$	$6.5 \times 10^{-1}$
0.5	$7.8 \times 10^{-1}$	$5.8 \times 10^{-1}$	$1.3 \times 10^0$	$2.7 \times 10^0$	$3.9 \times 10^0$	$8.2 \times 10^0$	$2.4 \times 10^0$	$1.8 \times 10^1$	$7.1 \times 10^0$	$7.5 \times 10^{-1}$
1	$7.4 \times 10^{-1}$	$5.6 \times 10^{-1}$	$1.2 \times 10^0$	$2.6 \times 10^0$	$3.6 \times 10^0$	$7.0 \times 10^0$	$2.3 \times 10^0$	$1.4 \times 10^1$	$6.3 \times 10^0$	$7.0 \times 10^{-1}$
1.5	$6.7 \times 10^{-1}$	$4.9 \times 10^{-1}$	$1.1 \times 10^0$	$2.3 \times 10^0$	$3.2 \times 10^0$	$5.8 \times 10^0$	$2.0 \times 10^0$	$9.6 \times 10^0$	$5.3 \times 10^0$	$6.5 \times 10^{-1}$
2	$6.1 \times 10^{-1}$	$4.5 \times 10^{-1}$	$1.0 \times 10^0$	$2.1 \times 10^0$	$2.7 \times 10^0$	$4.6 \times 10^0$	$1.8 \times 10^0$	$6.8 \times 10^0$	$4.4 \times 10^0$	$6.0 \times 10^{-1}$
4	$3.9 \times 10^{-1}$	$3.7 \times 10^{-1}$	$7.9 \times 10^{-1}$	$1.2 \times 10^0$	$1.3 \times 10^0$	$1.9 \times 10^0$	$1.0 \times 10^0$	$2.7 \times 10^0$	$1.9 \times 10^0$	$4.7 \times 10^{-1}$
<b>Source organ : Spleen</b>										
Energy(MeV)	Skeleton	Heart	Bladder	Stomach	Spleen	Pancreas	Liver	Kidneys	Adrenal	Lungs
0.01	$8.1 \times 10^0$	$2.1 \times 10^{-1}$	0.0	$2.8 \times 10^2$	$2.8 \times 10^3$	$4.3 \times 10^2$	$1.8 \times 10^1$	$7.0 \times 10^1$	$1.1 \times 10^2$	$8.1 \times 10^1$
0.015	$1.4 \times 10^1$	$2.8 \times 10^0$	$2.3 \times 10^0$	$2.3 \times 10^2$	$1.4 \times 10^3$	$3.2 \times 10^2$	$2.7 \times 10^1$	$7.1 \times 10^1$	$9.8 \times 10^1$	$5.3 \times 10^0$
0.02	$1.5 \times 10^1$	$4.7 \times 10^0$	$4.3 \times 10^0$	$1.3 \times 10^2$	$6.3 \times 10^2$	$1.7 \times 10^2$	$2.2 \times 10^1$	$4.7 \times 10^1$	$6.3 \times 10^1$	$7.0 \times 10^0$
0.03	$8.9 \times 10^0$	$2.9 \times 10^0$	$2.9 \times 10^0$	$4.6 \times 10^1$	$1.9 \times 10^2$	$5.9 \times 10^1$	$9.4 \times 10^0$	$1.8 \times 10^1$	$2.2 \times 10^1$	$3.9 \times 10^0$
0.05	$2.6 \times 10^0$	$9.8 \times 10^{-1}$	$9.8 \times 10^{-1}$	$1.3 \times 10^1$	$5.5 \times 10^1$	$1.7 \times 10^1$	$3.0 \times 10^0$	$5.4 \times 10^0$	$6.7 \times 10^0$	$1.3 \times 10^0$
0.1	$7.1 \times 10^{-1}$	$6.1 \times 10^{-1}$	$5.9 \times 10^{-1}$	$8.0 \times 10^0$	$3.3 \times 10^1$	$1.0 \times 10^1$	$1.7 \times 10^0$	$3.2 \times 10^0$	$3.8 \times 10^0$	$7.1 \times 10^{-1}$
0.2	$5.9 \times 10^{-1}$	$6.8 \times 10^{-1}$	$6.6 \times 10^{-1}$	$9.1 \times 10^0$	$3.8 \times 10^1$	$1.1 \times 10^1$	$1.9 \times 10^0$	$3.6 \times 10^0$	$4.6 \times 10^0$	$7.9 \times 10^{-1}$
0.5	$6.3 \times 10^{-1}$	$7.6 \times 10^{-1}$	$7.3 \times 10^{-1}$	$1.0 \times 10^1$	$3.7 \times 10^1$	$1.2 \times 10^1$	$2.1 \times 10^0$	$3.9 \times 10^0$	$4.6 \times 10^0$	$9.0 \times 10^{-1}$
1	$5.8 \times 10^{-1}$	$7.0 \times 10^{-1}$	$6.9 \times 10^{-1}$	$9.2 \times 10^0$	$2.5 \times 10^1$	$1.1 \times 10^1$	$2.0 \times 10^0$	$3.7 \times 10^0$	$4.7 \times 10^0$	$8.2 \times 10^{-1}$
1.5	$5.2 \times 10^{-1}$	$6.8 \times 10^{-1}$	$6.1 \times 10^{-1}$	$7.7 \times 10^0$	$1.6 \times 10^1$	$9.0 \times 10^0$	$1.8 \times 10^0$	$3.2 \times 10^0$	$4.0 \times 10^0$	$7.5 \times 10^{-1}$
2	$4.7 \times 10^{-1}$	$6.4 \times 10^{-1}$	$5.8 \times 10^{-1}$	$6.1 \times 10^0$	$1.1 \times 10^1$	$6.8 \times 10^0$	$1.6 \times 10^0$	$2.7 \times 10^0$	$3.3 \times 10^0$	$7.3 \times 10^{-1}$
4	$3.2 \times 10^{-1}$	$4.8 \times 10^{-1}$	$4.7 \times 10^{-1}$	$2.5 \times 10^0$	$3.9 \times 10^0$	$2.7 \times 10^0$	$9.9 \times 10^{-1}$	$1.4 \times 10^0$	$1.5 \times 10^0$	$5.6 \times 10^{-1}$
<b>Source organ : Bladder</b>										
Energy(MeV)	Skeleton	Heart	Bladder	Stomach	Spleen	Pancreas	Liver	Kidneys	Adrenal	Lungs
0.01	$4.7 \times 10^0$	0.0	$2.7 \times 10^3$	0.0	0.0	0.0	$2.8 \times 10^{-1}$	$1.3 \times 10^0$	0.0	0.0
0.015	$1.8 \times 10^1$	$2.4 \times 10^{-1}$	$1.5 \times 10^3$	$2.1 \times 10^0$	$2.3 \times 10^0$	$4.4 \times 10^0$	$2.7 \times 10^0$	$8.2 \times 10^0$	0.0	$3.4 \times 10^{-1}$
0.02	$2.2 \times 10^1$	$8.9 \times 10^{-1}$	$6.9 \times 10^2$	$4.0 \times 10^0$	$4.3 \times 10^0$	$7.0 \times 10^0$	$4.5 \times 10^0$	$1.0 \times 10^1$	0.0	$1.2 \times 10^0$
0.03	$1.3 \times 10^1$	$8.6 \times 10^{-1}$	$2.1 \times 10^2$	$2.7 \times 10^0$	$2.9 \times 10^0$	$4.0 \times 10^0$	$2.8 \times 10^0$	$5.4 \times 10^0$	0.0	$1.1 \times 10^0$
0.05	$3.6 \times 10^0$	$3.4 \times 10^{-1}$	$6.0 \times 10^1$	$9.2 \times 10^{-1}$	$1.0 \times 10^0$	$1.4 \times 10^0$	$9.8 \times 10^{-1}$	$1.8 \times 10^0$	0.0	$4.4 \times 10^{-1}$
0.1	$9.6 \times 10^{-1}$	$2.2 \times 10^{-1}$	$3.6 \times 10^1$	$5.5 \times 10^{-1}$	$5.6 \times 10^{-1}$	$8.2 \times 10^{-1}$	$5.8 \times 10^{-1}$	$1.0 \times 10^0$	0.0	$2.4 \times 10^{-1}$
0.2	$7.8 \times 10^{-1}$	$2.5 \times 10^{-1}$	$4.1 \times 10^1$	$6.3 \times 10^{-1}$	$6.5 \times 10^{-1}$	$8.7 \times 10^{-1}$	$6.5 \times 10^{-1}$	$1.2 \times 10^0$	0.0	$2.6 \times 10^{-1}$
0.5	$8.1 \times 10^{-1}$	$2.9 \times 10^{-1}$	$4.2 \times 10^1$	$6.8 \times 10^{-1}$	$7.3 \times 10^{-1}$	$9.6 \times 10^{-1}$	$7.2 \times 10^{-1}$	$1.3 \times 10^0$	0.0	$3.1 \times 10^{-1}$
1	$7.6 \times 10^{-1}$	$2.9 \times 10^{-1}$	$3.1 \times 10^1$	$6.5 \times 10^{-1}$	$6.8 \times 10^{-1}$	$9.9 \times 10^{-1}$	$6.8 \times 10^{-1}$	$1.2 \times 10^0$	0.0	$2.9 \times 10^{-1}$
1.5	$6.9 \times 10^{-1}$	$2.5 \times 10^{-1}$	$2.1 \times 10^1$	$6.0 \times 10^{-1}$	$6.2 \times 10^{-1}$	$8.6 \times 10^{-1}$	$6.2 \times 10^{-1}$	$1.1 \times 10^0$	0.0	$2.7 \times 10^{-1}$
2	$6.4 \times 10^{-1}$	$2.5 \times 10^{-1}$	$1.4 \times 10^1$	$5.5 \times 10^{-1}$	$5.7 \times 10^{-1}$	$8.1 \times 10^{-1}$	$5.8 \times 10^{-1}$	$1.0 \times 10^0$	0.0	$2.5 \times 10^{-1}$
4	$4.2 \times 10^{-1}$	$1.9 \times 10^{-1}$	$4.8 \times 10^0$	$4.5 \times 10^{-1}$	$4.7 \times 10^{-1}$	$6.4 \times 10^{-1}$	$4.5 \times 10^{-1}$	$7.7 \times 10^{-1}$	$5.1 \times 10^{-1}$	$2.0 \times 10^{-1}$

SAFs were set to zero when statistical uncertainty exceeds 5%.

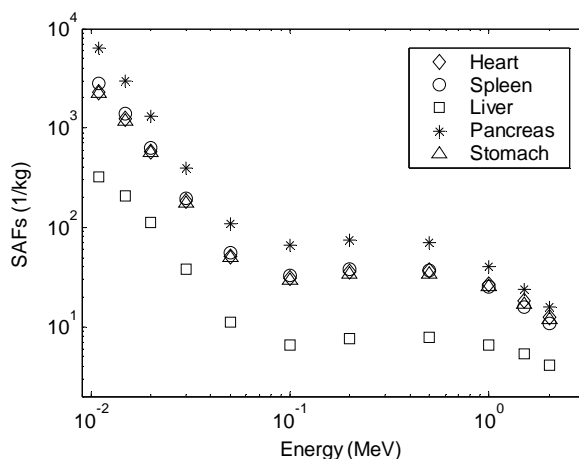


**Figure 1.** Photon specific absorbed fractions for self-irradiation in organs of the Digimouse phantom.

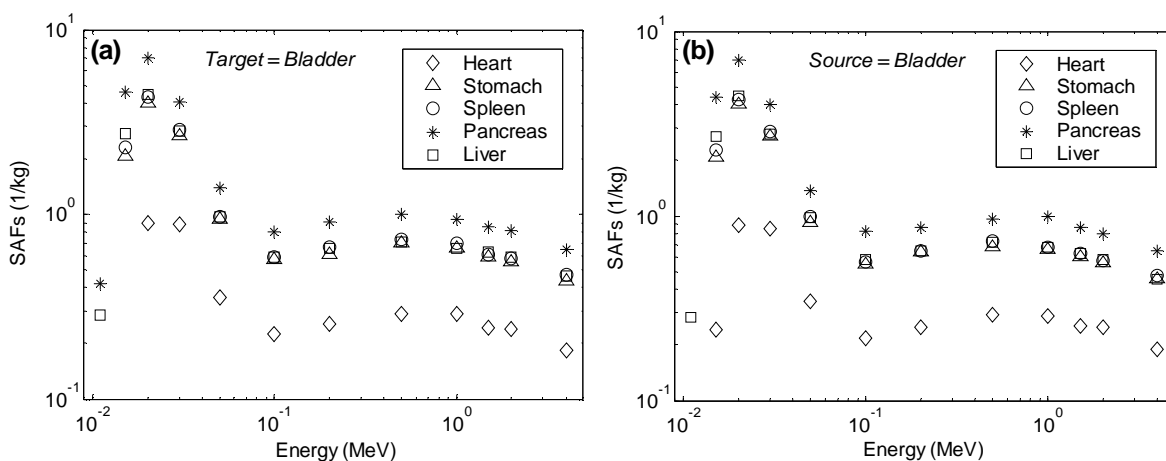


**Figure 2.** Comparison of photon specific absorbed fractions (SAFs) for cross-irradiation in organs of the Digimouse for (a) source=heart, stomach, spleen, pancreas or liver and target=bladder (b) source=bladder and target= heart, stomach, spleen, pancreas and liver.

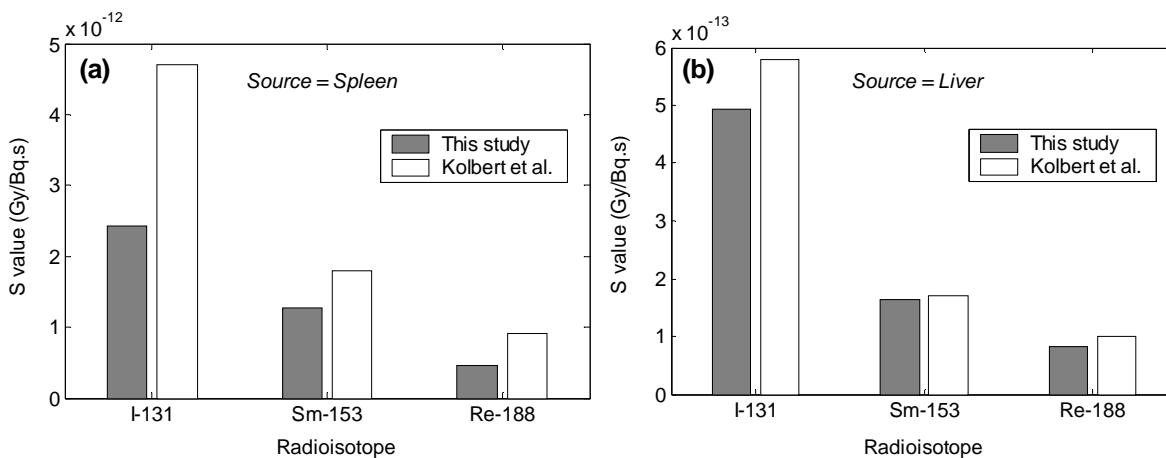


**Figure 3.** Comparison of photon-only S values for self-irradiation for  $^{131}\text{I}$ ,  $^{153}\text{Sm}$  and  $^{188}\text{Re}$  in this study with Kolbert *et al.*<sup>2)</sup> study for (a) source=liver and (b) source=spleen.

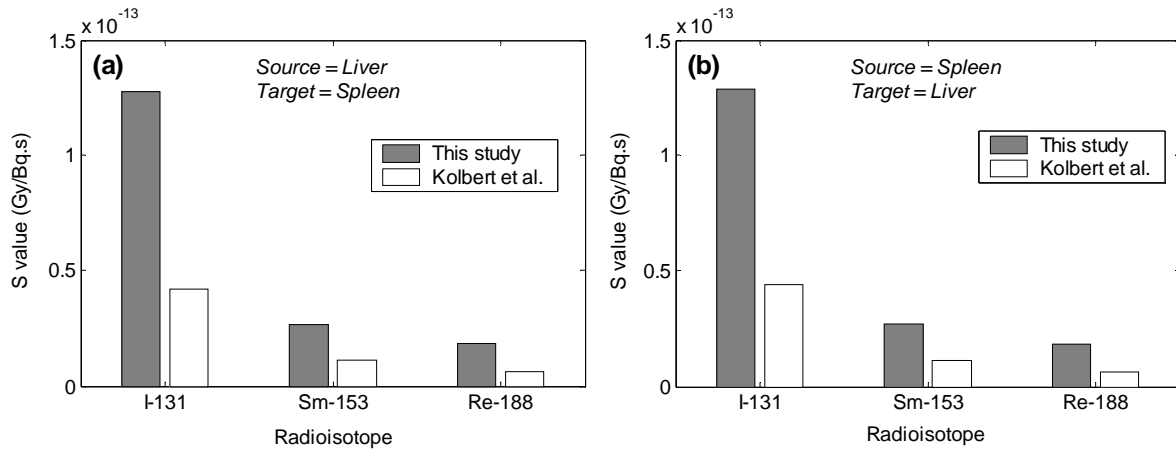


**Figure 4.** Comparison of photon-only S values for cross-irradiation for  $^{131}\text{I}$ ,  $^{153}\text{Sm}$  and  $^{188}\text{Re}$  in the present study with Kolbert *et al.*<sup>2)</sup> study for (a) Source=liver and target=spleen. (b) source=spleen and target=liver.

# EVALUATION OF COUNTING EFFICIENCIES OF A WHOLE-BODY COUNTER CONSIDERING THE ICRP BIOKINETIC MODELS

M. Takahashi<sup>1</sup>, S. Kinase<sup>1</sup> and R. Kramer<sup>2</sup>

<sup>1</sup>*Japan Atomic Energy Agency, 2-4 Shirakata-Shirane, Tokai-mura, Ibaraki 319-1195, Japan*

<sup>2</sup>*Universidade Federal de Pernambuco, Av. Prof. Luiz Freire 1000, Cidade Universitaria, CEP 50740-540, Recife, PE, Brazil*

## Abstract

Counting efficiencies of a whole-body counter (WBC), which has been installed at the Japan Atomic Energy Agency (JAEA), have been evaluated for  $^{137}\text{Cs}$  and  $^{60}\text{Co}$  within a voxel phantom. The distributions of the radionuclides were estimated from the ICRP biokinetic models. The evaluated efficiencies were compared with those for whole-body radionuclide distributions in the voxel phantom in order to study the impact of radionuclide distributions on the counting efficiency evaluations. Consequently, it was found that the efficiencies for  $^{137}\text{Cs}$  and  $^{60}\text{Co}$  with various distributions have minima at 0.5 days after intake. The efficiencies lead to 20 % ( $^{137}\text{Cs}$ ) and 30 % ( $^{60}\text{Co}$ ) underestimations of activity in comparison with those for the whole-body distributions.

## 1 Introduction

The International Commission on Radiation Units and Measurements (ICRU) mentions that the acceptable errors for direct measurements with whole-body counters (WBCs) will be less than  $\pm 50\%$  [1]. The measurements require adequate knowledge of calibrations for the WBCs, such as selections of human surrogates (phantoms) and radioactive source distributions in the human subjects. In particular, the knowledge and its applications are needed for rapid and accurate measurements following an accident. At the Japan Atomic Energy Agency (JAEA), there have been several attempts on the use of voxel phantoms that provide three-dimensional representations of the human bodies in calibrations for a WBC [2, 3]. Monte Carlo simulations with the voxel phantoms have been applied to the calibrations. The purpose of this work is to evaluate counting efficiencies of the WBC considering radioactive source distributions in the voxel phantom for development of a more reliable calibration method for the WBC. Inhaled  $^{137}\text{Cs}$  and  $^{60}\text{Co}$  were considered as the sources since these nuclides are important for radiation protection in typical nuclear facilities.

## 2 Materials and methods

### 2.1 Whole body counter(WBC)

A bed-type WBC, which has three p-type high-purity Ge closed-ended coaxial detectors, has been installed at JAEA. The Ge detectors have approximately 80 % peak efficiencies related to that of a 76.2 mm diameter  $\times$  76.2 mm thick NaI(Tl) crystal. A bed and the Ge detectors are located in a shielding room, of which inner size is 2.0 m width  $\times$  2.5 m distance  $\times$  2.5 m height, to reduce background radiations. The schematic illustrations of the WBC and the Ge detector are shown in

figure 1. The first Ge detector is placed under the thyroid of measured humans at a distance of 30 cm from the bed surface. Second one is at the opposite side of the legs of the humans at 120 cm from the first detector. Last one is in the middle position between the other two detectors above 50 cm from the bed surface. The positions of detectors were determined so that the total counting efficiency is roughly constant along the midline of a measured human.

## 2.2 Voxel phantom

MAX06 voxel phantom was used. The MAX06 was developed by Kramer *et al.* [4] as the first human phantom which corresponds to the male anatomical data recommended in ICRP publication [5]. Figure 2 shows the images of the MAX06 of (a) entire body and (b) cross sectional slice. The MAX06 has been compiled as a data set of 474 columns  $\times$  222 rows  $\times$  1461 slices and consequently the total number of voxels are 153,738,108, of which 41,461,410 voxels are filled with human tissues. The voxel size is  $1.2 \times 1.2 \times 1.2$  mm<sup>3</sup>. Around 90 organ and tissue regions have been specified and it allows to assume variety source distributions in the phantom.

## 2.3 Biokinetic model

Distributions of <sup>137</sup>Cs and <sup>60</sup>Co in a human body were estimated using the ICRP biokinetic models [6, 7]. The models are presented as a compartment model, in which transfer of radiological materials are expressed by first-order kinetics as a following equation.

$$\frac{dq_i}{dt} = \sum_j \lambda_{j \rightarrow i} q_j - \lambda_i q_i - \lambda_p q_i \quad (1)$$

where  $q_i, q_j$  are activities of i- and j-th compartments,  $\lambda_i$  is a transfer coefficient outward from i-th compartment,  $\lambda_{j \rightarrow i}$  is a transfer coefficient from j-th to i-th compartment and  $\lambda_p$  is a decay constant of the nuclide.

In figure 3, the biokinetic models of <sup>137</sup>Cs and <sup>60</sup>Co are shown. The radionuclides are deposited in the respiratory organs by inhalation and then absorbed into blood and moved to some organs with specific rates of the materials. The source distributions vary with time. The equations for each compartment of the models were calculated to obtain the source distributions at given days after an intake by inhalation.

## 2.4 Monte Carlo calculations

Counting efficiencies of the WBC were evaluated with the EGS4 code [8] in conjunction with UCWBC code [2]. The photon source organs of the MAX06 and emission fractions were assumed to be the source distributions derived from the biokinetic models. Photon energies of 662 keV (<sup>137</sup>Cs) and 1333 keV (<sup>60</sup>Co) were simulated. The MAX06 was assumed to be on the bed at the same position with humans in actual measurements. The counting efficiencies were evaluated by dividing the sum of total absorption peaks of the three Ge detectors by the number of histories. The number of histories was set 10 millions so that statistical uncertainties were below 3 %. The cross section data for photons were taken from PHOTX [9], and for electrons from ICRU report 37 [10].

# 3 Results and discussion

## 3.1 Source distributions

Table 1 shows the fractions of activity in the source organs for <sup>137</sup>Cs and <sup>60</sup>Co at 0.5, 3, 10 and 365 days after an intake. At 0.5 days, the nasal passage is one of the main source organs for both

nuclides because it is the entrance of the inhaled materials.

It can be also seen in table 1 that the distributions of  $^{60}\text{Co}$  are different from homogeneity over the period of a year. The nasal passage and the colon are dominant source organs at 0.5 and 3 days. Following removal of the activities from these organs, the lungs become a significant source organ. On the other hand,  $^{137}\text{Cs}$  is almost homogeneously distributed in the whole body because of rapid absorption into blood and circulation to the whole body. These fractions of activity were assigned into the MAX06 for the simulations. Figure 4 illustrates the source distributions on frontal view of the MAX06.

### 3.2 Counting efficiency

Figure 5 shows the counting efficiencies of the WBC for  $^{137}\text{Cs}$  and  $^{60}\text{Co}$  with various source distributions. For both nuclides, the efficiencies at 0.5 days after an intake are the lowest and the discrepancies with those for the homogeneous sources are approximately 20 % and 30 % for  $^{137}\text{Cs}$  and  $^{60}\text{Co}$ , respectively. This is due to the retention of the activity in the nasal passage, which is at relatively large distance from the detectors. The results indicate that measurements with the WBC following intakes by inhalation of  $^{60}\text{Co}$  and  $^{137}\text{Cs}$  can lead to underestimations of the body activity.

For  $^{137}\text{Cs}$ , the counting efficiency at 3 days after an intake is consistent with that for the homogeneous source. It is due to the rapid circulation of Cs to the whole body. The efficiency for  $^{60}\text{Co}$  at 3 days after an intake is inconsistent with that for the homogeneous source. This means that the activities in the other organs than the nasal passage only slightly affected the efficiency of the WBC.

## 4 Conclusions

The counting efficiencies of the WBC at JAEA for  $^{137}\text{Cs}$  and  $^{60}\text{Co}$  were evaluated using the voxel phantom and the ICRP biokinetic models. The fractions of the radionuclides in the organs at 0.5, 3, 10 and 365 days after an intake were estimated. It was found that the efficiencies at 0.5 days after an intake are the lowest for both radionuclides. The differences of the counting efficiencies between that for the specific source distributions at 0.5 days after an intake and that for the homogeneous source distribution are 20 % and 30 % for  $^{137}\text{Cs}$  and  $^{60}\text{Co}$ , respectively. The results show that the calibration of the WBC taking into account the biokinetic models may be necessary for measurements following an accident.

## References

- [1] ICRU, "Direct Determination of the Body Content of Radionuclides", ICRU Report 69, Bethesda, MD, (2003).
- [2] S. Kinase, S. Takagi, H. Noguchi and K. Saito, "Application of Voxel Phantoms and Monte Carlo Method to Whole-body Counter Calibration", *Radiat. Prot. Dosim.*, 125, 189-193(2007).
- [3] M. Takahashi, S. Kinase and R. Kramer, "Evaluation of Counting Efficiency of Whole-body Counter Using "MAX06" Voxel Phantom", *KEK Proceedings*, 2008-7, 34-40(2008).
- [4] R. Kramer, H. J. Khoury, J. W. Vieira and V. J. M. Lima, "MAX06 and FAX06: update of two adult human phantoms for radiation protection dosimetry", *Phys. Med. Biol.*, **51**, 3331-3346(2006).
- [5] ICRP, "Basic Anatomical and Physical Data for Use in Radiological Protection: Reference Values", ICRP Publ. 89, Pergamon Press, Oxford(2002).

- [6] ICRP, "Age-dependent Doses to Members of the Public from Intake of Radionuclides: Part 1", ICRP Publ. 56, Pergamon(1989).
- [7] ICRP, "Age-dependent Dose to Members of the Public from Intake of Radionuclides: Part 2 Ingestion Dose Coefficients", ICRP Publ. 67, Pergamon(1993).
- [8] W. R. Nelson, H. Hirayama and D. W. O. Rogers, "The EGS4 Code System", SLAC-265 (1985).
- [9] RSIC, DLC-136/PHOTX Photon Interaction Cross Section Library (contributed by National Institute of Standards and Technology)(1989).
- [10] ICRU, "Stopping Powers for Electrons and Positrons", ICRU Report 37, Bethesda, Md, (1984).

Table 1: Fractions of activity in the specified source organs.

Elapsed days from intake	$^{137}\text{Cs}$				$^{60}\text{Co}$			
	0.5	3	10	365	0.5	3	10	365
Whole body (blood)	68	96	100	100	8	18	27	60
Nasal passage	32	4			32	11		
Lungs					9	36	69	33
Small intestine					3			
Colon					48	33	1	
Liver						2	3	7

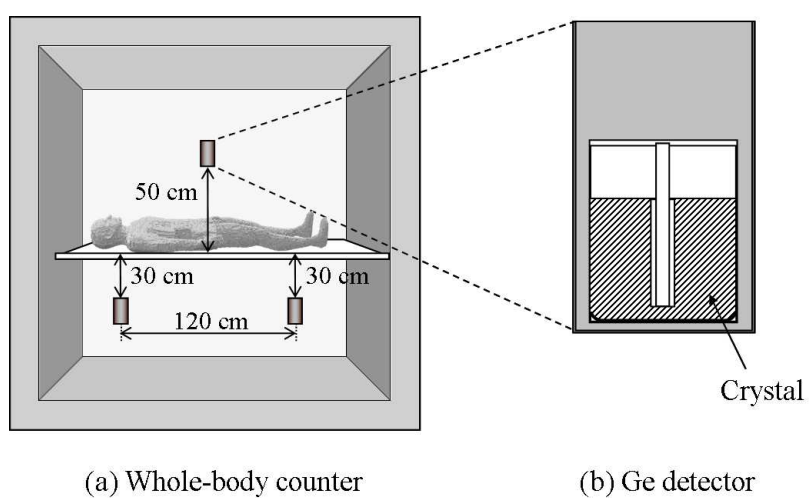


Figure 1: Geometrical models of the whole-body counter and the Ge detector.

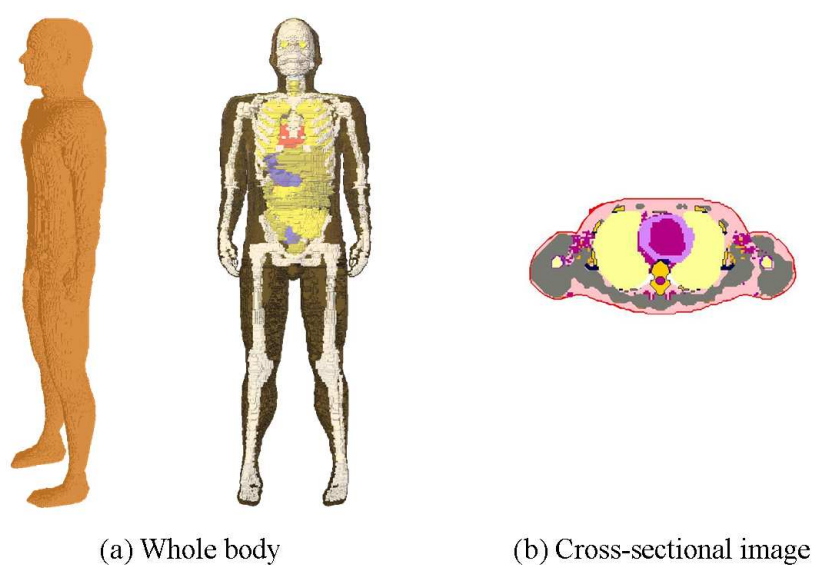


Figure 2: MAX06 phantom.



# Evaluation of LSO scintillator characteristics for development of lost alpha particle-induced gamma ray detector system in ITER

S. Kashiwa<sup>1</sup>, M. Nishiura<sup>2</sup>, T. Tanaka<sup>1</sup>, T. Nagasaka<sup>1</sup>,  
K. Fujioka<sup>3</sup>, A. Okamoto<sup>1</sup>, S. Kitajima<sup>1</sup>, M. Sasao<sup>1</sup>

<sup>1</sup>*Department of Quantum Science and Energy Engineering,  
Tohoku University Graduate School of Engineering, Miyagi 980-8579, Japan*

<sup>2</sup>*National Institute for Fusion Science, Gifu 509-5292, Japan*

<sup>3</sup>*Institute of Laser engineering, Osaka University, Osaka 565-0871, Japan*

*e-mail: soichiro.kashiwa@ppl2.qse.tohoku.ac.jp*

## Abstract

A lost alpha particle-induced gamma ray detector system is now under development for application to ITER. The Ce:LSO scintillator is considered an attractive candidate detector and its characteristics were studied. To evaluate the potential of this system, the pulse height distribution of 4.44 MeV gamma rays resulting from an Am-Be source was measured, and results obtained by experiment and EGS4 simulation was compared. In addition, the transmittance of Ce:LSO was measured to evaluate the effects of self-absorption.

## 1. Introduction

Alpha particle diagnostics is important for understanding particle behaviors outside and inside fusion plasmas. Alpha particle confinement and loss are dependent on the performance of thermonuclear reactors. Therefore, scintillator lost ion probes have been widely used in existing devices, such as LHD, NSTX, and ASDEX-UG. For ITER, a similar system has been designed and various components have been developed. In burning plasma experiments such as ITER, various nuclear reactions are expected due to the energetic particles originating from DT/DD reactions. Kiptily *et al.* first proposed the concept of detection using 4.44 MeV gamma ray emission produced by the nuclear reaction  ${}^9\text{Be}(\alpha, n\gamma){}^{12}\text{C}$  between lost alpha particles and beryllium first walls of ITER [1]. The advantages of this system are that the hardware installation is flexible and the distributions of lost alpha particles are measurable.

For this purpose, the scintillators should have a sufficient time response, energy resolution, and sensitivity for gamma rays. In addition, scintillators require adequate light output maintained at high temperature of  $\sim 600$  K and low sensitivity to neutrons.

In view of these requirements, LSO was selected as a promising scintillator for 4.44 MeV gamma rays detection. Here, the pulse distribution of the 4.44 MeV gamma rays produced in  ${}^9\text{Be}(\alpha, n\gamma){}^{12}\text{C}$  from an Am-Be source and energy resolution at 4.44 MeV were studied. In addition, the pulse height distribution of 4.44 MeV gamma rays was calculated by EGS4. Moreover, the transmittance of Ce:LSO was measured and self-absorption was studied.

## 2. Experimental setups, conditions, and simulation conditions

### 2.1 Measurement of pulse height distributions of 4.44 MeV gamma rays from Am-Be source

An experiment was performed involving irradiation of the Ce:LSO scintillator with 4.44 MeV gamma rays from an Am-Be source. The experimental setup is shown in Fig. 1. Ce:LSO is wrapped with Teflon tape and coupled by optical grease (ORTEC 6262A) to the glass window of a photomultiplier tube. The detector anode signal is sent through AMP to MCA. The distance between source and scintillator is 5 cm. Thus, Ce:LSO was unshielded, and placed under conditions

of gamma rays flux at about  $143 \text{ cm}^{-2}\text{s}^{-1}$ .

## 2.2 Conditions and geometry of Am-Be experiment and simulation

In the system design for ITER, the LSO scintillator size is important, because the detector installed in the port plug is irradiated with fast neutrons. This causes noise and thus reduces the signal to noise ratio. Therefore, neutron sensitivity must be reduced by optimization of scintillator thickness or volume in addition to the selection of a low sensitivity scintillator material. Given these problems, EGS4 is considered a useful tool for the design of suitable scintillator size for installing in ITER. EGS4 results provide the pulse height distribution of gamma rays, and it is therefore possible to determine the scintillator size required by calculating EGS4. First, a comparison between experiment and calculation with regard to the pulse height distribution was carried out.

Calculation conditions were as follows. In the simulation, Ce:LSO material data was made without Ce doping. Thus, the scintillator was composed of lutetium, silicon, and oxygen only at elemental ratios of 2, 1, and 5, respectively. The density was  $7.4 \text{ g/cm}^3$ . The energies of gamma rays emitted from the source were 4.44 and 3.21 MeV with an emission ratio of 89:11 calculated from the cross-section of  ${}^9\text{Be}(\alpha, n\gamma){}^{12}\text{C}$  [2]. The emission was in the  $2\pi$  direction. The distance between the source and scintillator was 5 cm, which was the same as in the experiment. The source was defined as a point source. In addition, the convolution operation was carried out on EGS4 results to reflect device resolution. The standard deviation of each channel was determined as the relationship between energy resolution and absorbed gamma ray energy.

## 2.3 Calculation of full energy peak fraction regarding Ce:LSO

The effective scintillator size was estimated by calculating the full energy peak fraction as effective size index by EGS4. The conditions of the calculations were as follows. Scintillator material data were as explained above. The evaluation was carried out to study the full energy peak fraction changes with changes in thickness or the area of incidence plane.

## 2.4 Transmittance of Ce:LSO

The study of self-absorption in crystals is important, because larger scintillator size is associated with lower transmittance due to the increase in its self-absorption. To study this value, the Ce:LSO emission spectrum was measured. In this experiment, a Xe lamp was used to excite the scintillator.

In addition, a short pass filter was placed between the light source and scintillator to allow only UV to pass through and excite the scintillator. The transmittance of Ce:LSO was measured using a spectrophotometer (Hitachi U-4100).

# 3. Results and Discussion

## 3.1 Measurement of pulse height distributions of 4.44 MeV gamma rays from Am-Be source

Figure 2 shows the pulse height distribution of 4.44 MeV gamma rays produced in  ${}^9\text{Be}(\alpha, n\gamma){}^{12}\text{C}$  reaction from the Am-Be source. Note an energy resolution of 7% was obtained at full energy peak. In addition, three more peaks were confirmed. From the higher channel, they were a 4.44 MeV single escape peak, 4.44 MeV double escape peak, and 3.21 MeV single escape peak. As the Am-Be source produces another 3.21 MeV energy gamma rays in  ${}^9\text{Be}(\alpha, n\gamma){}^{12}\text{C}$  in addition to 4.44 MeV, the linear relation between absorbed gamma ray energy and light output was studied. Figure 3 shows the pulse height distribution of 0.662 MeV, 1.17 MeV, and 1.33 MeV from  ${}^{137}\text{Cs}$  and  ${}^{60}\text{Co}$ . Note the three peaks in the pulse height of  ${}^{60}\text{Co}$ . The highest channel peak is the sum peak. The relation was obtained based on these results. As shown in Fig. 4, the results confirmed a linear relation between gamma ray energy and light output from 0.662 MeV to 4.44 MeV. Therefore, Ce:LSO was expected to be able to discriminate 4.44 MeV gamma rays from any other gamma rays.

## 3.2 Am-Be experiment and simulation

Figures 5 and 6 show a comparison of the experimental and simulation results. These results indicated good agreement in peak shapes and the ratio of full energy peak to the other two peaks in the simulation

by EGS4.

### 3.3 Calculation of full energy peak fraction regarding Ce:LSO

Figure 7 shows the transition of the full energy peak fraction of LSO with changes in thickness. The full energy peak fraction showed saturation above ~4 cm. Full energy peak fraction is defined as the ratio of the full energy peak to the total reaction. This would be a useful index to estimate effective thickness and volume to detect 4.44 MeV gamma rays. This study allows lowering of the neutron reaction rate. The estimation of full energy peak fraction by EGS4 simulation indicated that the effective thickness is about 4 cm. This value is the same as 4.44 MeV gamma rays of attenuation lengths of LSO.

### 3.4 Transmittance of Ce:LSO

The emission spectrum of Ce:LSO excited by a Xe lamp is shown in Figure 8. The transmittance of Ce:LSO is shown in Figure 9. It indicates that the wavelength center is about 420 nm. Given this result, the transmittance of Ce:LSO at 420 nm was studied and it was shown to be about 84%. Here, the effects of self-absorption were studied using Fresnel's law, which provides the reflection rate on the surface of the scintillator. For simplicity, it is assumed that self-absorption does not occur inside the scintillator. Taking into account multiple bounces between the two end surfaces (the scintillator and air), the theoretical transmittance without self-absorption is obtained. This ideal transmittance is about 84%, which is equivalent to the transmittance of Ce:LSO obtained in the experiment. These results indicated that self-absorption inside Ce:LSO could be ignored over the range of thickness of 20 mm.

## 4. Conclusions

The results presented in this paper indicated that Ce:LSO is expected to be available as a 4.44 MeV gamma ray detector in ITER. In addition, the peak shape in EGS4 simulation showed good agreement with the experimental results. Therefore, it is expected to be possible to design a suitable scintillator size for detecting 4.44 MeV gamma rays by EGS4. Moreover, EGS4 simulation provides the effective volume of the LSO scintillator by calculating the full energy peak fraction with changes in volume. The comparison of the measured transmittance of Ce:LSO and evaluation of transmittance without self-absorption according to Fresnel's law showed that self-absorption can be ignored for Ce:LSO. Given this result and those of EGS4 simulation, Ce:LSO can be enlarged to the effective thickness indicated by EGS4 calculation. However, it is necessary to further study the characteristics of Ce:LSO, especially the neutron sensitivity as neutrons cause noise pulses and neutron fluxes are expected where the detector is mounted.

## References

- 1) V. G. Kiptily, Joint Meeting of ITPA NWG and Diagnostic Workshop (2007)
- 2) K.W.Geiger,L.Van Der Zwan R,NRCC-15303,197605

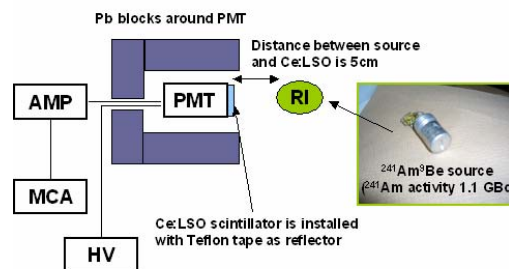


Figure 1: Am-Be experimental setup

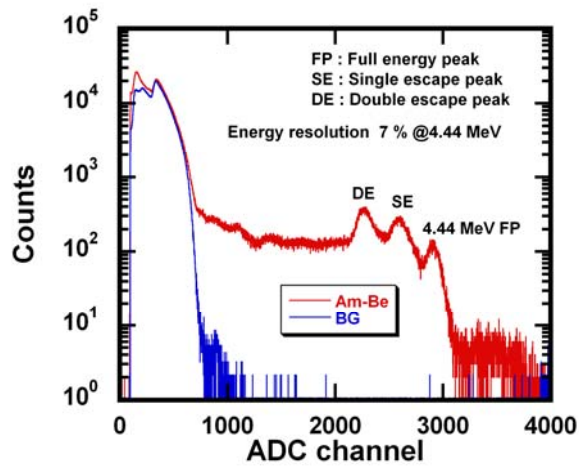


Figure 2: The pulse height distribution of 4.44 MeV gamma rays

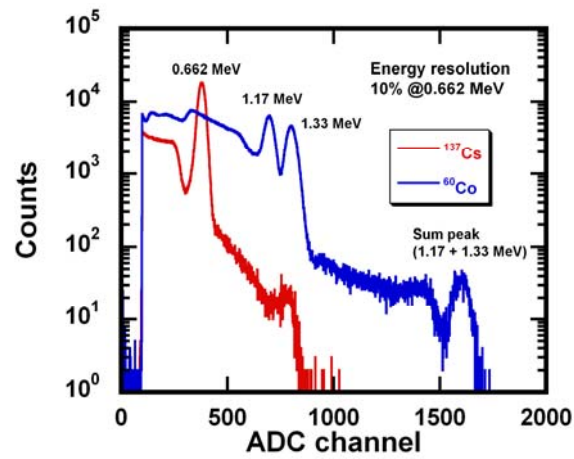


Figure 3: Pulse height distributions of 0.662, 1.17, and 1.33 MeV gamma rays

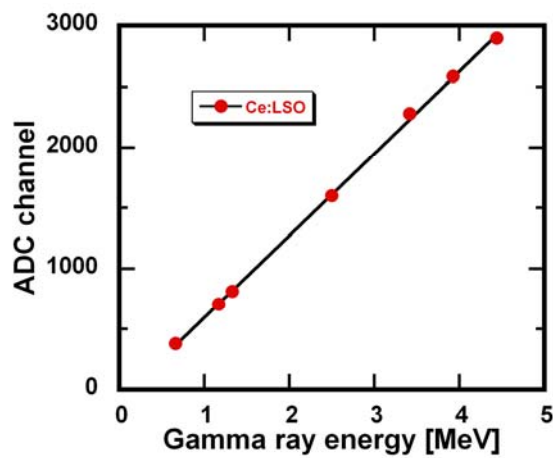


Figure 4: Relationship between pulse height and absorbed gamma ray energy

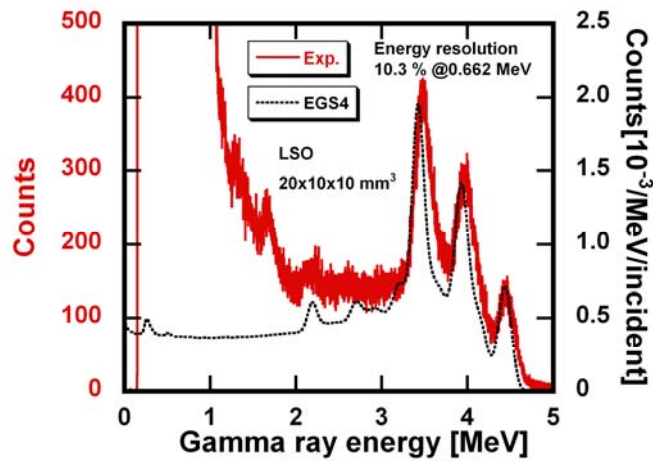


Figure 5: Comparison of Am-Be source experiment and EGS4 simulation (scintillator volume:  $20 \times 10 \times 10 \text{ mm}^3$ )

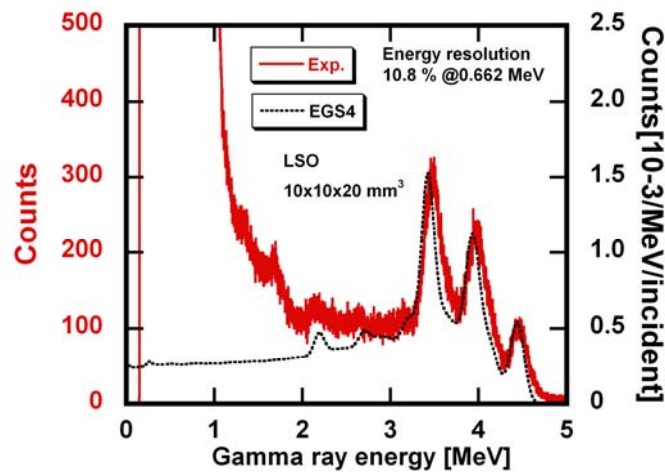


Figure 6: Comparison of Am-Be source experiment and EGS4 simulation (scintillator volume:  $10 \times 10 \times 20 \text{ mm}^3$ )

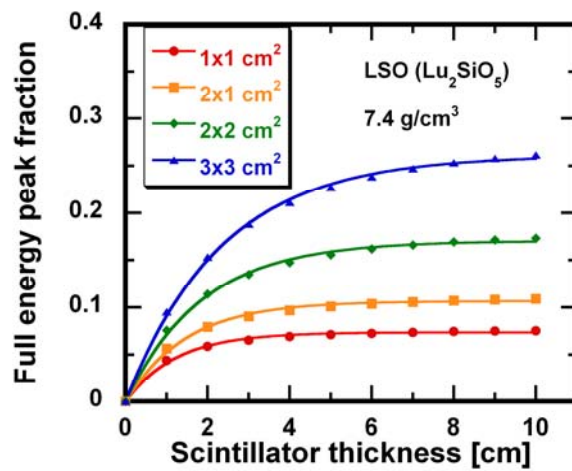


Figure 7: Full energy peak fraction of LSO with volume change

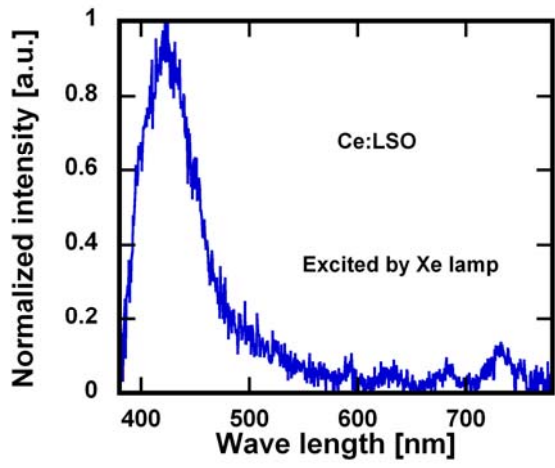


Figure 8: Emission of Ce:LSO with Xe lamp excitation

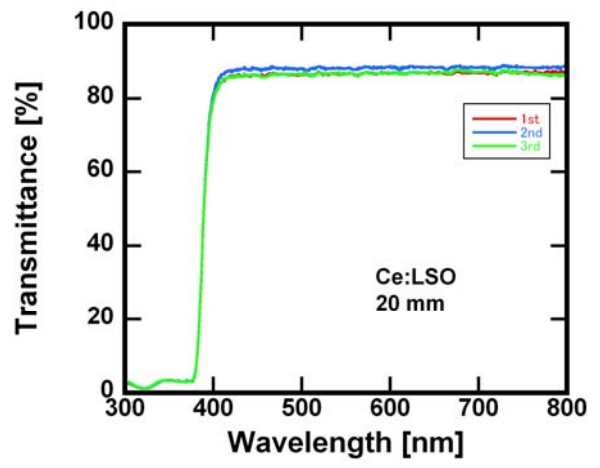


Figure 9: Transmittance of Ce:LSO

# EVALUATION OF DELTA-RAYS PRODUCTION IN A WALL-LESS TISSUE EQUIVALENT PROPORTIONAL COUNTER IRRADIATED BY ENERGETIC HEAVY ION BEAMS

S. Tsuda<sup>1,3</sup>, T. Sato<sup>1</sup>, H. Iwase<sup>2,3</sup>, Y. Namito<sup>2,3</sup>, and S. Sasaki<sup>2,3</sup>

<sup>1</sup> *Research Group of Radiation Protection, Japan Atomic Energy Agency,  
Ibaraki 319-1195, Japan*

<sup>2</sup> *Radiation Science Center, High Energy Accelerator Research Organization,  
Ibaraki 305-0801, JAPAN*

<sup>3</sup> *School of High Energy Accelerator Science, The Graduate University for Advanced Studies (Sokendai)  
Kanagawa 240-0193, Japan*

*e-mail: tsuda.shuichi@jaea.go.jp*

## Abstract

Energy deposits in a wall-less tissue equivalent proportional counter irradiated by 290 MeV/u carbon ion beams were obtained using EGS5 by modeling the delta-rays production along with the beam path. It is found that the delta-rays produced in a wall-less TEPC along with the carbon beams deposit energies in wide  $y$  region.

## 1. Introduction

Cancer therapy using energetic particles such as proton and carbon has recently become popular as one of the medical treatments for cancers. Energetic carbon beams can reach inside of human body and deposit energies effectively in a targeted tissue. It is important to know precise energy deposit distributions along with the beam in tissue for the purpose of strict evaluation of the dose by the energetic carbon ions.

In microdosimetry for heavy ion beams, tissue equivalent proportional counters, TEPCs, are widely used. A conventional TEPC has a detection volume filled with a gas surrounded by a solid cathode made of a tissue-equivalent material. However, the number of secondary electrons, delta-rays, produced in a solid material is much more than that in a gaseous one in the case of irradiation of energetic heavy ion beams. The so-called wall effects tend to reduce the number and to increase the mean size of measured events in such a way as to keep the energy deposition constant<sup>1)</sup>.

To lessen the wall effect, the authors have designed and used a wall-less TEPC<sup>2)</sup> in the measurement of energy deposit by heavy ion beams, to measure precise energy deposit including delta-rays. However, it is structurally impossible to completely exclude the wall effect in the measurement using proportional counters. The purpose of this study is to simulate the energy deposit and estimate the contribution of the wall effect to measured energy deposit distributions. By modeling the delta-rays production along with carbon beams with energy of 290 MeV/u, energy deposits by the produced delta-rays in solid and gaseous components of the wall-less TEPC were calculated using EGS5. In this paper, the radial dose distribution and the lineal energy distribution in a wall-less TEPC irradiated by the carbon

ions are reported.

## 2. Materials and Methods

### 2.1 Modeling of the source of delta-rays along with carbon ion beams

Since general-purpose Monte Carlo simulation codes such as PHITS<sup>3)</sup> and MCNPX<sup>4)</sup> do not treat the production of delta-rays in general, we have developed a code to create source files of the delta-rays produced in our wall-less TEPC irradiated by 290 MeV/u carbon beams to simulate the energy deposit from the carbon ions and the delta-rays. The source information such as positions, direction and energy of the delta-rays were determined as follows.

The wall-less TEPC used in the measurement is shown in Fig.1. The carbon beams are incident through a beam window into the wall-less TEPC filled with a propane-based tissue-equivalent gas (TE-gas) at pressure of  $4.0 \times 10^4$  Pa. TE-gas is composed of propane 54.7 %, carbon dioxide 39.7 % and nitrogen 5.6 % in volume percent. The simulated site size in this study is equivalent to 0.72  $\mu\text{m}$  in tissue. The volume surrounded by the helical wire is defined as the detection volume, whose cylindrical height and diameter are both 1.0 mm. The helical wire whose diameter is 50  $\mu\text{m}$  is cathode made of a stainless steel (SUS304). The calculation geometry is shown in Fig.2. The detection volume is irradiated by the beams parallel to the z-axis. Torus geometries were used in the presentation of the cathode for simplification of the modeling. We assume two kinds of sources of the delta-rays produced along with the beam as shown in Fig. 2. Impact parameter  $b$  is defined as a distance between Z-axis and the beam path (see Fig. 2). If the beam hits the cathode, the source is only created in SUS304 because the number of delta-rays is much more than that in TE-gas. In this calculation, the anode wire was ignored because the diameter, 20  $\mu\text{m}$ , is thinner than that of the cathode and the probability that the beams hit on the anode is much smaller than that for the cathode.

The energy spectra of the delta-rays in the materials of the wall-less TEPC were obtained by the equation of Butts and Katz<sup>5)</sup>. The number of secondary electrons per unit length of path having energies in the interval  $\omega$  to  $\omega+d\omega$  is as follows;

$$dn = \frac{CZ^{*2}}{\beta^2} \frac{d\omega}{\omega^2} \quad (1)$$

$$\omega \leq \omega_{\max}$$

$$C = \frac{2\pi N e^4}{m c^2} \quad (= 8.5 eV / \mu m, \text{ in water}),$$

where  $Z^*$  is effective charge of an ion moving with speed  $\beta c$ ,  $m$  and  $e$  are the electron mass and charge,  $N$  is the number density of electrons in the material.

Energy distribution of secondary electrons produced in water by the irradiation of carbon ion with energy of 290 MeV/u is shown in Fig.3. One determined the directions of the delta-rays on the assumption of two-body collision between the carbon ion and electron in the materials, without considering the binding energy of electron in the atoms. The authors set the threshold energy as 100 eV in the TE-gas and SUS304 considering the ionization potentials of them, because below the threshold the energies will be deposited locally. The maximum energy of the delta-rays was estimated 630 keV for 290 MeV/u carbon ion, according to eq.(2).

$$E_{\max} = \frac{4mME}{m^2 + M^2 + 2m\sqrt{2ME + M^2}} \quad (2),$$

where  $m$  and  $M$  are the electron and the carbon mass, respectively, and  $E$  is the incident carbon kinetic energy.

### 2.2 Calculation of energy deposit

Energy deposits in the detection volume from the delta-rays source were calculated by the EGS5 code<sup>6)</sup> combined with the PHITS code, particle and heavy ion transport code system<sup>3)</sup>. The energy cut-off was set 1 keV for

electron. The direct energy deposit by the carbon ions in the detection volume was assumed to be as the product of the stopping power of the carbon ion with energy of 290 MeV/u in the TE-gas multiplied by the chord length crossing the detection volume. Moreover, the values were multiplied by 0.8, because a part of energy deposit will be lost according to a radial dose distribution by Chunxiang et al.<sup>7)</sup>. The source positions of the delta-rays, (X, Y), were randomly determined in the irradiation area shown in Fig.2(b). The beam direction is parallel to the Z-axis. The sources were used as the user-defined sources in the calculation. Then, the calculated energy deposits per source electron in the detection volume were multiplied by the number of the delta-rays produced in a material to obtain a total energy deposit.

Lineal energy<sup>8)</sup>,  $y$ , is defined as the quotient of  $\varepsilon$  by  $\bar{l}$ , where  $\varepsilon$  is the energy imparted to the matter in a volume by a single-energy deposition event and  $\bar{l}$  is the mean chord length in that volume:

$$y = \frac{\varepsilon}{\bar{l}} \quad (3).$$

The mean chord length is  $\pi d/4$  for a right regular circular cylinder (height and diameter are same) with diameter  $d$ , irradiated by beams incident on the cylinder perpendicular to the central axis. The irradiation area by the beams parallel to the z-axis is  $0.01 \text{ cm}^2$  in a case shown in Fig.2.

### 3. Results and discussion

#### 3.1 Radial dose distribution in the wall-less TEPC for 290 MeV/u carbon ion beams

The calculated radial dose distributions are presented in Fig. 4. The x-axis is an impact parameter,  $b$ . It is noted that the calculation was done in the case that the carbon beams directly hit the cathode wire and the probability is 20 % based on the cross-sectional area of the cathode in the detection volume. The value of the X was fixed as zero in the calculation, which means that beams pass the center of a torus. The dose distributions by the four sources along the beam paths are shown. It is found that the direct energy deposit by the carbon beams decrease with  $b$ , because the chord length decrease with  $b$  in the detection volume. The energy deposits from the source in SUS304 increase at the boundary of SUS304 and TE-gas,  $b = 0.05$ , and sharply decrease beyond the boundary. The result is typical wall effect and consistent with the result of a measured radial dose distribution<sup>9)</sup> using a conventional TEPC irradiated by neon with energy of 210 MeV/u.

#### 3.2 Lineal energy distribution in the wall-less TEPC for 290 MeV/u carbon ion beams

Figure 5 shows the calculated lineal energy distributions in the wall-less TEPC irradiated by the carbon ions with energy of 290 MeV/u. The direct energy deposits by the incident carbon ions are included. The range of X-axis of irradiated areas are  $0.0 < X < 0.1$  or  $0.1 < X < 0.2$ , and  $0.0 < Y < 0.1$  (see Fig.2). The vertical axis presents the counts per number of delta-rays in each  $y$ . The incident carbon beams show the main peak around  $10 \text{ keV}/\mu\text{m}$ . The contribution of the delta-rays produced in the TE-gas is found in the  $y$  below  $0.2 \text{ keV}/\mu\text{m}$ . It is found that the energy deposits by the delta-rays from the cathode widely range in  $y$ .

### 4. Summary and future plan

Energy deposits in a wall-less TEPC irradiated by 290 MeV/u carbon ion beams were obtained using EGS5 by modeling the delta-rays production along with the beam path. It is found that the delta-rays produced in a wall-less TEPC along with the carbon beams deposit energies in wide  $y$  region. The calculation based on the more detailed modeling will be performed and compared with measured data in the near future.

## References

- 1) W.A. Glass and W. A. Gross, Topics in radiation dosimetry (4) wall-less detectors in microdosimetry, Academic press (1972).
- 2) S. Tsuda, T. Sato, F. Takahashi, D. Satoh, A. Endo, S. Sasaki, Y. Namito, H. Iwase, S. Ban and M. Takada, Measurement of lineal energy distribution by a wall-less tissue equivalent proportional counter for heavy ion beams, Proceedings of the 23-th Workshop on Radiation Detectors and Their Uses, KEK Proceedings, to be submitted.
- 3) H. Iwase, K. Niita, and T. Nakamura, Development of a general-purpose particle and heavy ion transport Monte Carlo code, J. Nucl. Sci. Technol. **39(11)**, 1142–1151 (2002).
- 4) L. S. Waters, Ed., "MCNPX User's Manual, Version 2.4.0," LA-CP-02-408 (Sept. 2002).
- 5) J. J. Butts and R. Katz, Theory of RBE for heavy ion bombardment of dry enzymes and viruses, Radiat. Res., 30, 855-871 (1967).
- 6) H. Hirayama, Y. Namito, A.F. Bielajew, S.J. Wilderman and W.R. Nelson, The EGS5 Code System, SLAC-R-730 (2005) and KEK Report 2005-8 (2005).
- 7) Z. Chunxiang, D. E. Dunn and R. Katz, Radial distribution of dose and cross-sections for the inactivation of dry enzymes and viruses, Radiat. Prot. Dosim., 13(1-4), 215-218 (1985).
- 8) ICRU, ICRU report 36 (1983).
- 9) S. B. Guetersloh, T. B. Borak, P. J. Taddei, C. Zeitlin, L. Heilbronn, J. Miller, T. Murakami and Y. Iwata, The response of a spherical tissue-equivalent proportional counter to different ions having similar linear energy transfer, Radiat. Res., 161, 64-71 (2004).

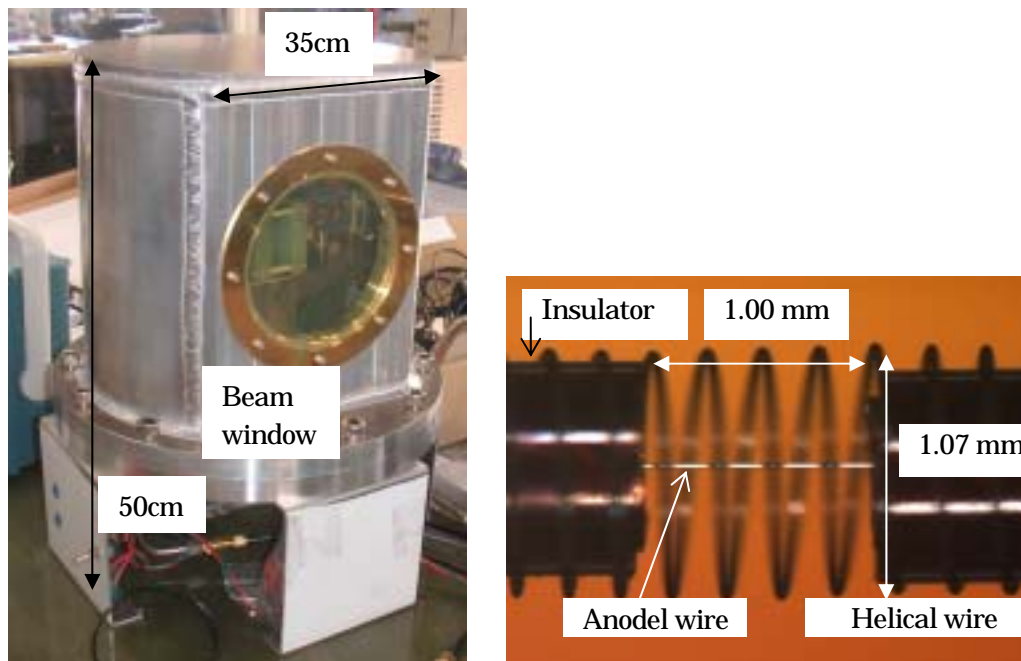


Figure 1: Photographs of the wall-less tissue equivalent proportional counter. Outlook (left) and the detection volume (right) constructed by thin wires are shown.

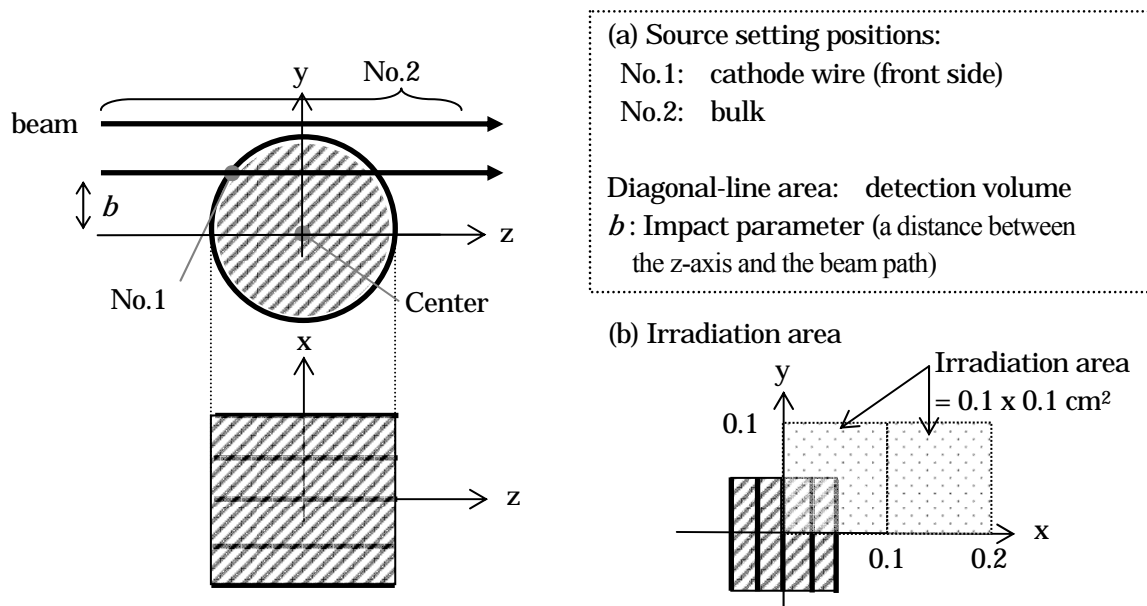


Figure 2: Calculation geometry for energy deposit in the detection volume of the wall-less TEPC.

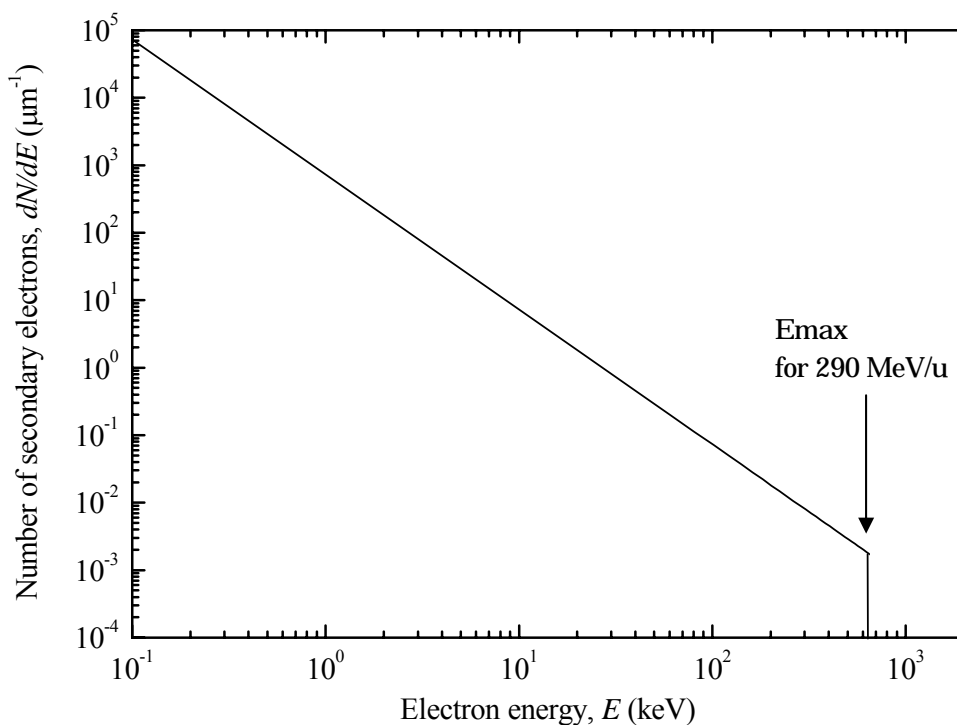


Figure 3: Energy distribution of secondary electrons knock-out by carbon ions with energy of 290 MeV/u in water .

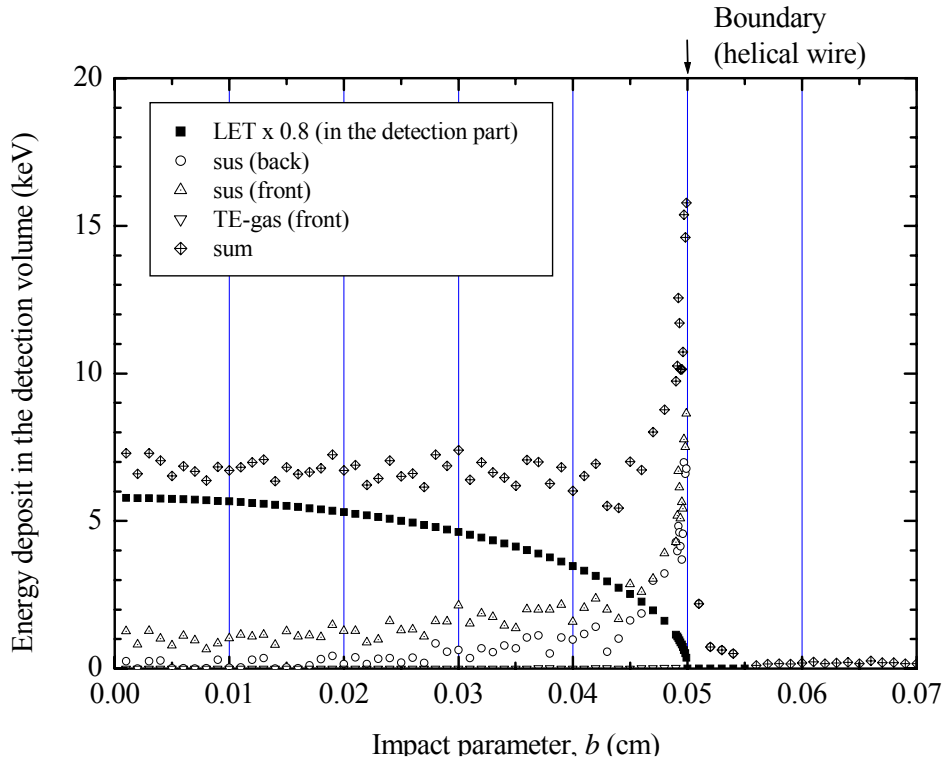


Figure 4: Radial dose distributions calculated by EGS5 in the wall-less TEPC irradiated by carbon ions with energy of 290 MeV/u.

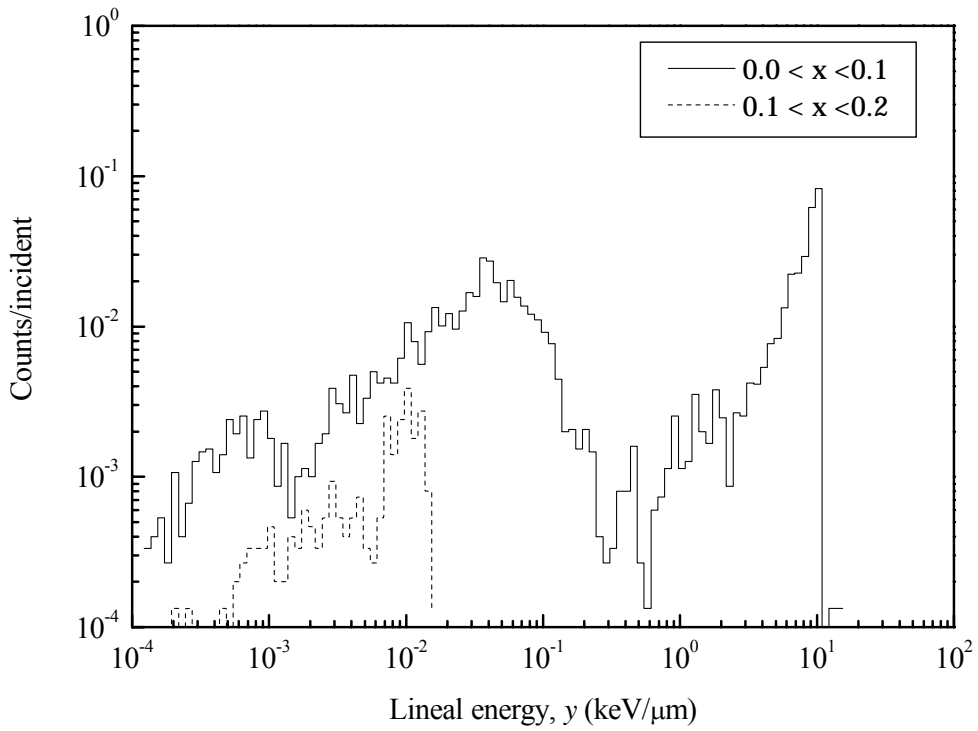


Figure 5: Lineal energy distributions calculated by EGS5 in the wall-less TEPC irradiated by carbon ions with energy of 290 MeV/u.

# Incorporating the LPM effect in the EGS5 code

Y. Kirihara, Y. Namito<sup>†</sup> and H. Hirayama<sup>†</sup>

*The Graduate University for Advanced Studies, Oho1-1, Tsukuba, Ibaraki 305-0801, Japan*

<sup>†</sup>*KEK High Energy Accelerator Research Organization, Oho1-1, Tsukuba, Ibaraki 305-0801, Japan*

## Abstract

We incorporated the Landau-Pomeranchuk-Migdal (LPM) effect and the dielectric suppression effect for bremsstrahlung, and the LPM effect for pair production in the EGS5 code. To verify the validity of the EGS5 code with the LPM plus dielectric cross section for bremsstrahlung, we compared the energy spectrum of bremsstrahlung photon of the calculations using the EGS5 code with that of the LPM effect experiments at primary electron energies of 8, 25, and 287 GeV. The calculated value of the EGS5 code reproduced the experimental value of the LPM effect well.

## 1 Introduction

Electron bremsstrahlung and pair production are two of the most common high-energy electromagnetic processes. The standard description of these processes is the Bethe-Heitler (BH) cross section [1]. However, Landau, Pomeranchuk, and Migdal [2, 3] pointed out that when an ultrarelativistic electron emits a low-energy photon by bremsstrahlung, the BH cross section is suppressed (LPM effect). The LPM effect is a suppression of photon production due to the multiple scattering of the electron. If an electron undergoes multiple scattering while traversing the formation length, the bremsstrahlung amplitudes can be suppressed, reducing the probability of bremsstrahlung photon emission. They also pointed out that a similar suppression occurs for pair production.

In addition, Ter-Mikaelian [4] pointed out that photon interactions can induce suppression. When the bremsstrahlung photon interacts with the electrons in the material by forward Compton scattering, a phase shift in the wave function of the photon is produced. If this phase shift is so large that it cause destructive interference, the photon emission is reduced (dielectric suppression effect). These effects appear at above several GeV for bremsstrahlung and above several TeV for pair production. Thus, these effects are important in the high energy air shower and the next generation colliders such as International Linear Collider (ILC).

In this study, to improve the accuracy of electromagnetic shower calculation at these energy range by using the EGS5 code [5], we incorporated the LPM effect and the dielectric suppression effect for bremsstrahlung, and the LPM effect for pair production in EGS5 code. The LPM effect and the dielectric suppression effect for bremsstrahlung are incorporated in Monte Carlo code as GEANT code [6] and FLUKA code [7]. However, the LPM effect for pair production is not incorporated in these codes.

### 1.1 Bethe-Heitler cross sections in the EGS5 code

In the EGS5 code, the BH cross section for bremsstrahlung of a photon of energy  $k$  by an electron of energy  $E_0$  is obtained as

$$\begin{aligned} \frac{d\sigma_{\text{Brems-BH}}}{dk} &= \frac{A'r_0^2\alpha Z(Z + \xi(Z))}{k} \\ &\times \left\{ (1 + (E/E_0)^2) \left[ \phi_1(\delta) - \frac{4}{3}\ln Z - (4f_c(Z) \text{ if } E_0 > 50, 0) \right] \right. \\ &\left. - \frac{2}{3}\left(\frac{E}{E_0}\right) \left[ \phi_2(\delta) - \frac{4}{3}\ln Z - (4f_c(Z) \text{ if } E_0 > 50, 0) \right] \right\}. \end{aligned} \quad (1)$$

Here,  $E$  is a secondary electron energy,  $\alpha$  is the fine structure constant,  $r_e$  is the classical electron radius,  $Z$  is the atomic number, and other parameters are the same as ref. [5]. The BH cross section for pair production of an electron (positron) of energy  $E_-$  ( $E_+$ ) by a photon of energy  $k_0$  is obtained as

$$\begin{aligned} \frac{d\sigma_{\text{Pair-BH}}}{dE_{-(+)}} &= \frac{A'r_0^2\alpha Z(Z + \xi(Z))}{k_0^3} \\ &\times \left\{ (E_+^2 + E_-^2) \left[ \phi_1(\delta) - \frac{4}{3}\ln Z - (4f_c(Z) \text{ if } k_0 > 50, 0) \right] \right. \\ &\left. + \frac{2}{3}E_+E_- \left[ \phi_2(\delta) - \frac{4}{3}\ln Z - (4f_c(Z) \text{ if } k_0 > 50, 0) \right] \right\}, \end{aligned} \quad (2)$$

where parameters are the same as ref. [5].

## 1.2 LPM plus dielectric cross section for bremsstrahlung

The LPM cross section for bremsstrahlung was given by Migdal [3] and Klein [8] as

$$\frac{d\sigma_{\text{Brems-LPM}}}{dk} = \frac{4\alpha r_e^2 \xi(s)}{3k} \{y^2 G(s) + 2[1 + (1 - y)^2] \phi(s)\} Z^2 \ln\left(\frac{184}{Z^{1/3}}\right), \quad (3)$$

where  $y = k/E_0$ .  $\xi(s)$ ,  $G(s)$ , and  $\phi(s)$  are functions of

$$s = \left( \frac{E_{\text{LPM}} k}{8E_0(E_0 - k)\xi(s)} \right)^{1/2}. \quad (4)$$

Here,  $E_{\text{LPM}}$  depends on the radiation length  $X_0$ , given by

$$E_{\text{LPM}} = 7.7 \text{ TeV/cm} \cdot X_0. \quad (5)$$

$G(s)$  and  $\phi(s)$  are infinite series. In addition, Eq. (4) require an iterative procedure for solution, since  $\xi(s)$  appearing on the right-hand side is itself a function of  $s$ . Thus, it is difficult to use Eq. (3) with these equations for Monte Carlo codes directly. To calculate Eq. (3) easily, Stanev et al. [9] gave polynomials of  $G(s)$  and  $\phi(s)$ , and approximate equations without iteration of  $\xi(s)$  and  $s$  as Eq. (13) to Eq. (22) in their paper. We adopted the equations given by Stanev et al. to calculate Eq. (3) for the EGS5 code. In the absence of suppression  $s \rightarrow \infty$ ,  $G(s) \rightarrow 1$  and  $\phi(s) \rightarrow 1$ ; strong suppression corresponds to  $s \rightarrow 0$ ,  $G(s) \rightarrow 0$  and  $\phi(s) \rightarrow 0$ . Figure 1 shows the BH cross section as Eq. (1) and the LPM cross section as Eq. (3) per radiation length,  $X_0 n y d\sigma/dy$ , for Pb, where  $n$  is atomic density. As  $E_0$  rises, the LPM cross section drops, with low energy photons suppressed the most.

Migdal [3] considered dielectric suppression effect for bremsstrahlung. Since it occurs only for  $y \ll 1$ , only the  $\phi$  term is relevant: Migdal replaced  $\phi(s)$  with  $\phi(s\Gamma)/\Gamma$  to get

$$\frac{d\sigma_{\text{diel}}}{dk} = \frac{16\alpha r_e^2 \xi(s)}{3k} \frac{\phi(s\Gamma)}{\Gamma} Z^2 \ln\left(\frac{184}{Z^{1/3}}\right), \quad (6)$$

where  $\Gamma = 1 + (k_p^2/k^2)$ ,  $k_p = \gamma \hbar \omega_p$ ,  $\gamma = E_0/mc^2$ ,  $\omega_p = \sqrt{4\pi n Z e^2/m}$ ,  $m$  is the electron mass,  $c$  is the speed of light, and  $e$  is the electric charge.

To calculate both the LPM effect and the dielectric suppression effect, we give the differential cross section for bremsstrahlung as

$$\frac{d\sigma_{\text{Brems-LPM-diel}}}{dk} = \frac{4\alpha r_e^2 \xi(s)}{3k} \{y^2 G(s) + 2[1 + (1 - y)^2] \frac{\phi(s\Gamma)}{\Gamma}\} Z^2 \ln\left(\frac{184}{Z^{1/3}}\right). \quad (7)$$

Figure 2 shows the comparison of the cross section function for bremsstrahlung for C at an incident energy of 25 GeV. When  $y \geq 1.4 \times 10^{-3}$ , the LPM plus dielectric cross section as Eq. (7) is equivalent to the LPM cross section as Eq. (3). On the other hand, when  $y < 1.4 \times 10^{-3}$ , the LPM plus dielectric cross section as Eq. (7) is equivalent to the dielectric cross section as Eq. (6).

### 1.3 LPM cross section for pair production

The LPM effect for pair production of an electron (positron) of energy  $E_-$  ( $E_+$ ) by a photon of energy  $k_0$  was given by Migdal [3] as

$$\frac{d\sigma_{\text{Pair-LPM}}}{dE} = \frac{4\alpha r_e^2 \xi(\tilde{s})}{3k_0} \left\{ G(\tilde{s}) + 2[v^2 + (1-v)^2] \phi(\tilde{s}) \right\}, \quad (8)$$

where  $v = E_{-(+)}/k_0$ ,

$$\tilde{s} = \sqrt{\frac{E_{\text{LPM}} k_0}{8E(k_0 - E)\xi(\tilde{s})}}. \quad (9)$$

Here, as well as Eq. (3), Stanev et al. [9] gave polynomials of  $G(\tilde{s})$  and  $\phi(\tilde{s})$ , and approximate equations without iteration of  $\xi(\tilde{s})$  and  $\tilde{s}$  as Eq. (13) to Eq. (22) in their paper. In the limit  $\tilde{s} \gg 1$  there is no suppression, while  $\tilde{s} \rightarrow 0$  indicates large suppression. Figure 3 shows the BH cross section as Eq. (2), and the LPM cross section as Eq. (8) per radiation length,  $X_0 n v d\sigma/dv$ , for Pb. As  $k_0$  rises, the LPM cross section drops, with electrons (positrons) of energy of  $k_0/2$  suppressed the most.

## 2 Methods

### 2.1 Calculation of the LPM effect and the dielectric suppression effect

We incorporated the LPM plus dielectric cross section for bremsstrahlung according to Eq. (7) in the EGS5 code by using the rejection method. We added a new subroutine LPMB, and added the rejection method algorithm to a subroutine BREMS in the EGS5 code. The subroutine LPMB calculates the ratio of the LPM plus dielectric cross section to the BH cross section for atomic number, a primary electron energy, and an emitted photon energy. At the additional part in the subroutine BREMS, the emitted photon sampled by the BH cross section is rejected according to this ratio. Flow diagrams of the additional part of subroutine BREMS and the subroutine LPMB are shown in Fig. 4 and 5, respectively.

We also incorporated the LPM cross section for pair production according to Eq. (8) in the EGS5 code by using the rejection method. We added a new subroutine LPMP, and added the rejection method algorithm to a subroutine PAIR in the EGS5 code. The subroutine LPMP calculates the ratio of the LPM cross section to the BH cross section for atomic number, a primary photon energy, and an emitted electron (positron) energy. Flow diagrams of the additional part of subroutine PAIR and the subroutine LPMP are shown in Fig. 6 and 7, respectively.

### 2.2 Comparison with the experimental values

To verify the validity of the EGS5 code with the LPM plus dielectric cross section for bremsstrahlung, we compared the energy spectrum of photon of the calculation using the EGS5 code with that of LPM effect measurement. We calculated the energy spectrum by using the EGS5 code with both the BH cross section and the LPM plus dielectric cross section for bremsstrahlung.

Anthony et al. [10] measured the energy spectrum of photon produced by bremsstrahlung at incident electron energies of 8 and 25 GeV using a bismuth germanate (BGO) calorimeter. Target thicknesses were from 0.7% to 6%  $X_0$ . Targets C, Al, Fe, W, Au, Pb, and U were used. Anthony et al. also indicated the energy spectrum of photon calculated by Monte Carlo using LPM plus dielectric cross section. A single electron traversing the target may interact more than once, emitting more than one photon. Then, the energy of these photons is deposited in the BGO

calorimeter (multi-photon pileup). Thus, the calculations of EGS5 code took into account the multi-photon pileup.

Hansen et al. [11] measured the energy spectrum of photon produced by bremsstrahlung at incident electron energies of 149, 207, and 287 GeV using a lead glass (LG) detector. Target thickness was  $4.4\%X_0$ . Targets Cu, Ta, and Ir were used. Hansen et al. also indicated the energy spectrum of photon calculated by using GEANT code [6] with the LPM cross section. For Hansen’s experiment, the dielectric suppression effect was practically irrelevant because the effective energy range of the dielectric suppression effect was very small in comparison with that of the LPM effect. The multi-photon pileup also occurred for Hansen’s experiment. Thus, the calculation using the EGS5 code took into account the multi-photon pileup.

### 3 Results and Discussions

Figure 8 shows the energy spectrum of bremsstrahlung photon for C and Au targets of thickness of  $6\%X_0$  at incident electron energies of 8 and 25 GeV for Anthony’s experiment. The energy spectrum was plotted with the bins having a logarithmic width from 0.2 to 500 MeV. The calculations of the EGS5 code and Antony’s Monte Carlo calculation were normalized by using normalization constants as listed in Table 1. Energy ranges for normalization were 2 to 500 MeV and 20 to 500 MeV for 8 GeV and 25 GeV, respectively. The calculations of the EGS5 code of the LPM

Table 1: values of normalization constants of the calculation using the EGS5 code and Anthony’s Monte Carlo calculation.

Label in Figure 8	Normalization constant [%]	
	EGS5	Anthony(97)
(a) 8 GeV : $6\%X_0$ Carbon	-2.1	-4.6
(b) 8 GeV : $6\%X_0$ Gold	-1.3	-5.0
(c) 25 GeV : $6\%X_0$ Carbon	-1.3	-5.0
(d) 25 GeV : $6\%X_0$ Gold	-1.5	-5.5

plus dielectric cross section and Anthony’s experimental values are good agreement in almost all the energy range. However, for Figure 8 (b) and (c), the calculation using the EGS5 code of the LPM plus dielectric cross section underestimates below photon energy of 0.7 MeV. The reason of this is that the transition radiation effect [12] is not treated in the calculation using the EGS5 code.

Figure 9 shows the energy spectrum of bremsstrahlung photon for Cu and Ir targets of thickness of  $4.4\%X_0$  at an incident electron energy of 287 GeV for Hansen’s experiment. The energy spectrum was plotted with the bins having a logarithmic width from 2 to 287 GeV. The calculations of the EGS5 code and Hansen’s GEANT calculation were not normalized. The calculations of the EGS5 code of the LPM cross section and Hansen’s experimental values are good agreement in all the energy range.

For bremsstrahlung, the calculated value of the EGS5 code with the LPM effect and the dielectric suppression effect reproduced the experimental values well. Unfortunately, comparison of calculated and experimental values for pair production was not performed because there was no reliable experimental values of the LPM effect for pair production.

### References

- [1] International Commission on Radiation Units and Measurements: “Stopping Powers for Electrons and Positrons”, ICRU Report 37 (1984).

- [2] L. D. Landau and I. J. Pomeranchuk, Doklady Akad. Nauk SSSR **92**, No. 3, 535 (1953).
- [3] A. B. Migdal, Phys. Rev. **103**, 1811 (1956).
- [4] M. L. Ter-Mikaelian, *High Energy Electromagnetic Processes in Condensed Media*, John Wiley, New York, 1972.
- [5] H. Hirayama, Y. Namito, A. F. Bielajew, S. J. Wilderman and W. R. Nelson, "The EGS5 Code System." Report SLAC-R-730 and KEK Report 2005-8, (2005).
- [6] S. Agostinelli *et al.*, Nucl. Instr. Meth. A **506**, 250 (2003).
- [7] A. Fassò, A. Ferrari, J. Ranft, P. R. Sala, G. R. Stevenson and J. M. Zazula, FLUKA92 Proc. Workshop on Simulating Accelerator Radiation Environments, Santa Fe (New Mexico), 11-15 January 1993, Los Alamos report **LA-12835-C**, 134 (1994).
- [8] S. Klein, Rev. Mod. Phys. **71**, 1501 (1999).
- [9] T. Stanev *et al.*, Phys. Rev. D **25**, 1291 (1982).
- [10] P. L. Anthony *et al.*, Phys. Rev. D **56** 1373 (1997).
- [11] H. D. Hansen *et al.*, Phys. Rev. D **69**, 032001 (2004).
- [12] J. D. Jackson, *Classical Electrodynamics*, 2nd ed. (Wiley, New York, 1975), p.687.

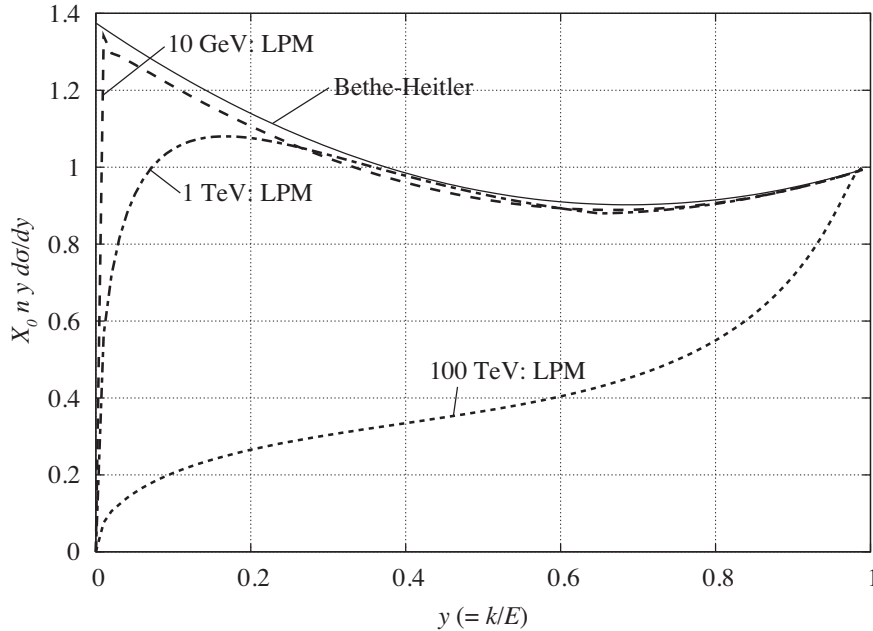


Figure 1: Energy spectrum of photon per radiation length for bremsstrahlung for Pb. Solid line: the BH cross section; dashed line, dot-dashed line, and dotted line: the LPM cross section at an incident electron energy of 10 GeV, 1 TeV, and 100 TeV, respectively.

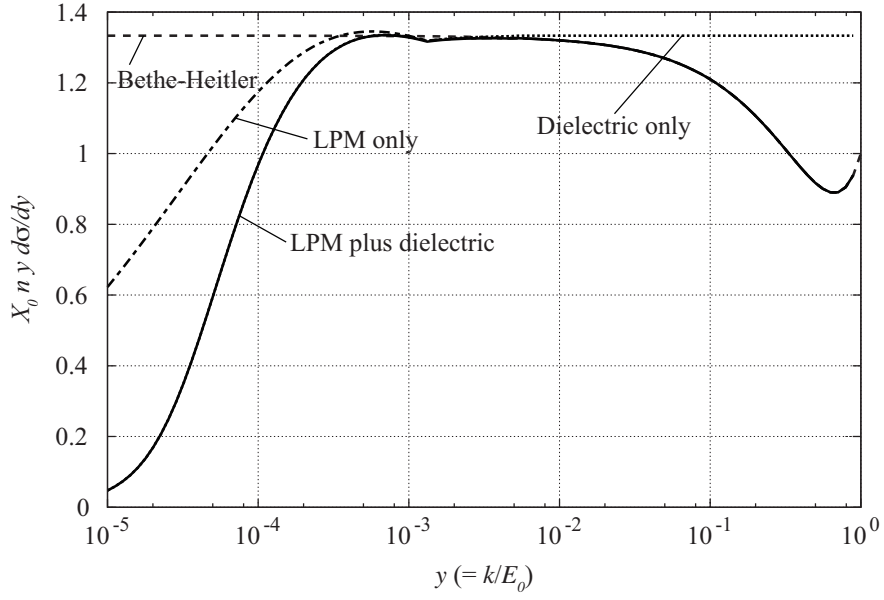


Figure 2: Comparison of the cross section equation for bremsstrahlung for C at an incident electron energy of 25 GeV. Solid line: the LPM plus dielectric cross section as Eq. (7); dashed line: the BH cross section as Eq. (1); dot-dashed line: the LPM cross section as Eq. (3); dotted line: the dielectric cross section as Eq. (6).

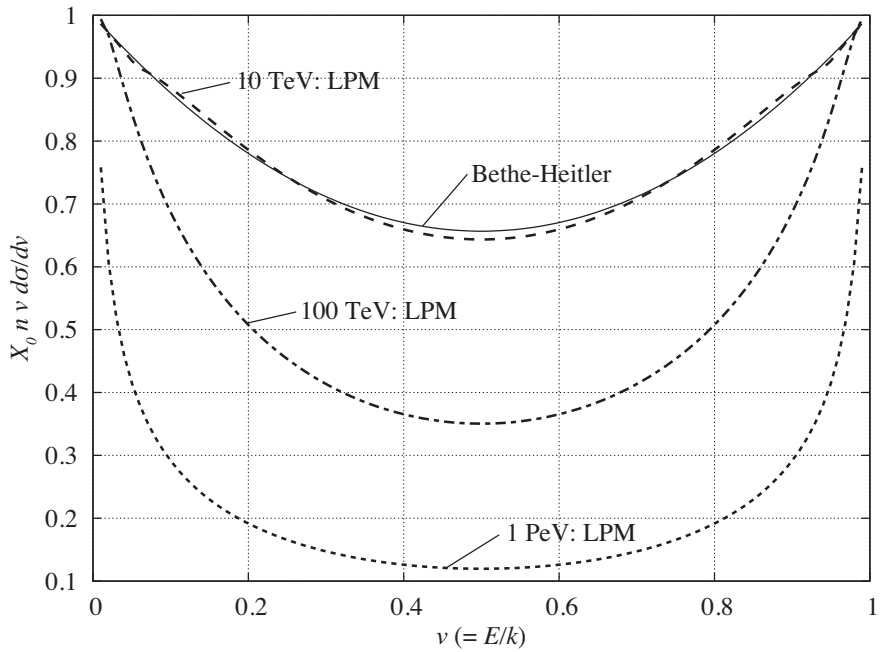


Figure 3: Energy spectrum of electron (positron) per radiation length for pair production for Pb. Solid line: the BH cross section; dashed line, dot-dashed line, dotted line: the LPM cross section at an incident electron energy of 10 TeV, 100 TeV, and 1 PeV, respectively

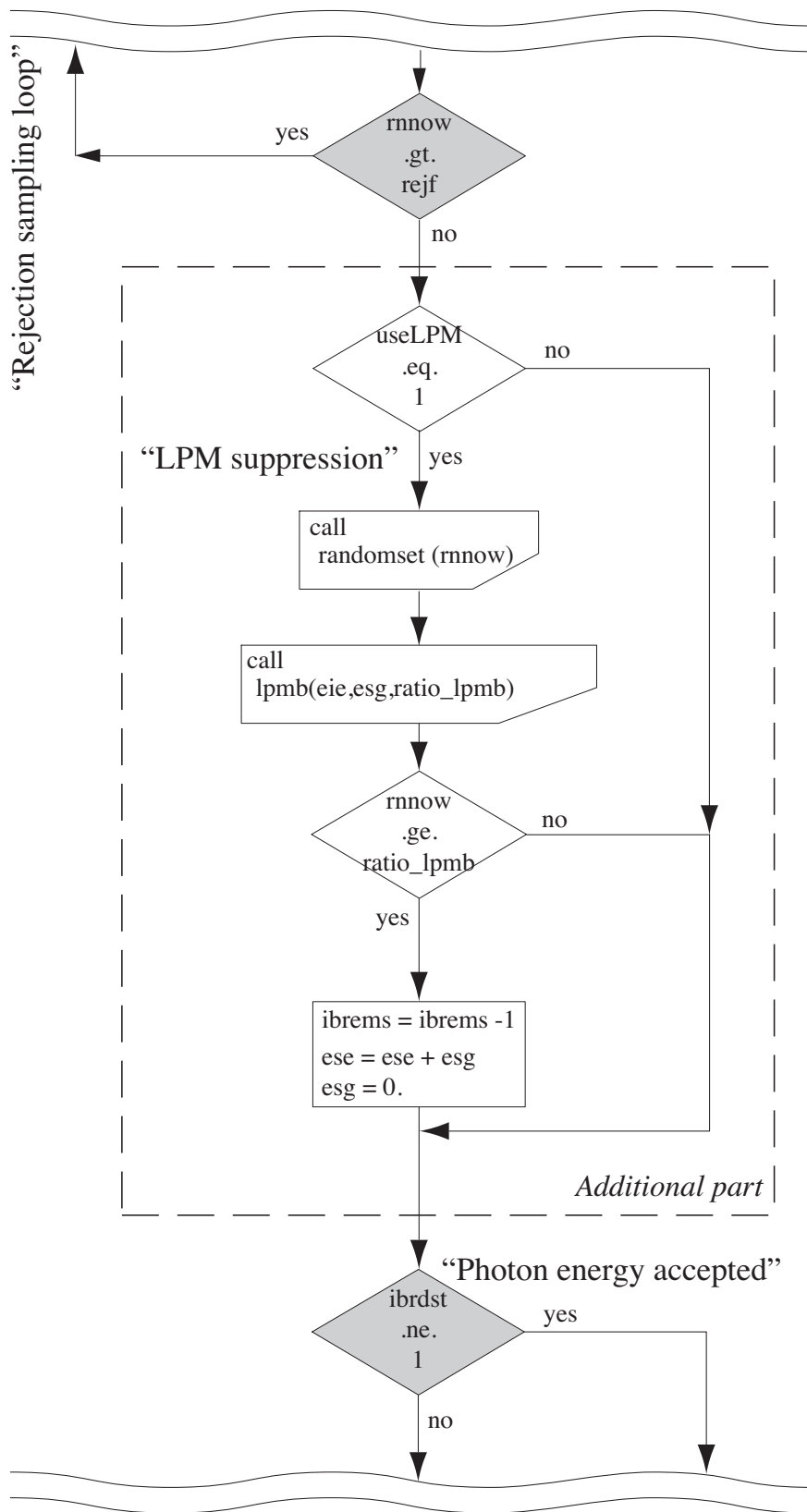


Figure 4: Flow diagram of subroutine BREMS (additional part).

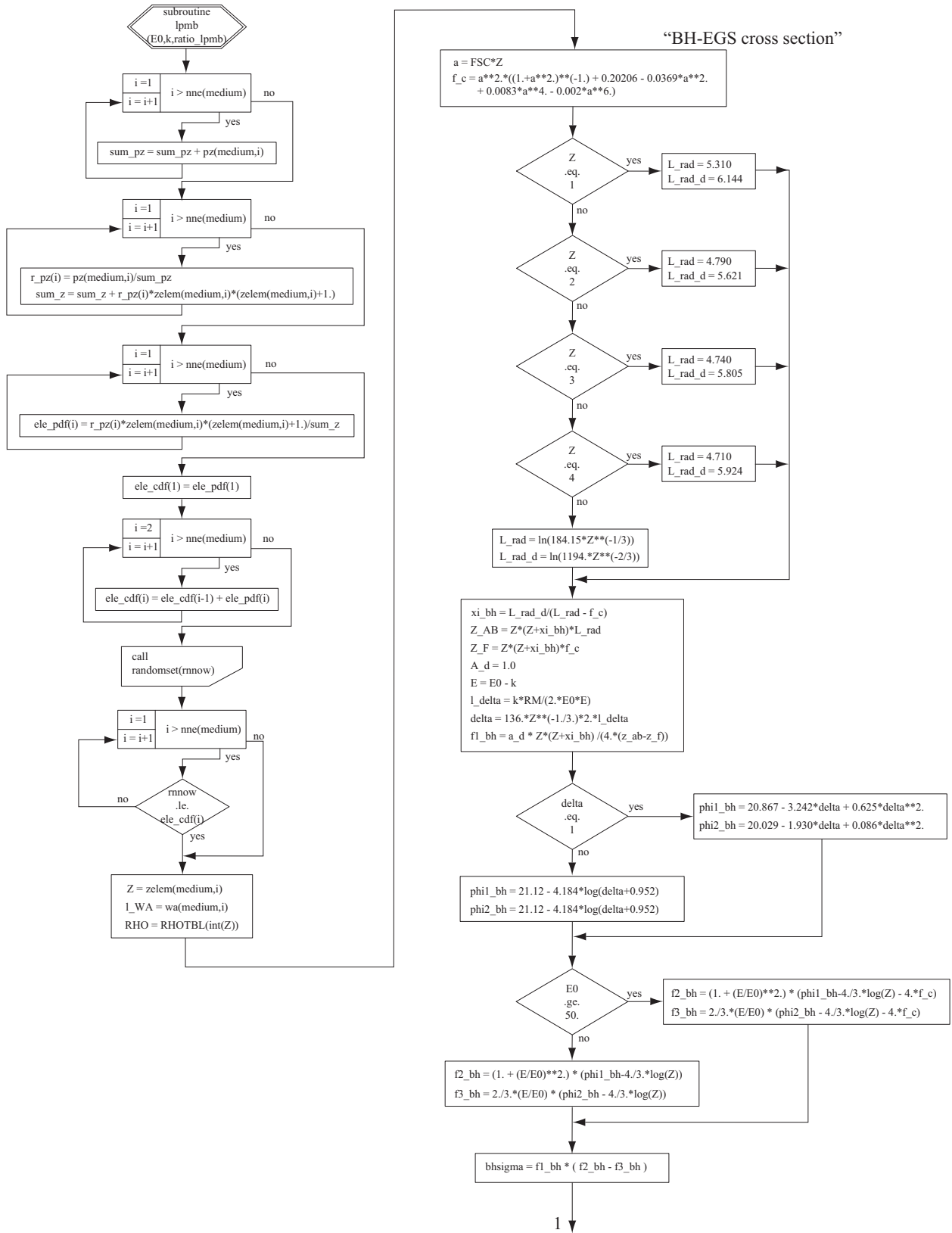


Figure 5: Flow diagram of subroutine LPMB.

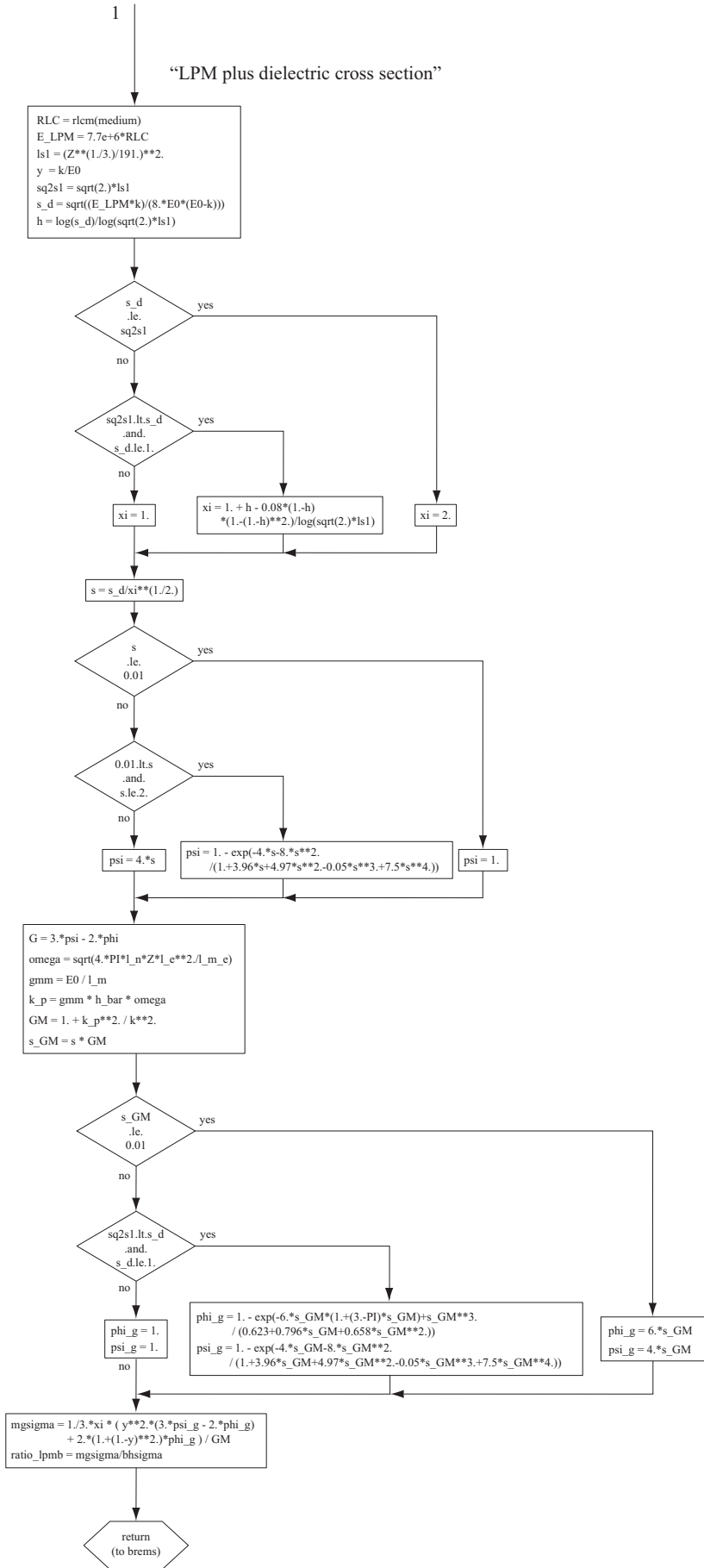


Figure 5: *Continued*

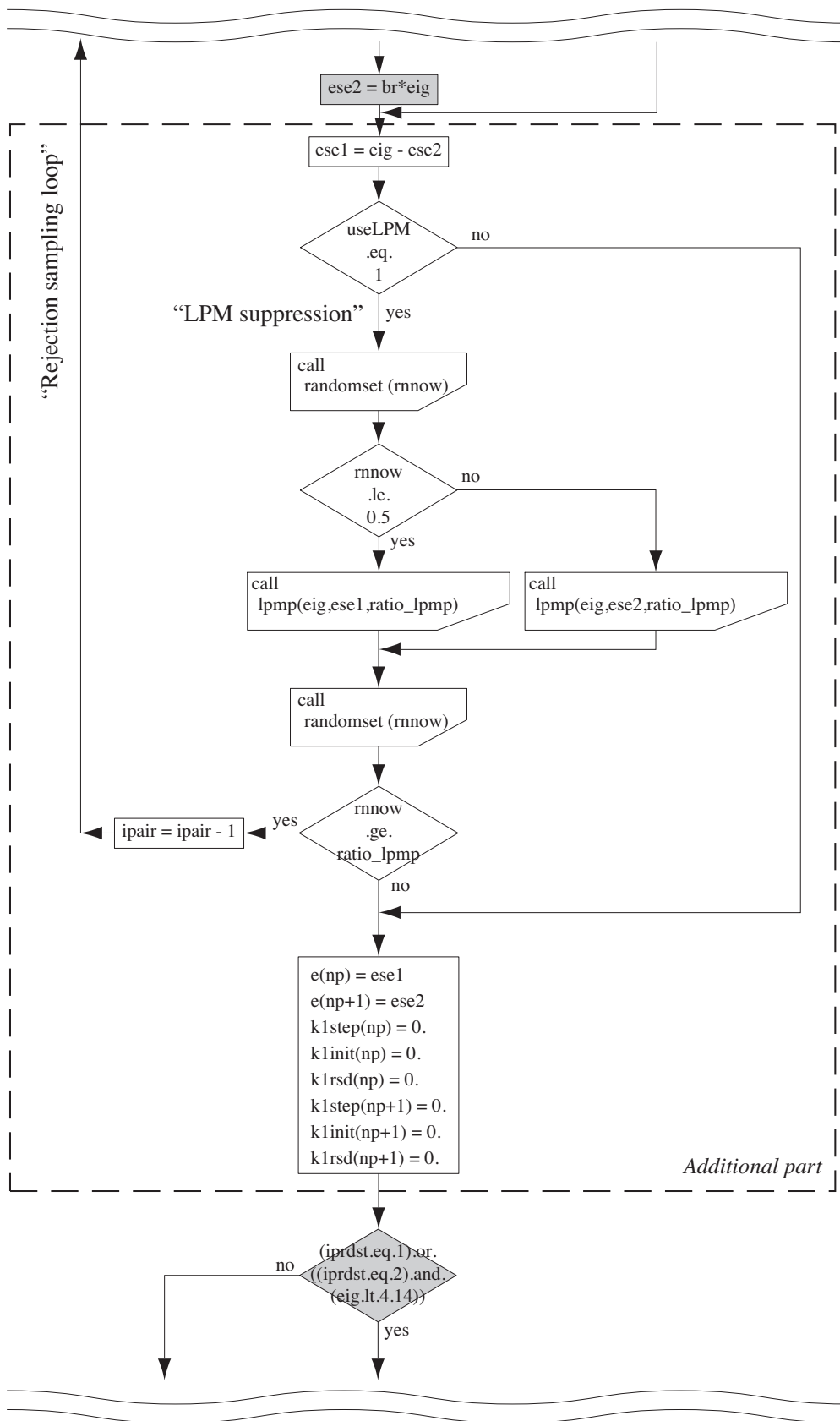


Figure 6: Flow diagram of subroutine PAIR (additional part).

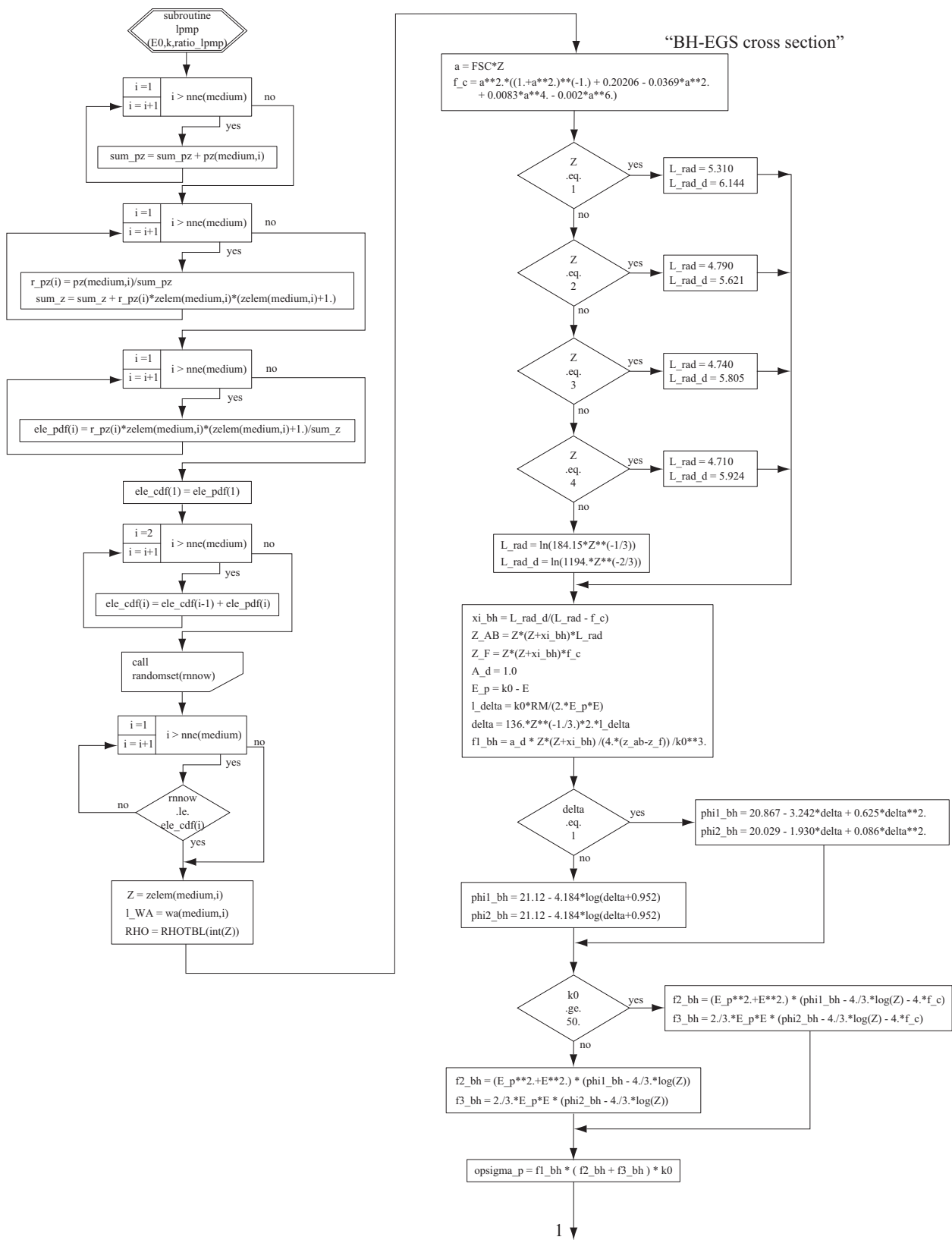


Figure 7: Flow diagram of subroutine LPMP.

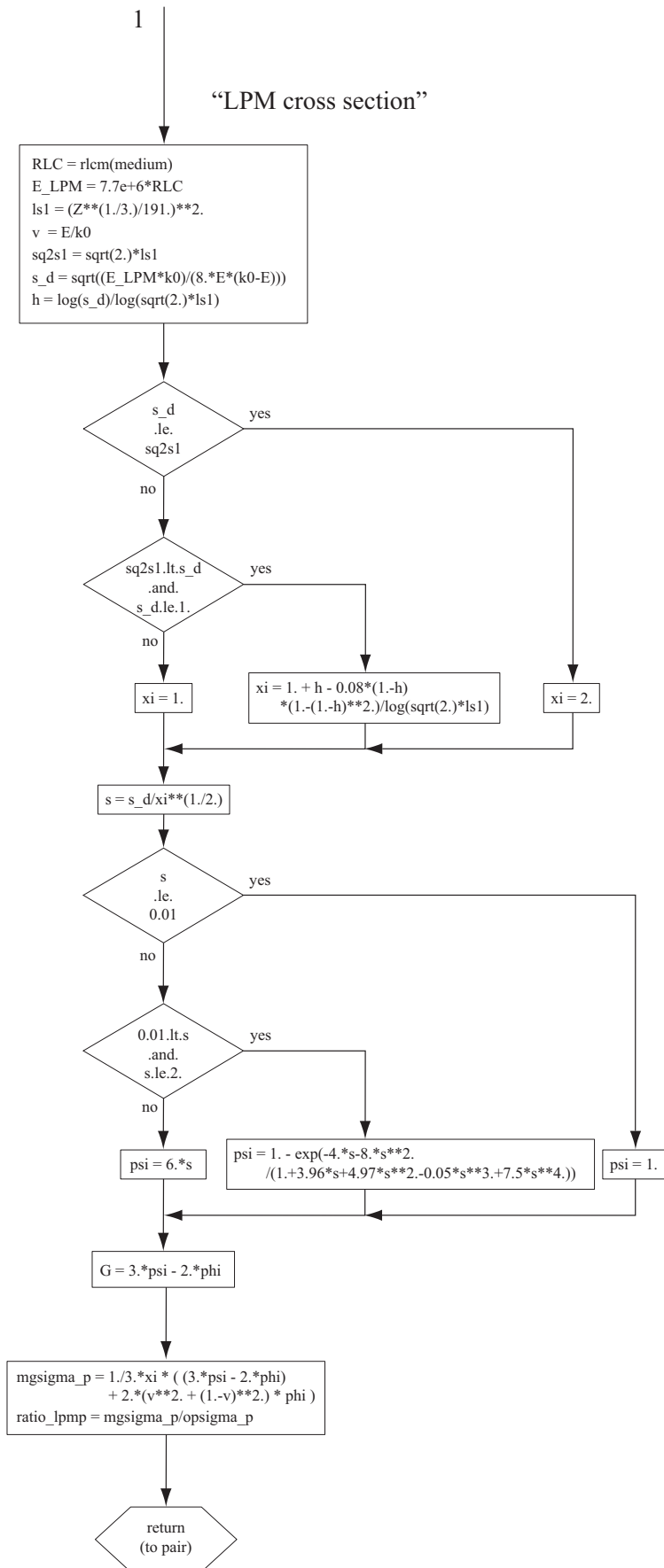


Figure 7: *Continued*

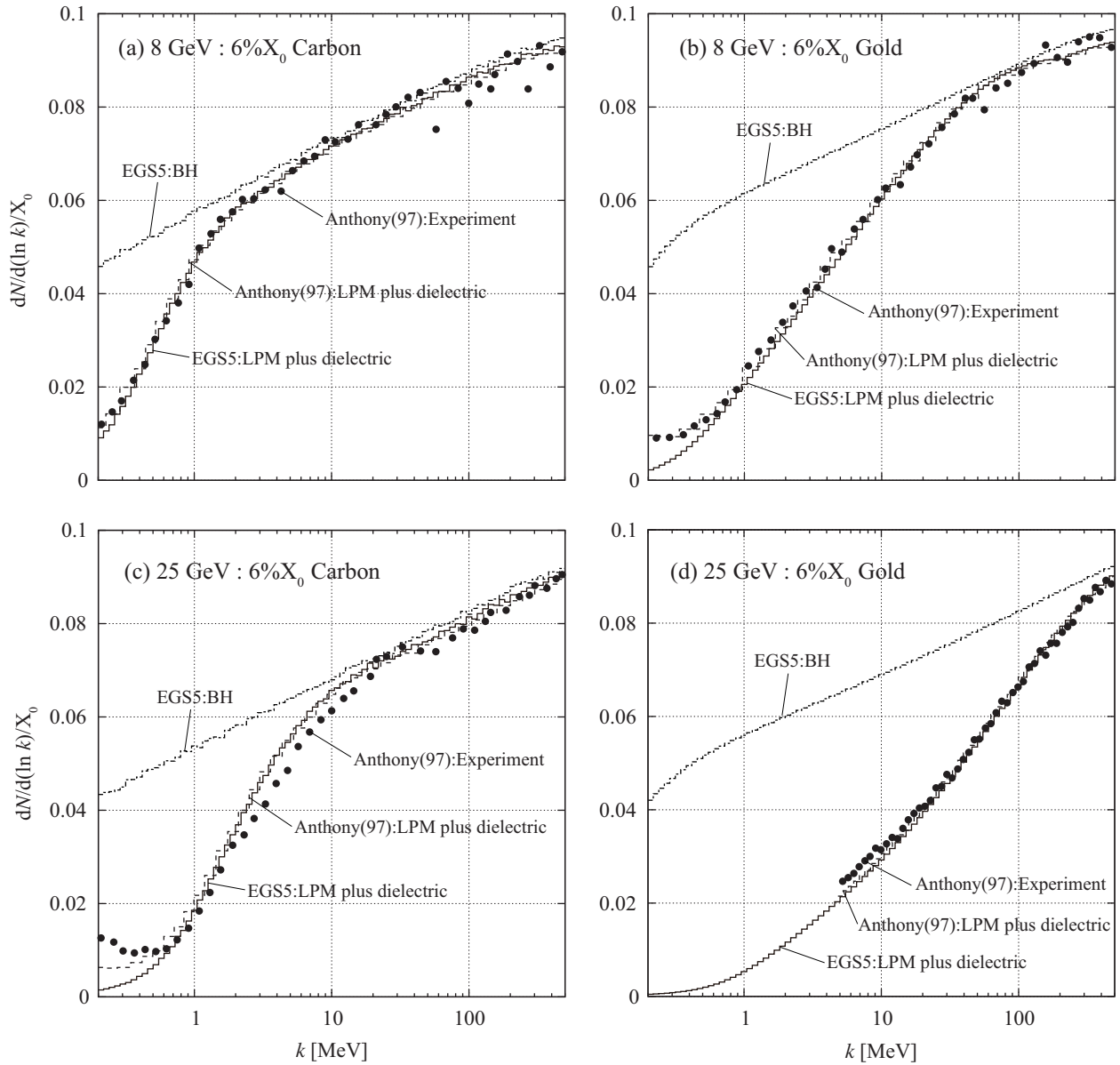


Figure 8: Energy spectrum of photon for (a) C and (b) Au targets at incident electron energies of 8 GeV, and (c) C and (d) Au targets at incident electron energies of 25 GeV. Filled circle: Anthony's experimental value; dashed line: Anthony's Monte Carlo calculation of the LPM plus dielectric cross section; solid line: the EGS5 calculation of the LPM plus dielectric cross section; dot-dashed line: the EGS5 calculation of the BH cross section.

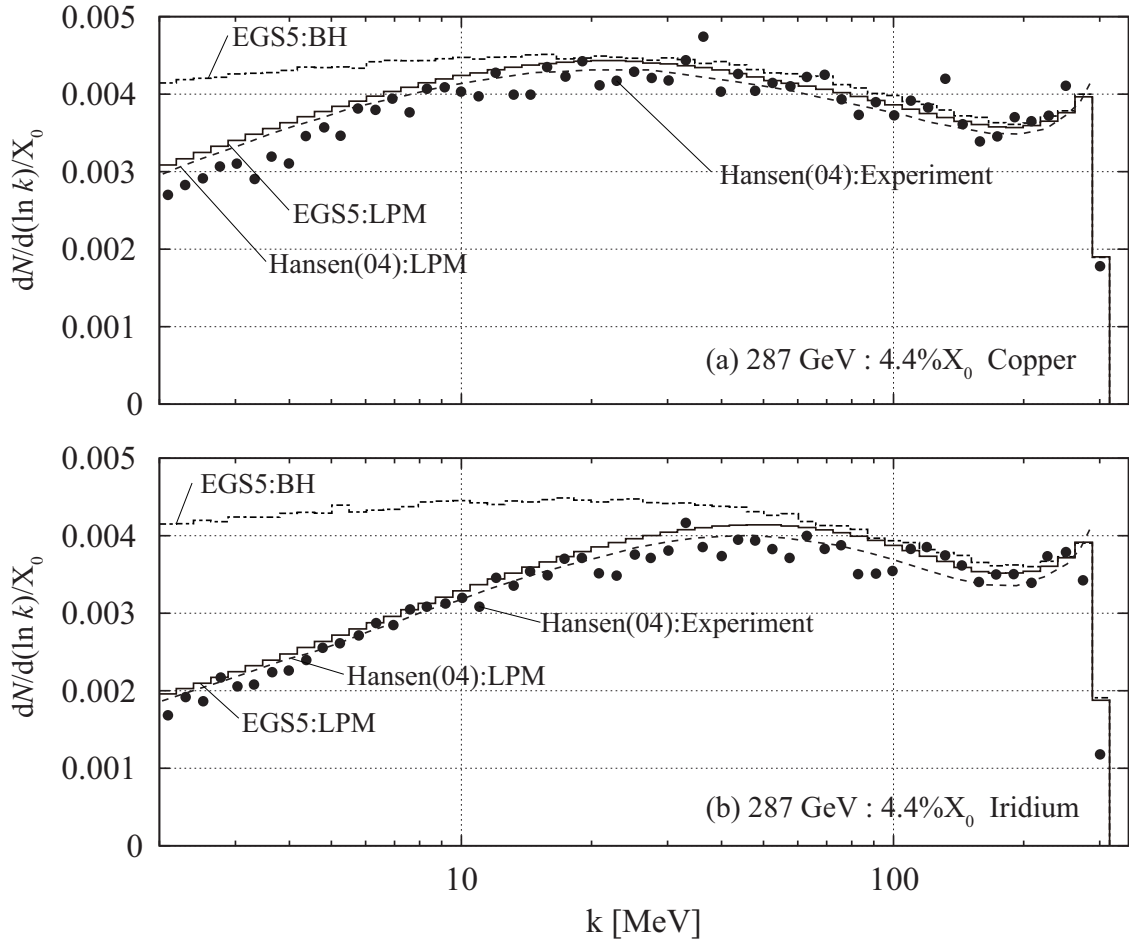


Figure 9: Energy spectrum of photon for (a) Cu and (b) Ir targets at incident electron energies of 287 GeV. Filled circle: Hansen’s experimental value; dashed line: Hansen’s GEANT calculation of the LPM cross section; solid line and dot-dashed line: the EGS5 calculation of the LPM cross section and the BH cross section, respectively.

# Charged particle transport calculation with GPU 2

K. Okei<sup>†</sup> and T. Nakatsuka<sup>‡</sup>

<sup>†</sup>*Kawasaki Medical School, Kurashiki 701-0192, Japan*

<sup>‡</sup>*Okayama Shoka University, Okayama 700-8601, Japan*

## Abstract

A GPU (graphics processing unit) was examined to see if it accelerates charged particle transport simulations. Having performed Monte Carlo simulations, we found that a GPU (NVIDIA GeForce 8800 GTX) outperforms a general purpose CPU (Intel Core2Duo E6700) by more than an order of magnitude for the cases where the mean number of Coulomb scattering per event is larger than 100.

## 1 Introduction

We have been studying the effectiveness of the GPU (graphics processing unit) computing for the charged particle transport. In the fifteenth EGS meeting, we reported that GPU can accelerate the sampling routines for generating the deflection angles due to Coulomb scattering by over an order of magnitude and the GPU accelerated simulation was used to validate a newly developed method for simulating large angle multiple scattering which includes the spin effect [1].

In this work, a Monte Carlo code of charged particle transport is implemented on a GPU (NVIDIA GeForce 8800 GTX) using CUDA [2, 3] and the execution time is compared with the CPU (Intel Core2Duo E6700) execution time. The GPU Monte Carlo simulation yields, the angular deflection  $\theta$ , lateral deviation  $r$  and actual path length  $s = t + \Delta$  of a particle after passing through a foil of thickness  $t$ . The analytical probability distribution of, the excess path length  $\Delta$ , joint or conditional probability distributions of  $\Delta$  and  $r$  are calculated according to Yang [4] and Nakatsuka [5] using a numerical inverse Laplace transform algorithm [6]. The distributions obtained from the GPU simulation and the analytical calculation are compared for validation.

## 2 Monte Carlo simulation

Charged particles passing through matter suffer deflections due to Coulomb scattering, and the process is the main source of the angular and lateral spreads (figure 1). In the GPU Monte Carlo simulation, we have a charged particle incident on the origin of the reference frame with the initial direction along the  $z$  axis. The simulation yields, the angular deflection  $\theta$ , lateral deviation  $r = \sqrt{x^2 + y^2}$  and actual path length  $s = t + \Delta$  of a particle after passing through a foil of thickness  $t$ . Or it can yield the  $z$  coordinate of a particle with a prescribed path length. As a example, simple simulations were performed with deflection angles sampled from Gaussian distributions. The RMS angle  $\sigma$  and mean free path  $\lambda$  of scattering were set to be  $\sigma = \sigma_\theta / \sqrt{\mu} = \sigma_\theta / \sqrt{t/\lambda}$  and  $\lambda = t/\mu$  respectively, so that the variances of angular deflection at  $s = t$  can be assumed to have constant value  $\sigma_\theta^2$  for different values of  $\mu$ .

Figure 2 shows the conditional probability density distribution of  $z$  given  $s = t$ ,  $f(z|s = t)$  (solid histogram) and that of  $s$  given  $z = t$ ,  $f(s|z = t)$  (dotted histogram) for  $\mu = 100$  and  $\sigma_\theta = 0.1$ . It seems that the distributions are symmetrical about  $s = t$  or  $z = t$ . This suggests that the conditional probability distribution of  $z - t$  given  $s = t$  is the same as the distribution of the excess path length  $\Delta = s - t$  given  $z = t$  (figure 3) in the case where the small angle approximation is

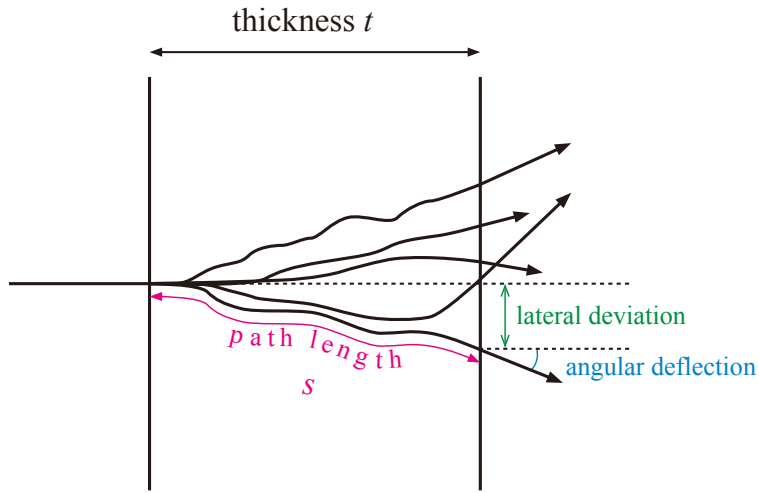


Figure 1: A schematic diagram of the projected trajectories of charged particles passing through a matter of thickness  $t$ .

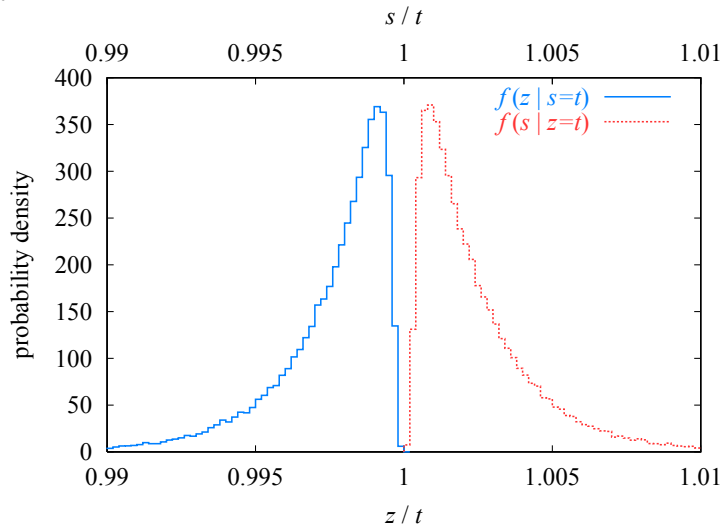


Figure 2: The conditional probability density distributions,  $f(z|s = t)$  (solid histogram) and  $f(s|z = t)$  (dotted histogram).

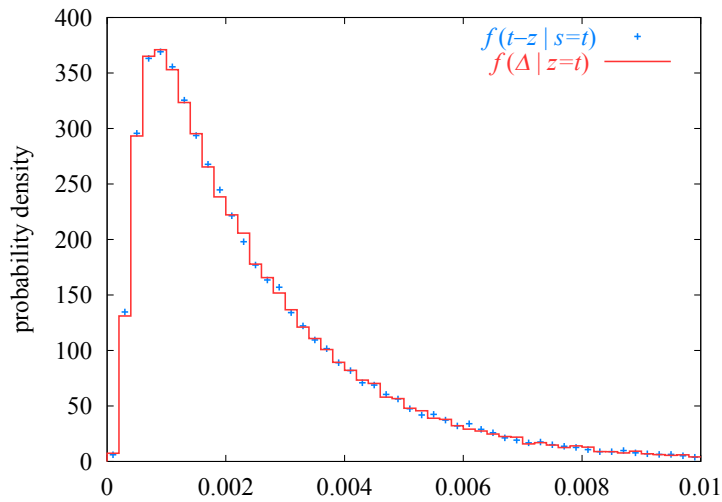


Figure 3: The conditional probability density distributions,  $f(t - z|s = t)$  (cross) and  $f(\Delta|z = t)$  (solid histogram).

Table 1: The comparison between CPU and GPU execution time of the Monte Carlo simulation.

processor	number of events	execution time (s)		
		$\mu = 10$	$\mu = 100$	$\mu = 1000$
CPU (Core2Duo E6700 2.66 GHz)	$2^{20} = 1048576$	4.2	41	410
GPU (GeForce 8800 GTX)	$2^{24} = 16777216$	10	61	510
ratio of the execution times		6.7	11	13

valid ( $\sigma_\theta \ll 1$ ). Hence we will focus hereafter on the excess path length  $\Delta$  given  $z = t$  rather than  $z$  given  $s = t$ .

Table 1 shows the comparison between CPU and GPU execution time of the Monte Carlo simulation for  $\mu = 10, 100$  and  $1000$ . The GPU codes were compiled with the `-use_fast_math` option [2]. In the simulation, floating-point arithmetic was performed in single precision. To generate uniform pseudo random numbers, “taus88” described in L’Ecuyer [7] was used. Since the simulation is processed in parallel on the GPU, the seed values are initialized by random numbers for each thread. We see that the GPU Monte Carlo simulation is more than 10 times faster than the CPU version for  $\mu \geq 100$ .

### 3 The excess path length

In order to test the validity of the GPU simulation, the excess path length distributions were compared with the analytical ones [5] obtained using a numerical inverse Laplace transform [6]. In the comparison, the variables  $\Delta$ ,  $r$  were scaled according to ref.[5] as  $u = \Delta/\frac{1}{2}t\sigma_\theta^2$ ,  $\rho = r/\sqrt{\frac{1}{3}t^2\sigma_\theta^2}$ . As an example of the analytical results, figure 4 shows the joint probability density distribution of the excess path length and lateral displacement  $f(u, \rho)$ .

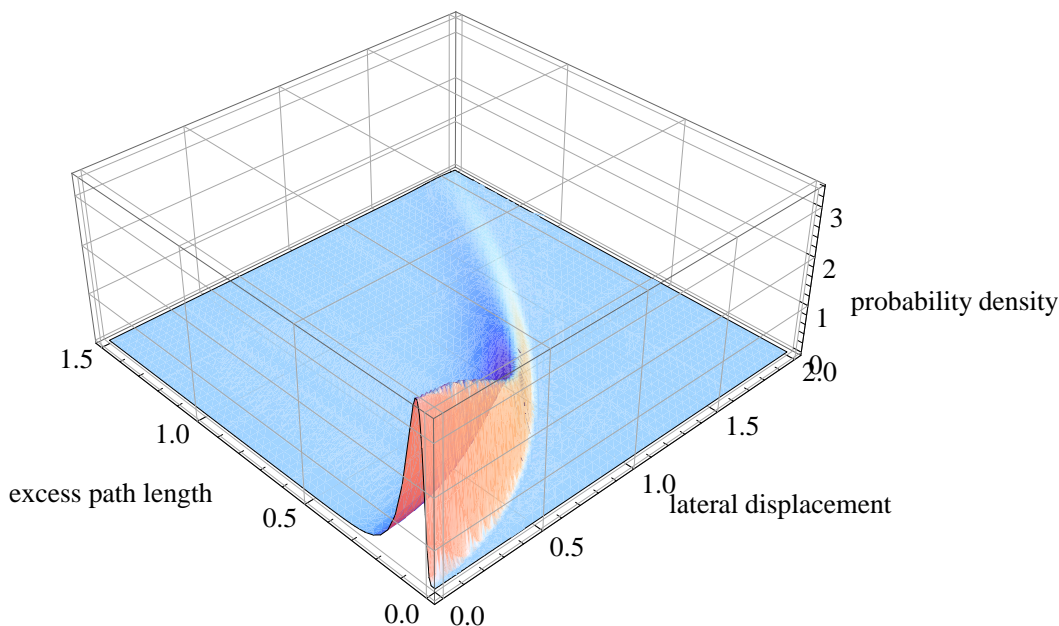


Figure 4: The joint probability density of the excess path length and lateral displacement.

The excess path length distribution for  $\mu = 100, 1000$  and  $\sigma_\theta = 0.1$  obtained from the GPU simulation is plotted in figure 5 on a linear scale (upper) and on a semi-logarithmic scale (bottom). The analytical result is shown by the dashed curve. The distribution from the GPU Monte Carlo simulation for  $\mu = 100$  slightly deviates from the analytical curve, whereas the Monte Carlo simulation for  $\mu = 1000$  gives better agreement.

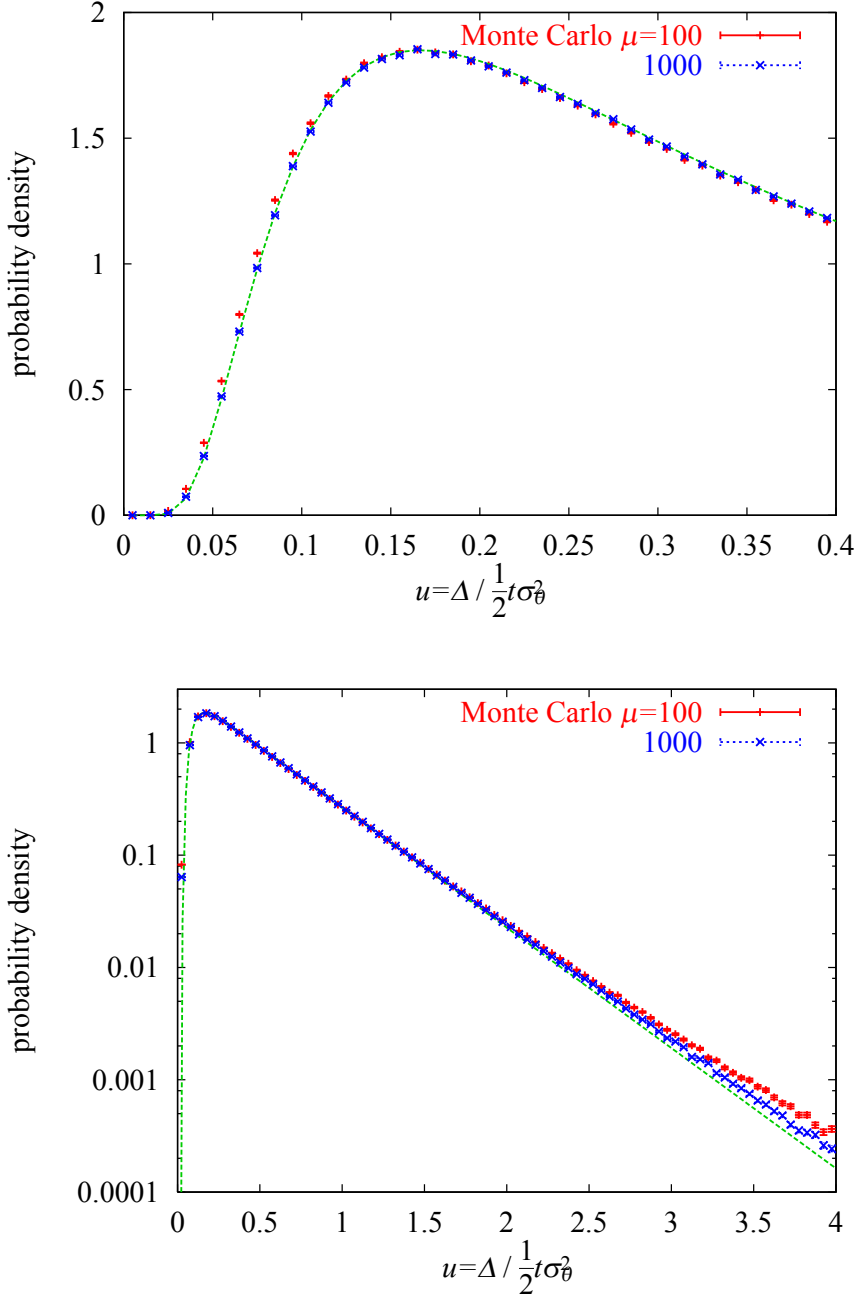


Figure 5: The excess path length distribution for  $\mu = 100, 1000$  and  $\sigma_\theta = 0.1$ .

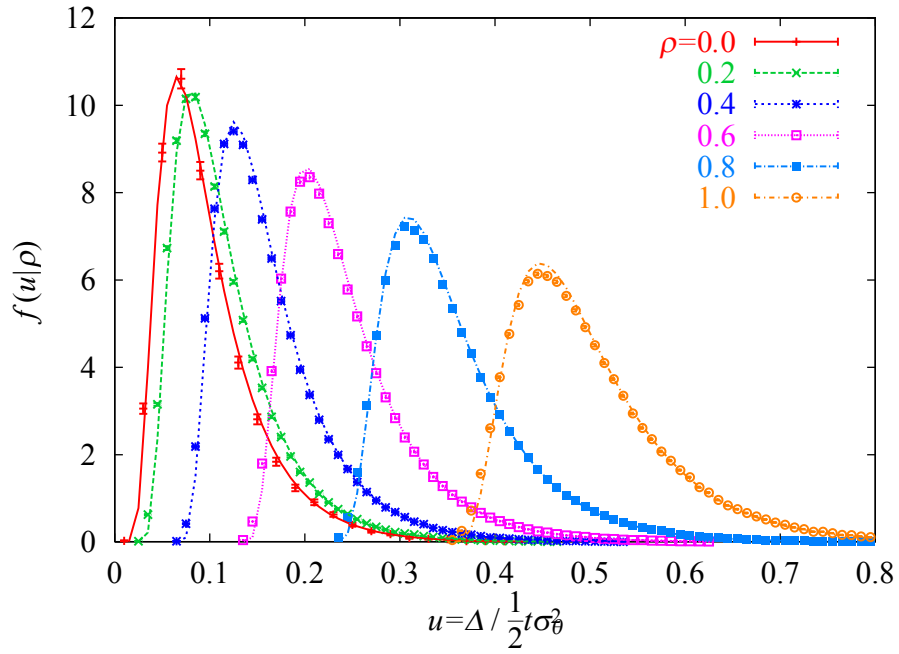


Figure 6: The conditional probability density  $f(u|\rho)$  for  $\mu = 100$  and  $\sigma_\theta = 0.1$ .

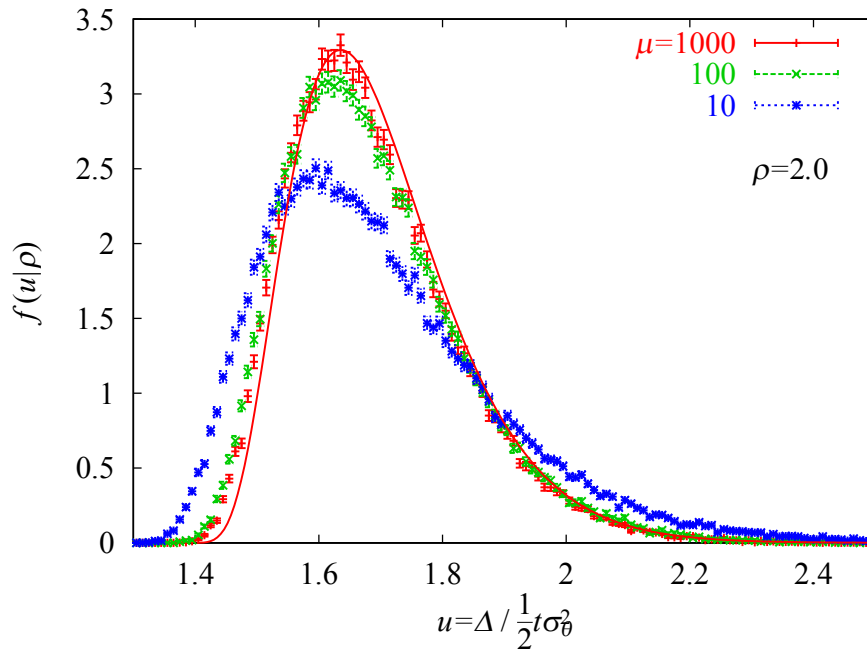


Figure 7: The conditional probability density  $f(u|\rho)$  for  $\mu = 10, 100, 1000$ , and  $\sigma_\theta = 0.1$ .

Figure 6 shows the conditional probability density distribution  $f(u|\rho)$  of the excess path length  $u$  given the lateral displacement  $\rho$  ( $\rho = 0, 0.2, 0.4, 0.6, 0.8, 1$ ) for  $\mu = 100$  and  $\sigma_\theta = 0.1$ . The symbols with error bars show the distributions obtained from the GPU simulations and curves show the analytical results. Also, figure 7 shows  $f(u|\rho = 2)$  for  $\mu = 10, 100, 1000$  and  $\sigma_\theta = 0.1$ .

As  $\rho$  increases, the distributions obtained from the GPU Monte Carlo simulations deviate from the analytical curves, however, the discrepancy decreases as  $\mu$  increases. Hence, it can be said that the discrepancy is not caused by errors in the GPU simulations but rather because the number of deflections is not large enough.

## 4 Conclusion

We have tested the effectiveness of the GPU computing for the charged particle transport. It was found that a GPU (NVIDIA GeForce 8800 GTX) accelerates charged particle transport Monte Carlo simulations by more than an order of magnitude over a CPU (Intel Core2Duo E6700) for the cases where the mean number of Coulomb scattering per event is larger than 100.

In order to validate the GPU Monte Carlo simulations, the excess path length distributions obtained from the simulations were compared with the analytical ones which were calculated using a numerical inverse Laplace transform algorithm. The Monte Carlo and analytical results agree well in the multiple scattering regime.

Therefore we conclude that the GPU Monte Carlo simulation of charged particle transport is not just fast but accurate and GPUs seem promising for the charged particle transport computation, although the performance gain depends on a particular application and/or processor.

## References

- [1] K. Okei and T. Nakatsuka, *Proc. 15th EGS Users' Meeting in Japan*, KEK Proceedings 2008-7, 8 (2008).
- [2] NVIDIA CUDA Compute Unified Device Architecture Programming Guide ver. 2.0 (2008)
- [3] [http://www.nvidia.com/object/cuda\\_home.html](http://www.nvidia.com/object/cuda_home.html)
- [4] C. N. Yang, *Phys. Rev.* **84**, 599 (1951)
- [5] T. Nakatsuka, *Phys. Rev. D* **35**, 210 (1987)
- [6] J. Abate, *ORSA J. on Computing* **7**, 36 (1995)
- [7] P. L'Ecuyer, *Mathematics of Computation* **65**, 203 (1996)